Université catholique de Louvain

Louvain School of Engineering

Institute of Mechanics, Materials
and Civil engineering

Centre for Research in Mechatronics

Multiphysics Modelling of Multibody Systems : Application to Railway Pneumatic Suspensions

Nicolas Docquier

Mechanical engineer

Ph. D. Thesis

Members of the jury:

Prof. Paul Fisette *(Promoter)*	Université catholique de Louvain
Prof. Hervé Jeanmart *(Promoter)*	Université catholique de Louvain
Prof. Jean-Claude Samin	Université catholique de Louvain
Prof. Olivier Brüls	Université de Liège
Prof. Stefano Bruni	Politecnico di Milano
Prof. Grégoire Winckelmans *(President)*	Université catholique de Louvain

Louvain-la-Neuve, Belgium

November 2010

Remerciements

Bien qu'il n'y ait qu'un auteur sur la première page, écrire une thèse relève malgré tout d'un travail d'équipe. Je souhaite donc exprimer ma reconnaissance envers toutes les personnes qui m'ont aidé à la réaliser, directement ou indirectement.

Plus particulièrement, merci à Paul pour m'avoir permis d'entamer des recherches au sein de son équipe "multicorps". Ses nombreux conseils et son optimisme m'ont toujours encouragé à avancer et ce, dans une excellente ambiance amicale, sportive et toujours motivante.

Merci à Hervé d'avoir été un deuxième promoteur à part entière. Son expertise dans le domaine de la mécanique des fluides a permis que le mot "multiphysics" prennent tous son sens dans mes recherches.

Merci à Jean-Claude dont l'expérience et la clairvoyance sont venus compléter à merveille mon "comité d'encadrement". J'apprécie particulièrement ces discussions un peu plus théoriques que nous avons parfois ensemble.

Je remercie aussi les autres membres du jury, M. Grégoire Winckelmans, M. Olivier Brüls et M. Stefano Bruni qui a fait ce long déplacement. Leurs commentaires et remarques ont grandement contribué à améliorer la qualité de ce travail. Grazie mille!

J'aimerais également remercier tous les enseignants que j'ai rencontré à Louvain-la-Neuve, Wavre, Colombes, Paris et ailleurs, et qui exercent un métier pas toujours assez reconnu de nos jours mais ô combien important. J'ai une pensée particulière pour mon professeur de "Sciences Physique" au collège, M. Couderc, qui avec son dynamisme et les nombreux travaux pratiques qu'il proposait m'a définitivement donné le goût pour les matières que j'ai étudiées plus tard.

Je souhaite également souligner la disponibilité et l'efficacité de tous les membres de l'iMMC sans qui la réalisation de certaines expériences n'aurait tout simplement pas été possible. Je pense notamment aux membres du LAFAB (Axel, Jovino, Alban et Jean), du LEFT et du LEMSC et tout particulièrement à Christophe: merci pour les nombreuses heures passées ensemble à secouer le coussin pneumatique! Merci également à Jean-Marie Seynhaeve pour ses conseils et sa disponibilité qui m'ont été très utiles dans la mise au point de certains modèles.

J'ai par ailleurs vraiment apprécié les nombreux contacts établis avec les membres du bureau d'étude "bogie" de Bombardier Transport à Crespin. L'expertise de M. Frederik Allert et de M. Johannes Picht m'a permis de mieux découvrir le milieu ferroviaire. Merci également à M. Antoine Mouchart d'avoir lancé ce sujet voici déjà quelques années.

Merci à Grégory, dont l'aide pendant les essais expérimentaux et son apport via son mémoire de qualité furent particulièrement bénéfiques.

Merci à tous mes collègues et anciens collègues du CEREM qui, en assurant une ambiance de travail exceptionnelle, me donne le sourire quand je monte sur mon vélo tous les matins. Merci à Benoit pour les 4 années passées ensemble au b.-160 à lancer de nouvelles idées, notamment en termes d'aménagement intérieur de bureau... Merci à Olivier de ne pas m'avoir laissé seul après le départ de Benoit mais au contraire de m'avoir fait bénéficier de son expérience récente pour cette phase tant redoutée qu'est la rédaction de thèse! Merci à Antoine, mon troisième compagnon de bureau avec qui encadrer les projets multicorps des étudiants est un réel plaisir.

Many thanks to Michel and Augustin for helping to improve English of this work. I am also grateful to David and John for correcting other papers that are at the basis of some parts of this thesis.

Merci à tous mes amis avec qui je passe de tellement bons moments. Je salue particulièrement ceux que j'ai rencontrés durant mes études et avec qui j'ai pu nouer une réelle relation d'amitié. Et un merci tout particulier à Bertrand pour avoir relevé avec moi le défi des suspensions pneumatiques durant notre mémoire.

Merci à toute ma famille qui m'a toujours soutenu et encouragé. Cette ambiance dans laquelle j'ai grandi et continue de m'épanouir m'est très précieuse.

Merci à celle que j'aime et qui marche avec moi, main dans la main, qu'il pleuve ou que le soleil brille. C'est promis Magali, je vais aussi reprendre du temps pour construire notre petit nid!

Dans nos obscurités, allume le feu qui ne s'éteint jamais, ne s'éteint jamais.

A Grand-Père

Abstract

Nowadays, computers have taken an important place in both private and professional activities. It is especially the case in the field of engineering for which several computer tools and software have been developed in the last decades, often denominated with the term *Computer Aided Engineering* (CAE). The apparition of several acronyms ensues: CAD for Computational Aided Design, CFD for Computational Fluid Dynamics, FEA for Finite Element Analysis, CACE for Computer Aided Control Engineering, etc. Within this framework, Multibody System (MBS) dynamics deals with systems composed of several rigid or flexible bodies characterized by their mass and inertia. Those bodies are connected by joints and interact with each other and with their environment via internal or external forces. Starting in the sixties, multibody dynamics now deals with a large range of applications like satellites, robots, road and rail vehicles and even the human body. Firstly developed in parallel with finite elements techniques, the exchanges between the two disciplines were then largely investigated to address problems involving large motion of flexible bodies. More generally, the tendency is now to couple various tools such as MBS and CACE or MBS and CFD so as to study more complex applications and analyse interactions between phenomena concerning various domains of engineering.

In the field of vehicles, the demand for transportation is still growing, requiring more safety, higher speeds and still improved comfort. Regarding railway transportation, a noticeable evolution has concerned the use of pneumatic suspensions which replace conventional helical springs by air chambers. Even though the first patent about air springs for railway application dates back to the 1840's, their practical use began in the second half of the twentieth century. For instance, pneumatic cushions has been used since the second version of the French TGV ("TGV Atlantique") and significantly improve their comfort. Besides, pneumatic suspensions were used before on metros for which the possibility of controlling the vehicle height and of adapting to variable payload is very beneficial. To achieve those interesting properties, the air suspension involves a complete pneumatic circuit composed of auxiliary tanks, pipes, restriction orifices and several valves, as illustrated in Fig. 1. Those various components can be combined in many ways leading to several suspension morphologies. From an industrial point of view, it appears that the choice between

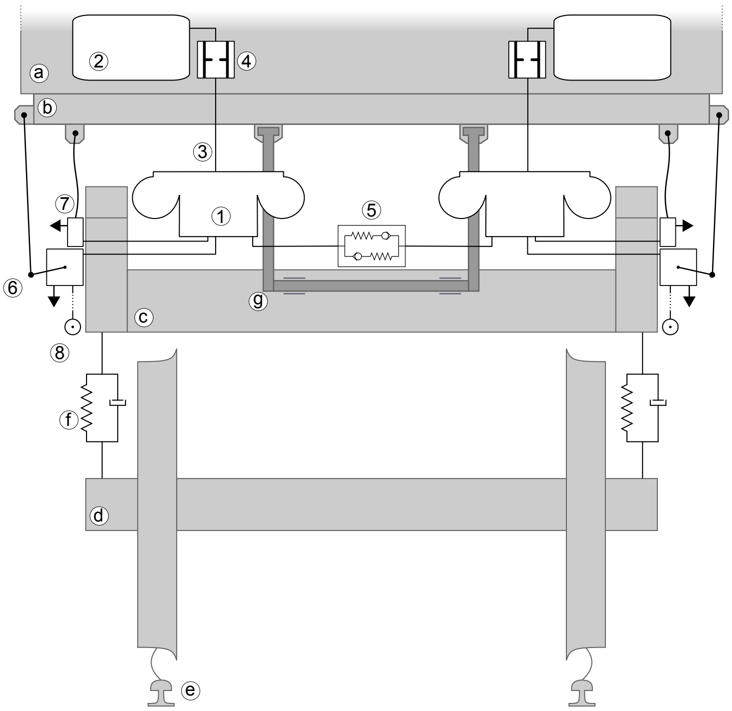

Vehicle main components		Pneumatic components	
a	Carbody	1	Bellows
b	Traverse	2	Auxiliary tank
c	Bogie frame	3	Pipe
d	Wheelset	4	Pipe orifice
e	Track	5	Differential pressure valve
f	Primary suspension	6	Levelling valve
g	Anti-roll bar	7	Safety valve
		8	Pressure source

Figure 1: Illustration of a simplified bogie and the various components of its pneumatic suspension.

those configurations, for a given customer, is achieved out of habit, rather than referring to a systematic design process. Resorting to a simulation tool offers the possibility of tackling this concern with limited costs.

Multibody dynamics is certainly a powerful way to model railway vehicles. Many developments were performed and railway specific features such as the wheel/rail contact problem were implemented in commercial multibody packages. They are now widely used in the industry to design vehicles and analyse their performances, for example, in terms of comfort and safety. However, suitable tools to study the behaviour of the overall pneumatic suspension circuit are still lacking. The present work therefore aims at analysing the existing pneumatic suspension models and proposing a modelling approach that involves most of the pneumatic circuit elements and that can be coupled with multibody dynamics. The goal is both to be able to address industrial problems and to provide an in-depth understanding of the physical phenomena that occur in the system.

To take up the challenge, the present thesis is divided into four parts. In the first chapter the above-mentioned context and the required tools are more deeply introduced. On one hand, various multibody system modelling techniques are reviewed and it is explained how they can be coupled with other disciplines. On the other hand, the various components of a pneumatic suspension are described and several circuit morphology examples are given.
Various modelling approaches for the pneumatic circuit are presented in chapter 2. A comparison test case is described and more details are given about two models already existing in multibody software. Then a component oriented approach based on thermodynamics is developed, focusing on pipes for which several methods are compared. It is shown how the chosen equations affect the frequency response of the suspension.
Chapter 3 is dedicated to the analysis of experiments carried out on a real suspension. A system composed of an air spring connected to an auxiliary tank is submitted to various kinds of excitation and various configurations of the connecting pipe are tested. It is first explained how the parameters of the previously established models can be determined. The influence of heat transfer phenomena receives a particular attention. The dynamic response of the suspension is tested and experimental measurements are confronted to simulation

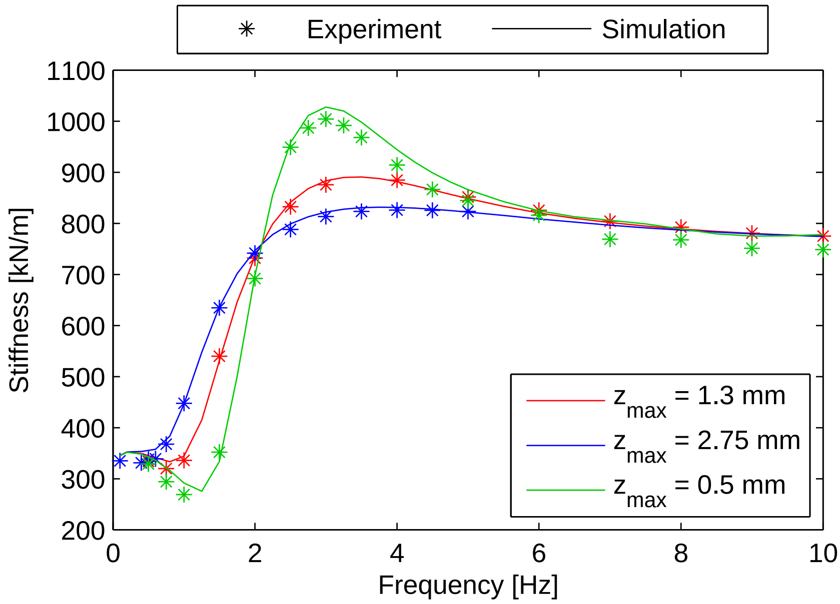

Figure 2: Dynamic stiffness of a suspension submitted to a vertical sinusoidal displacement excitation. Influence of the excitation amplitude.

results as it appears in Fig. 2.

In the last part of this work, a complete metro car and its pneumatic circuit are implemented. The complete vehicle performances are thus analysed for tests in which components such as valves play an important role. In particular the impact of some suspension component failure is investigated. Finally, thanks to the developed approach, novel suspension morphologies inspired from automotive suspensions are explored and compared to various well-established topologies (Fig. 3).

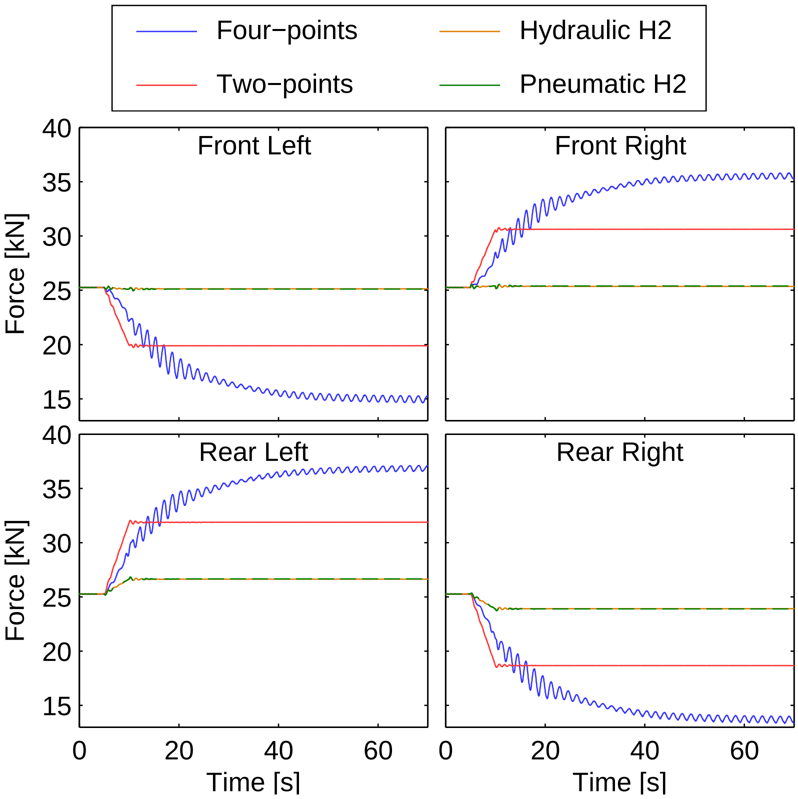

Figure 3: Vertical component of the wheel/rail contact force for a metro car submitted to a twisted track excitation. Comparison of various pneumatic suspension morphologies.

Contents

Chapter 1

Introduction

Multibody systems and railway dynamics: a difficult marriage?

Multibody system (MBS) dynamics studies the motion of mechanical systems composed of several rigid or flexible bodies interconnected by joints and submitted to internal or external forces and torques. Those forces can result from both passive elements such as springs, or active components such as electromechanical actuators. The first applications of multibody systems date back to the mid-sixties and were related to satellite stability.

The use of MBS to study vehicles only began in the eighties. The quite long time before the integration of MBS tools in the vehicle dynamics analysis, especially railway vehicles, is due to several factors. First, the relative motions between the various parts of a railway vehicle are very small: of the order of the centimetre for suspended elements and some millimetres for non-suspended elements. This makes it possible to generate and linearise the equations of motion without resorting to a specific formalism. Additionally, the connecting elements such as springs and dampers can suitably be represented by linear laws, especially in the case of small displacements. Furthermore the railway vehicle topologies were not so numerous, often a carbody carried by two rigid bogies, and thus this did not require to re-build the set of equations for each vehicle. This is especially true since the vertical and lateral dynamics are well decoupled making it possible to use a specific model for each direction. The use of the multibody approach was therefore unnecessary. It could even be more disadvantageous to use non-linear MBS formalism intrinsically dedicated to large body motion to study railway systems that would require a re-linearisation of the equations. However, the improvement of multibody techniques reversed the tendency. In 1991, the International Association for Vehicle System Dynamics (IAVSD) defined four benchmarks on which several multibody codes were confronted. Besides, some special architectures were designed such as the BA2000 articulated bogie (Ref. [28]) or independent wheel bogies for which the multibody formalism is especially suitable (see for instance Refs. [17, 27]). Furthermore, dedicated models for railway specific features such as the wheel/rail contact problem were introduced in MBS (Ref. [29]) and were implemented in multibody packages such as SIMPACK (Ref. [65]). Thanks to such tools, it is now possible to study in detail the behaviour of specific parts such as the influence of an anti-roll bar or the interaction between the catenary and the pantograph. Moreover, much software has been developed and is now able to address industrial demands. Indeed, multibody dynamics is nowadays a suitable mean to deal with mechatronics defined as the *"synergistic combination of mechanical engineering, electronics, control systems, and computers"* by Craig and Stolfi for which *"the key element in mechatronics is the integration of these areas through the design process"* (Ref. [20]). This requires the development of efficient multidisciplinary simulation environments in which, according to Kortüm and Vaculín, multibody tools can play a central part (Ref. [42]). The present thesis falls within this framework aiming at proposing and implementing suitable models to deal with modern railway pneumatic suspensions.

This chapter introduces and defines the concepts employed and developed in our study. We first introduce multibody dynamics in more details presenting the main formalisms and some application domains. We then review some well-established techniques to deal with multi-domain analysis. Finally, we describe the railway vehicle structure focusing on the pneumatic suspension system.

1.1 Multibody Dynamics

1.1.1 Multibody formalism

The first step in many multibody problems, as in many other mechanical fields, consists in describing the system topology in a suitable way for mathematical analysis. The main components of a multibody system are:

- the bodies, characterized by their mass, centre of mass location and inertia tensor;
- the joints that determine the relative motion between two bodies or between a body and the inertial frame.

In order to establish the kinematics and dynamics of a multibody system, body configurations[1] have to be determined according to various approaches:

- the relative coordinate approach,
- the absolute coordinate approach,
- the natural coordinate approach,
- the nodal absolute coordinate approach.

Using *absolute coordinate*, the configuration of each body is defined with respect to the inertial frame which is supposed to be fixed (see Fig. 1.1(a)). So, for a three-dimensional problem, the body configuration will be described by at least six variables, whatever the connections with other bodies. The joints are taken into account a posteriori by adding constraints to the system.
For *relative coordinates*, the configuration of a body is defined relatively to another one called the parent body. The parent body configuration is also defined with respect to its own parent, etc., until reaching the inertial frame (see Fig. 1.1(b)). For most applications, this approach dramatically reduces the number of coordinates and joint constraints are automatically taken into account. However, it can lead to highly non-linear equations. The relative coordinate approach also implies that the system has a tree-like structure: a body has one and only one parent body. Many mechanical systems do not respect this condition and present so-called *kinematic loops* (Fig. 1.2(a)). Nevertheless, if it appears, loops can be cut to restore a tree-like structure and be replaced by equivalent algebraic constraints, as illustrated in Fig. 1.2(b). Let us note that algebraic constraints do not arise from kinematic loops only. For instance, they can be due to the structure of a joint such as a screw which implies combined translation and rotation along the same axis.

An alternative to absolute and relative coordinates are the *natural coordinates* introduced by García de Jalón in the early eighties (see Refs. [32, 33]

[1] The configuration of a body denotes its position and orientation.

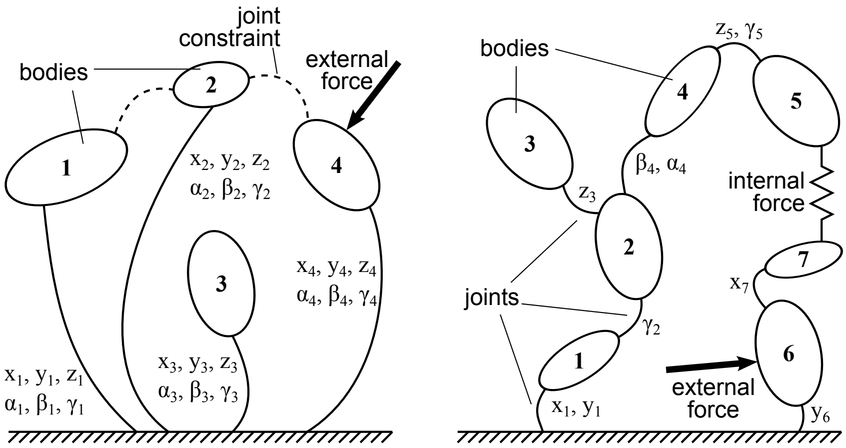

(a) (b)

Figure 1.1: (a) Absolute coordinates: each body configuration is defined by three translation coordinates and three orientation coordinates (b) Relative coordinates: the configuration of each body is defined with respect to the parent body. x, y and z coordinates refer to translation coordinates along each axis while α, β and γ refer to orientation coordinates.

for more details). The main asset of this approach is that no angular coordinates are introduced since the configuration of each body is defined by the position of *basic points* and the Cartesian components of *unit vectors*. There are several possible combinations of basic points and unit vectors to define the configuration of a same body. Generally speaking, at least three basic points are needed so as to describe the configuration of one body. Nevertheless, because the dynamical properties of a body (mass, center of mass and inertia) are only determined by the mass associated to each basic point, using additional points can be more convenient (see Ref. [49] for more details). Furthermore, by judiciously locating the basic points and unit vectors, the total number of coordinates remains limited. For instance, a spherical joint is implemented by using one basic point that is shared by the two bodies connected by the joint (Fig. 1.3(a)). Algebraic constraints may arise from two sources. On one hand, the body rigidity is ensured by imposing constraints such as a constant length between the basic points. On the other hand, most of the joints imply

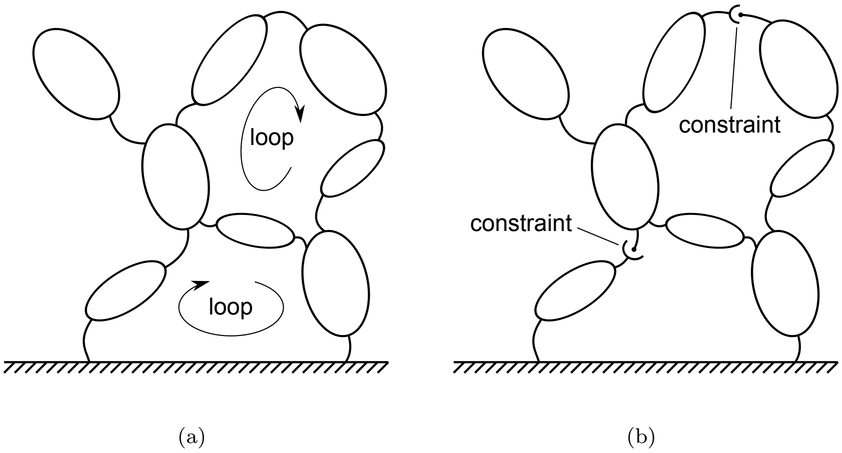

Figure 1.2: Relative coordinate illustration of loop constraints. (a) Multibody system with kinematic loops. (b) Equivalent tree-like structure where kinematic loops are cut and constraints are added.

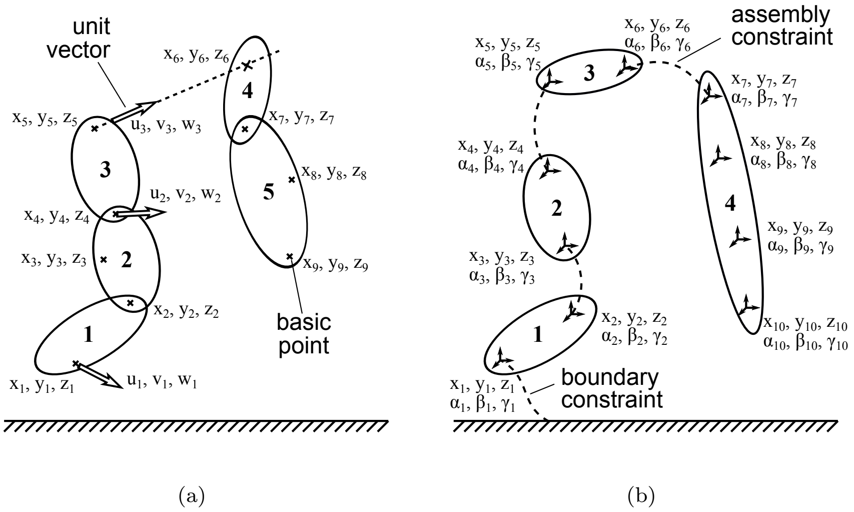

Figure 1.3: (a) Natural coordinates: each body configuration is defined by the position of basic points and the Cartesian components of unit vectors. (b) Finite-element coordinates: the position of each body is defined by nodal points which have their own set coordinates.

constraints that restrict the motion of the basic points and unit vectors. For instance, a cylindrical joint can be implemented by imposing that the two connected bodies share a unit vector in the direction of the joint axis and that one basic point on each body remains aligned with the unit vector.
Beside those three techniques which originate from rigid multibody systems, the nodal absolute coordinates, used with the *multibody finite element technique*, aim at integrating flexible bodies from the very first steps of the formalism development instead of adding flexible deformation to large body motion as it is classically done. In the method proposed by Géradin and Cardona (Ref. [34]), each body has its set of nodes and each node is defined by a subset of coordinates (Fig. 1.3(b)). The total motion of each node (rigid motion and flexible deformation) refers directly to the global inertial frame like the absolute coordinate approach. Algebraic constraints arise from four origins: boundary nodal constraints emanate from connections between a body and the ground, assembly nodal constraints represent the joints, driving constraints impose the motion of certain nodes and zero strain constraints are used for representing rigid bodies.

MBS are submitted to internal and external forces or torques (or *efforts*). External efforts act on a body of the system and react on its environment. Gravity, ground/tyre contact forces for vehicles, aerodynamical drag are typical cases of external forces. In case of internal forces, the force acts on a body and reacts on another body of the MBS. A good example is the force due to a car suspension spring/damper acting for instance between the chassis and the suspension arm.

Several formalisms have been developed so as to automatically obtain the equations of motion of any multibody system. The most basic one relies directly on the Newton-Euler equations. The so-called recursive Newton-Euler algorithm (Ref. [60]) allows to reduce the computational efforts when relative coordinates are used. The equations can also be obtained by using the virtual power (or work) principle or by using Lagrange's equations, which consider the system at the energy level.

Whatever the formalism, the equation of motion of a multibody system are generally presented in the following form:

$$\begin{aligned} \mathbf{M}(\mathbf{q})\ddot{\mathbf{q}} + \mathbf{c}(\mathbf{q}, \dot{\mathbf{q}}, \mathbf{g}) = \mathbf{Q}(\mathbf{q}, \dot{\mathbf{q}}, t) + \mathbf{J}^T \boldsymbol{\lambda} \\ \mathbf{h}(\mathbf{q}) = 0 \end{aligned} \tag{1.1}$$

with: $\mathbf{M}$ the generalized mass matrix,
$\mathbf{q}$ the generalized coordinate vector,
$\dot{\mathbf{q}}$ its time derivative,
$\ddot{\mathbf{q}}$ its second order time derivative,
$\mathbf{c}$ the non-linear dynamic vector (gravity, Coriolis and centripetal effect)
$\mathbf{Q}$ the generalized force vector,
$\mathbf{h}$ the algebraic constraint vector.
$\mathbf{J} = \frac{\partial \mathbf{h}}{\partial \mathbf{q}^T}$ the constraint Jacobian matrix,
$\boldsymbol{\lambda}$ the Lagrange multiplier vector.

Therefore, multibody dynamics generally implies a set of differential algebraic equations (DAEs), which requires special care to be time integrated. Several techniques have been proposed to deal with the time integration of multibody DAE system.

- Constraint stabilization (Ref. [10]) consists in derivating the constraint equations so as to transform the DAEs into ordinary differential equations (ODEs). Constraints are thus not exactly solved and can deviate from the exact solution. Stabilization terms are added to solve the problem but the setting of the related coefficients is not straightforward.

- The generalized coordinate partitioning techniques (Ref. [69]) consist in splitting, on the basis of the constraints, the set of generalized coordinates into two groups: *dependent* and *independent variables.* The equations of motion are split accordingly:

$$\begin{aligned} \begin{pmatrix} \mathbf{M}_{uu} & \mathbf{M}_{uv} \\ \mathbf{M}_{vu} & \mathbf{M}_{vv} \end{pmatrix} \begin{pmatrix} \ddot{\mathbf{u}} \\ \ddot{\mathbf{v}} \end{pmatrix} + \begin{pmatrix} \mathbf{c}_u \\ \mathbf{c}_v \end{pmatrix} = \begin{pmatrix} \mathbf{Q}_u \\ \mathbf{Q}_v \end{pmatrix} + \begin{pmatrix} \mathbf{J}_u^T \\ \mathbf{J}_v^T \end{pmatrix} \boldsymbol{\lambda} \\ \mathbf{h}(\mathbf{q}) = 0 \end{aligned} \tag{1.2}$$

  The dependent variables $\mathbf{v}$ are calculated as functions of the independent variables $\mathbf{u}$ by solving exactly the algebraic constraints at position, velocity and acceleration levels. The Lagrange multipliers $\boldsymbol{\lambda}$ and dependent variables are eliminated from the independent variable equation subset so as to calculate the independent accelerations. Therefore, only the independent variables have to be considered by the integrator which can be a classical ODEs solver.

- The direct methods attempt to attack *directly* the complete set of DAEs by applying, for instance, a backward differentiation formula to variables and by solving the resulting system at each step using a Newton/Raphson type method (e.g. Ref. [30]). They are quite efficient from the computational time viewpoint and are particularly suitable for stiff equations like those arising from flexible body problems.

Regarding the equations generation problem, two ways can be envisaged:

- the *numerical* generation: the equation system is rebuilt at each time step of integration depending on the current values of coordinates and forces.

- the *symbolic* generation: the equation system is built only once in a symbolic form, as it could have been done analytically by hand. This approach becomes efficient thanks to the symbolic simplification which avoids recalculation of useless terms. It is particularly efficient for the relative coordinate formulation (see for instance Ref. [60]).

Eventually, let us mention that two main model formulations are often treated in multibody dynamics:

- the *direct dynamics:* for given initial conditions and external and internal forces, the position and velocity of each body are calculated via time integration of the accelerations. It is often used for instance in vehicle dynamics.

- the *inverse dynamics*: for an imposed system trajectory, i.e. positions, velocities and accelerations imposed as function of time, the corresponding (joint) forces must be calculated. It is a typical approach used in robotics or biomechanics for example.

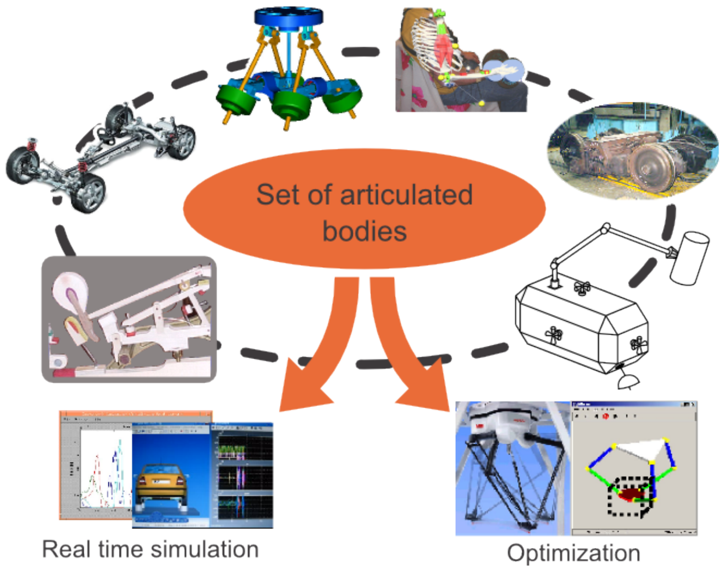

Figure 1.4: Illustration of multibody systems applications.

1.1.2 Application domains

As illustrated in Fig. 1.4, multibody dynamics covers a wide range of applications, from robotics to vehicles to human body. This section briefly presents typical physical and virtual domains covered by multibody system.

Physical domain In the sixties, the first applications concerned *aerospace systems*. At that time, the computers only allowed us to use multibody formalism to design the passive stability of satellites and spacecraft as well as to study their active control (Refs. [37, 59]). The numerical analysis was validated on Earth and then applied to problems without gravity for which experiments on Earth are quite complex.
Later on, multibody dynamics was used to analyse the kinematics and dynamics of *complex mechanisms* such as pantographs.
In the eighties, multibody formalism began to be used in *robotics*, for instance for computer-torque based control or for the dynamic parameter identification

of serial robots (Ref. [58]). In this domain, the inverse dynamics is widely used to calculate the actuator efforts required to follow a given trajectory. Nowadays, multibody dynamics is very helpful in analysing *parallel robots* that are often very light and imply high dynamics and for which flexibility may not be negligible.
As already mentioned, multibody dynamics is also especially suitable to deal with *road* and *rail vehicles*. For example, for a simple car model, the chassis can constitute the main body on which suspension arms are mounted via revolute joints. The wheel rotates with respect to the wheel carrier which is articulated on the suspension arms. Ground tyre interaction is modelled by external forces acting on the wheels. In case of rail vehicles, the wheel/rail contact problem is a really challenging question for which an important research activity was and is still conducted. Issues such as vehicle stability, passenger comfort and safety, etc., can be addressed using multibody techniques.
The *human body* as well can be considered as a multibody system. Recently, many research activities have been conducted in this field. Multibody dynamics formalisms are used for example to quantify the human joint force and muscle efforts during a given activity (Refs. [56, 57]). Such information is very useful for surgeons to prepare a surgical operation or for therapists to support the rehabilitation. Multibody dynamics can also be used to analyse sportsman performances or to improve system ergonomics such as automobile ingress movements of passengers (Ref. [46]).

Virtual domain Formalisms and specific techniques has been developed so as to perform *real-time* simulations (Ref. [52]). Providing time efficient calculation is especially interesting in order to address modern industry concerns such as active suspension control.
MBS are furthermore used in *control design*, such as the control of *overactuated* robots (Ref. [31]) or *flexible mechanisms* (Ref. [15]).
The time efficiency of multibody formalisms allows to combine them with *optimization* tools, which have many specific prospects such as the *mechanisms synthesis* (Ref. [19, 18]). Related to this point, the *sensitivity analysis* of multibody dynamics becomes more and more important. For instance, it can be used for a car suspension in order to establish how important a parameter is regarding the comfort or the stability. At present, many research efforts are made in

order to compute symbolically the sensitivity of a multibody system (Ref. [51]).

1.1.3 Computer implementation and tools

The various techniques and formalisms described in section 1.1.1 have led to the implementation of various computer tools and software. Presenting all the existing software is almost impossible since each research team working in multibody dynamics has developed its own tool, often dedicated to a specific application field.
Regarding commercial or industrial software, the most used are ADAMS produced by MSC Software, SIMPACK developed at first by the German aerospace agency DLR and LMS Virtual Lab Motion. The SAMCEF MECANO package which arises from research conducted at the Université de Liège (Belgium) is based on finite element methods which make it a suitable tool to deal with flexible multibody systems. However, it does not deal with railway specificities. On the contrary, VAMPIRE is an industrial software purely dedicated to the modelling of railway vehicles.
In this thesis, we will use the SIMPACK software which is one of the most used by the railway industry. SIMPACK relies on relative coordinates and on a numerical generation of the equation of motion. It provides a joint library that contains conventional elements such as simple revolute joints, prismatic joints, universal joints, etc., and specific features to deal with railway vehicles. Concerning time integration, SIMPACK provides classical ODEs integrators for unconstrained system and especially developped DAEs solvers for systems implying algebraic constraints.
Next to those industrial packages, many scientific computer programs have been and are still developed. Those tools are often used to develop and test new features. They are often more flexible to answer more specific requests that come out of the scope of classical industrial applications. At the Université catholique de Louvain (Belgium), the ROBOTRAN program was written at the beginning of the nineties (Ref. [27]). It is a symbolic generator which is able to compute the equation of mechanical systems in a symbolic form and following various formalism. The user has then the possibility of focusing on the modelling of force elements and developing in an “open manner”, which makes it a very flexible tool for a wide range of applications.

1.2 Multiphysics modelling of multibody systems

For several years now, engineers have relied more and more on computer tools to design new systems and analyse existing devices. In each field of engineering, the development of new formalisms and software coupled to the improvement of computer efficiency makes the analysis of even more realistic applications possible. In this context, it is often needed to combine modelling approaches from different domains to investigate the interaction between several parts of a device. For instance, modelling of mechatronics systems often implies the coupling of multibody dynamics with other disciplines such as electricity, hydraulics, pneumatics, control, etc.

As depicted by Arnold and Heckmann in Ref. [9] and Samin et al. in Ref. [61], many techniques have been developed in order to combine multibody dynamics with other fields of engineering. Two main strategies can be distinguished.

- The *strongly coupled* approaches consist in assembling the contributions of the various disciplines into one set of coupled equations that is provided to a single monolithic integrator. The coupling is thus performed at the modelling or equational level by the mean of unifying theory or by extending multibody formalisms.
- The *weakly coupled* techniques implement the coupling, a posteriori, at the simulation level by using special integration techniques such as the co-simulation. The equations of the different domains are generated and then integrated by independent solvers that exchange informations at fixed time step, possibly with iteration process to increase the numerical accuracy and stability.

The weakly coupled techniques present a good modularity and a relatively straightforward implementation by means of the interfaces available in the implied software. Furthermore, it can take advantage of specific integrators dedicated to each discipline.

For the strong coupling technique, which is more reliable when the frequency ranges of the coupled domains are similar (Ref. [62]), the generation of a unique equation set independent of any solvers makes it a very portable solution that is particularly useful to deal with time simulation but also modal analysis, optimization, sensitivity analysis, etc.

In this section, we will briefly review some coupling techniques. We will then present some specific coupling cases and discuss the pneumatic-multibody coupling at the root of our railway application.

1.2.1 Strongly coupled approach

Linear graph method

This techniques consist in representing the system as a graph that identifies each components which can be of two types: *storage* for a component able to store energy and *dissipative* for a component that dissipates energy (see Ref. [62] for further details). The constitutive equations of each component can be formulated in terms of so-called *through* variables, i.e. variables that may be measured by an instrument mounted in series with the component (e.g. the current in an electrical circuit, see Table 1.1), and *across* variables that can be measured by an instrument mounted in parallel (e.g. the pressure in an hydraulic circuit). These variables are commonly called *power* variables and their product represent the energy provided or dissipated by the component. Physical connections between the various components are represented by the nodes for which constitutive equations are also written. Fig. 1.5 illustrates the linear graph of a simple loud-speaker. The equations can be automatically deduced from the graph following a set of systematic derivation rules.

Linear graphs are thus intrinsically well-suited for multidomain problems thanks to the use of *transformer* elements that imply multiphysics constitutive equations in terms of *power* variables. The appearance of the graph is furthermore similar to the system which is userfriendly when working with large systems. However, some specific mechanical constraints, such as the non-slipping constraints or the wheel/rail contact constraint, must be added a posteriori. Moreover, the equations are generated in a less efficient form compared to recursive multibody formalisms, especially when dealing with large and complex structures.

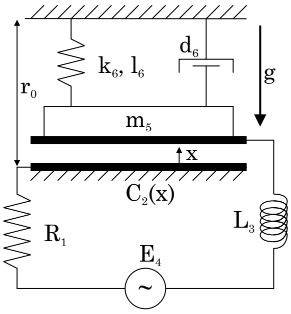

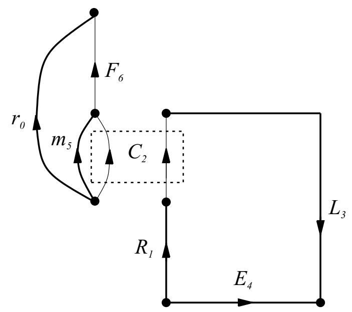

Figure 1.5: (a) Loudspeaker diagram. (b) Loudspeaker linear graph. Illustrations from [62].

	Power variables		Storage Elements		Dissipation
	Across Variable	Through Variable	A-type	T-type	Elements
Mechanics	Velocity	Force	Mass (inertia)	Spring	Damper
Electricity	Voltage drop	Current	Capacitor	Inductor	Resistor
Hydraulics	Pressure	Flow Rate	Capacitance	Inertance	Resistance
Thermics	Temperature	Heat Flow	Capacitance		Resistance

Table 1.1: Linear graph analogies (from [62]).

Bond graph method

In contrast to linear graphs, bond graphs are based on energy exchanges between the components and the environment (see Refs. [41, 50] for further details). Those exchanges are done via *interactive ports* that involve two scalar variables: a *flow*-type and an *effort*-type (see Table 1.2). The product of those two variables represents the transmitted power. A bond graph is obtained by the interconnection of *junctions* and *elements* by means of *bonds*, according to the system topology. The graph appearance is however rather different from the analysed system (see the bond graph of the simple loud-speaker in Fig. 1.6). Bond graphs have the advantage to provide a straightforward interpretation of energy transfer in the system. Nevertheless, their extension to large three-dimensional multibody systems requires the development of *vectorial bonds* that make the modelling quite complex and this represents the main limitation

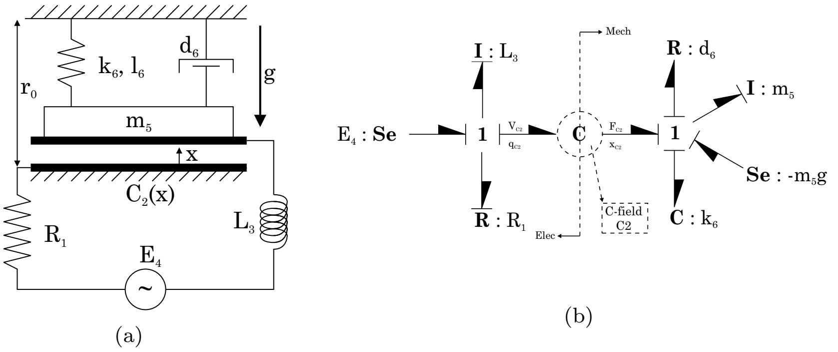

Figure 1.6: (a) Loudspeaker diagram. (b) Loudspeaker bond graph. Illustrations from [62].

	Power variables		Storage Elements		Dissipation
	Effort Variable	Flow Variable	Capacitor	Inertia	Elements
Mechanics	Force	Velocity	Spring	Mass (inertia)	Damper
Electricity	Voltage drop	Current	Capacitor	Inductor	Resistor
Hydraulics	Pressure	Flow Rate	Capacitance	Inertance	Resistance
Thermics	Temperature	Heat Flow	Capacitance		Resistance

Table 1.2: Linear graph analogies (from [62]).

of this technique for multibody applications.

Extension of multibody formalisms

Despite their intrinsic ability to deal with multiphysics problems, unifying approaches such as bond graphs and linear graphs are not necessarily the best choice to treat complex “non-academic” problems such as a the optimization of a complete car equipped with hydraulic suspensions (Ref. [61]). Furthermore, some virtual engineering applications involve not only time domain analysis but also control design, optimization or sensitivity analysis. This requires to formulate equations in a way that is both portable and efficient from a computer viewpoint. Considering the extension of multibody formalisms can thus become more beneficial.

Non-mechanical components can often be taken into account by additional first-order state equation. Eq. (1.1) is thus completed as follow:

$$\begin{aligned}\mathbf{M}(\mathbf{q})\ddot{\mathbf{q}}+\mathbf{c}(\mathbf{q},\dot{\mathbf{q}},\mathbf{g})&=\mathbf{Q}(\mathbf{q},\dot{\mathbf{q}},\mathbf{x},\dot{\mathbf{x}},t)+\mathbf{J}^T\boldsymbol{\lambda}\\ \dot{\mathbf{x}}&=\mathbf{f}(\mathbf{q},\dot{\mathbf{q}},\mathbf{x},\boldsymbol{\lambda},t)\\ \mathbf{h}(\mathbf{q},\mathbf{x})&=0\end{aligned} \tag{1.3}$$

This technique can be implemented in many ways. For smaller problems, the non-mechanical element is often implemented as a force-element in the multibody package. Many software also propose to the user to write its own "user-element". Nevertheless, for larger applications, this methodology can become time-consuming and increases the risk of errors.
In Ref. [61], Samin et al. compare two techniques to extend multibody formalism to electromechanical systems. The first one developed by Sass in Ref. [62] relies on the symbolic generation of both the mechanical and electrical equations. The symbolic generation allows drastic simplification and therefore provide a very compact, portable and time-efficient set of equations. The second technique consists of a numerical modelling based on a finite element formulation applied to all the domains. With this second approach, mechanisms flexibility can also be taken into account thanks to the finite element formulation (see Ref. [15]).

1.2.2 Co-simulation

Co-simulation involves a coupling at the simulation level. Specific integrators solve separately the equation set of each discipline and interact at fixed time-steps. Therefore, each domain model is computed separately. Once done, the input and the output of each part of the system are used by the solvers to exchange information. The communication between subsystems is thus limited by the chosen interaction time-step. According to Arnold et Heckmann (Ref. [9]), a typical time-step size is around 1 ms for vehicle application but it may depend on the coupled domains as we will show later on.

1.2.3 Some specific field coupling

Electro-MBS

Many mechatronic systems imply both electrical circuits and multibody mechanisms. The unified modelling of electromechanical multibody systems has been studied in details by Sass (Refs. [62, 63]) who compared several existing unified modelling theories: bond graphs, linear graphs and virtual work principle. Based on the Robotran symbolic engine for multibody system, it is also proposed to generate symbolic models for the electrical parts and to couple the electromechanical equations into one global symbolic model. Special care needs to be taken to deal efficiently with constrained electromechanical systems on the basis of the coordinate partitioning technique (see section 1.1.1). This method provides a reduced set of equations that can be provided to only one ODE integrator. This technique was used to analyse industrial problems, e.g. to check that replacing DC-motors by three phase inductive motors on a railway bogie would not lead to fatigue issues due to torque oscillations at motor start.

Hydro-MBS

Hydraulics can suitably be modelled using linear graph or bond graph techniques, which can be useful for coupling with other domains. However, those approaches are sometimes limited regarding applications that imply large multibody systems.
Ref. [22] investigates the coupling of hydraulics and multibody dynamics in case of a semi-active hydraulic suspension that implies a relatively complex hydraulic circuit. The problem of connecting several pipes is addressed by considering flow constraints instead of virtual volume. It is also highlighted that a strong coupling approach is far more efficient than co-simulation because of the stiffness of hydraulic equations due to the very small compressibility of oil. This approach has shown a real interest to provide real-time simulations which are very accurate in the $0 - 20\ Hz$ frequency range, while other modelling techniques, for instance using the Adams software, are too slow.

MBS-pneumatics

Mechatronic applications often involve the coupling of multibody dynamics with electrical circuits, hydraulics or thermal effects. Nevertheless, the coupling of mechanical systems and pneumatic circuits is far less described in the literature.
The dynamics of aeraulic components such as ducts, valves, chambers, etc., has of course been studied widely, particularly in the field of combustion engines

or pneumatic drives (see for instance Ref. [11]).
Multiphysics software programs such as AMESIM or ITISIM often propose a pneumatic library with standard components used in industrial applications like cylinders but the modelling of components like pipes can be quite elementary. Other possibilities are available with MODELICA which is *a unified object-oriented language for physical systems modelling.* For instance the commercial PNEULIB library proposes a large number of pneumatic components. Furthermore, MODELICA proposes since 2009 a more advanced library for the study of one-dimensional flows. However, in most cases, such packages lack the possibility to deal with large and complex three-dimensional mechanical systems and therefore resort to co-simulation with multibody software.
Concerning more specifically pneumatic suspensions, as it will be explained later, most approaches consist in extending multibody tools by force-elements that are generally limited to very simple pneumatic assemblies.
In this work, we will therefore investigate how the pneumatic circuit modelling should be refined for a specific domain that involves multibody systems, i.e. railway dynamics. Even though the co-simulation will be used, the developed tools will be implemented independently of the coupling technique so that it would also be possible to resort to strong coupling such as done in Refs. [62] and [22].

1.3 Railway vehicle modelling

1.3.1 Railway vehicle description

Railway vehicles have been used for several centuries and still rely on the same basic principle: the wheel/rail guidance based on the wheel profile conicity.

Railway trains are often composed of several *freight* or *passenger* cars, whose main structure is illustrated in Fig. 1.7. The *carbody* constitutes the larger part of the vehicle, where the goods are placed or the passengers can take place. On some freight trains, the carbody is carried by only two *wheelsets*, each composed of an axle and two wheels. However, for most cases, each carbody is mounted on two *bogies* (see Fig. 1.7). Various bogie structures exist but in most cases they are composed of the following elements:

- the *frame*, which constitutes the heaviest element of the bogie, especially if a motor and other fixed component are taken into account;

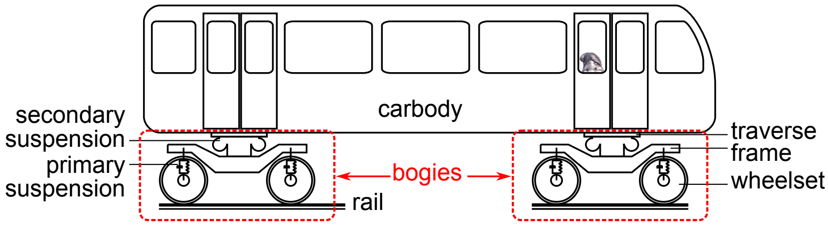

Figure 1.7: Illustration of main components of a railway car.

- the *wheelsets* that ensure the guidance and are connected to the bogie frame via the *axle boxes* which contain the bearings;
- the *traverse* which is connected to the carbody.

Other components such as anti-roll bars, traction rods, etc. are often added on the bogie.
With regard to the suspension, classical bogies contain two stages:

- the *primary suspension* which is located between the axle boxes and the bogie frame and that strongly influence the vehicle stability and guidance properties (Ref. [39]);
- the *secondary suspension* which is placed between the bogie frame and the traverse and ensures the passenger comfort.

1.3.2 Railway pneumatic suspension

For several decades, the secondary suspension of passenger trains has been ensured by air cushions which present the following advantages with respect to classical helical spring systems:

- reduced weight and size for equivalent stiffnesses,
- improved passenger comfort and noise insulation,
- ability to provide both vertical and transverse stiffness,
- possibility of keeping a constant carbody height whatever the payload by adding or removing air in the cushion,

- increasing suspension stiffness with increasing payload due to the air pressure rise which makes the eigenfrequencies remaining almost constant,
- possibility to increase damping by adding restriction orifices in the pneumatic circuit.

However, this kind of suspension implies a more costly and complex design in order to ensure the above-mentioned functions. Indeed, the air spring is connected to a complete pneumatic circuit illustrated in Fig. 1.8.

Pneumatic bellows

The pneumatic *cushions* or pneumatic *bellows*[2] are the main components of the suspension. They are mainly composed of a steel structure and a reinforced rubber diaphragm that allows vertical and horizontal deformations. They are commonly inflated to a pressure varying between 3 and 7 *bar* (relative pressure), depending on the payload. The volume varies between 10 and 40 dm^3. The mechanical device often includes an emergency spring in case of diaphragm puncture as illustrated in Fig. 1.9.

Auxiliary tanks, pipes and orifices

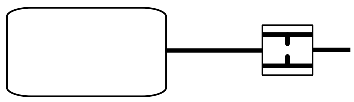

The main function of an auxiliary tank is to increase the total air volume so as to soften the suspension. Its volume is often between 20 dm^3 and 100 dm^3. It is connected to the air cushion via a pipe whose length can vary from some millimetres to several metres when the tank is placed on the roof of the train. A restriction orifice is often added on the pipe to increase the pressure drop coefficient and thus provide more suspension damping. As it will be shown later, the geometrical properties of the tanks and the pipes, especially the pipe length, strongly influence the frequency response of the suspension. Furthermore, in some cases, it has been attempted to implement a semi-active suspension by using a variable area orifice which allows to continuously adapt the suspension properties (see Ref. [6, 36, 66]).

[2] In the present work, the air springs will be denoted by the terms *air springs*, *air bags*, *(air) bellows* or *(air) cushions* without distinction.

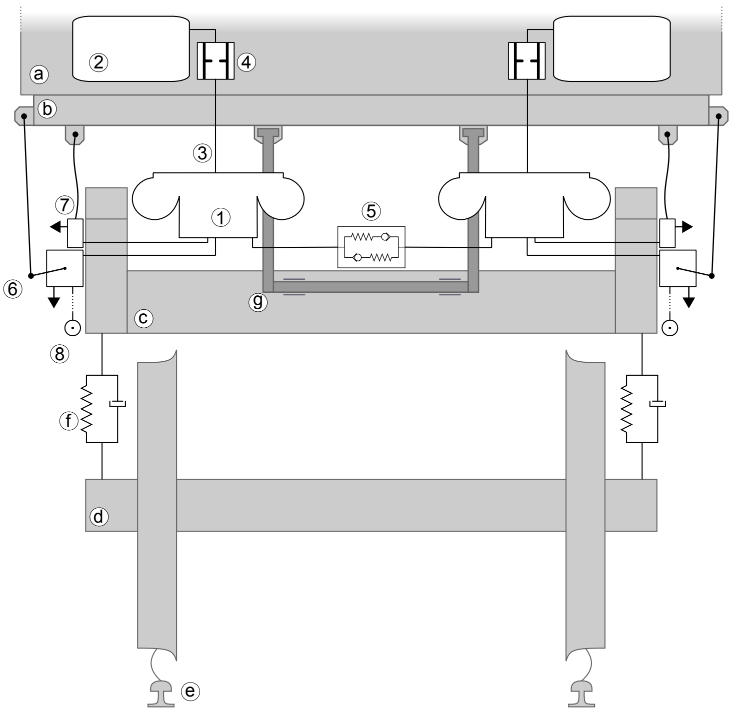

Main components		Pneumatic components	
a	Carbody	1	Bellows
b	Traverse	2	Auxiliary tank
c	Bogie frame	3	Pipe
d	Wheelset	4	Pipe orifice
e	Track	5	Differential pressure valve
f	Primary suspension	6	Levelling valve
g	Anti-roll bar	7	Safety valve
		8	Pressure source

Figure 1.8: Illustration of a simplified bogie and the various components of its pneumatic secondary suspension (view along the longitudinal axis).

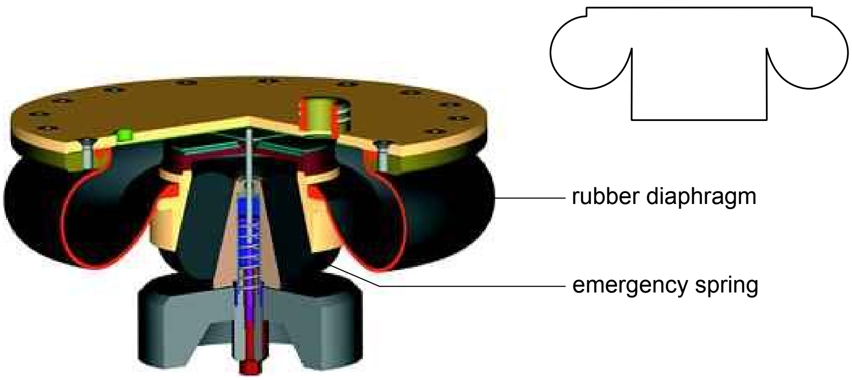

Figure 1.9: Illustration of a railway airpsring and schematic representation (picture from *http://www.phoennix-ag.com*).

Levelling valves

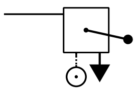

The levelling valve controls air admission or exhaust in the bellows in order to maintain a constant height between the carbody and the bogie when the carbody load varies. It is controlled by a lever connected:

- to the bogie frame if the valve is fixed to the carbody,
- to the carbody if the valve is fixed to the bogie frame.

As the bogie-carbody vertical distance becomes too small, the lever connects the bellows to the pressure source and air is admitted into the suspension resulting in an increase of the pressure so as to restore the initial bogie-carbody distance. On the contrary, if the distance is too large, the lever connects the bellows to the atmosphere and air exhausts (see Fig. 1.10). This principle is particularly useful, for instance, when numerous passengers exit or enter a metro.

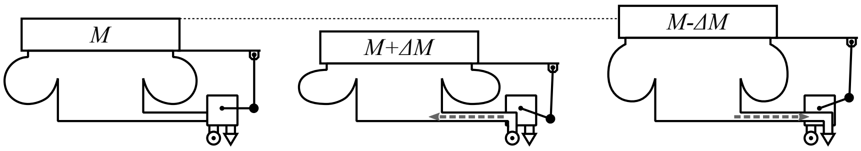

Figure 1.10: Illustration of the levelling valve functioning.

Safety valves

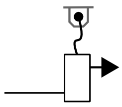

The safety valve, also called exhaust valve, is connected to the bellows or to the auxiliary tank. It operates as a “mechanical fuse”: when the bogie-carbody height exceeds a fixed-value, a sudden airflow passes through the valve from the bellows to the atmosphere. It can for instance be engaged when the levelling valve is accidentally locked in admission and inflating continuously the bellows.

Differential pressure valve

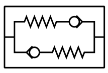

The differential pressure valve is located between the two bellows or the two auxiliary tanks of one bogie. It is intended to avoid too large pressure differences between the right and left bellows: an airflow appears when the pressure difference between its connections exceeds a fixed value, often fixed between 1 and 2.25 *bar*. It can occur when one air bag is punctured or when the vehicle passes through a twisted track, i.e. the situation in which the two rails are not parallel (see Fig. 1.11), which is typical in a curve entry.

Pressure source

The compressed air is provided by a compressor often located under the carbody. It constitutes a pressure source at around 8 *bar* (relative pressure) that

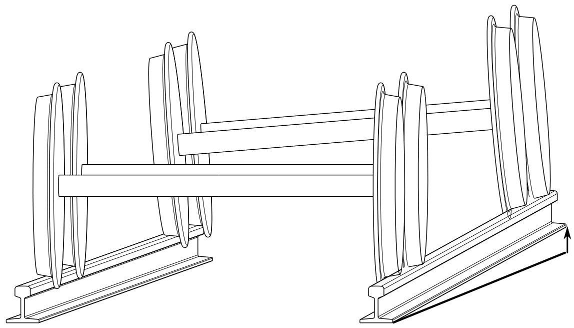

Figure 1.11: Illustration of a rail twist.

is used for both the pneumatic suspension and the braking system.

A common suspension circuit often contains other components such as a mean pressure gauge that gives information about the load in the carbody and is intended to indicate whether a bellows is punctured, maximal pressure valve to limit the maximal pressure, etc. Those components will not be considered in this work because they a priori do not affect the vehicle behaviour. However, as we will show later, the retained approach proposes to consider them if necessary.

All the previous components can be connected in several ways as illustrated in Fig. 1.8. A major variant involves the levelling system for which many configurations exist, but they can generally be likened to one of the following cases. Let us consider a carbody carried by two bogies via two air springs per bogie.

- The *four-point configuration* (see Fig. 1.12(a)) consists in placing four levelling valves per carbody. There are thus two levelling valves on a same bogie, one for each bellows. This configuration provides height levelling when the payload is varying and also compensates for the lateral acceleration in curve by inflating outer bellows and deflating inner bellows. It is generally used in combination with a differential pressure valve between the two bellows to limit the wheel force variations when the vehicle passes through a twisted track.

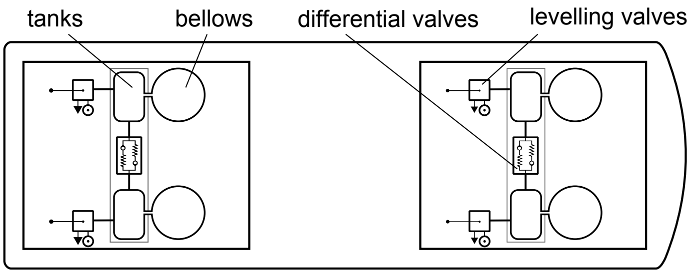

(a) A four-point suspension.

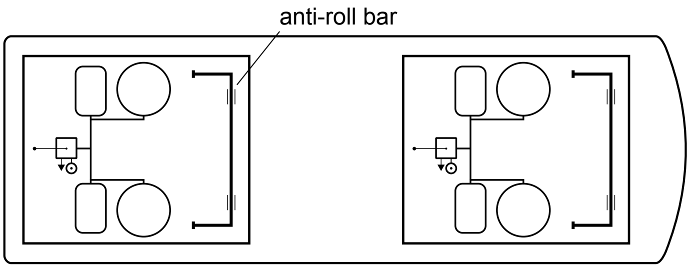

(b) A two-point suspension.

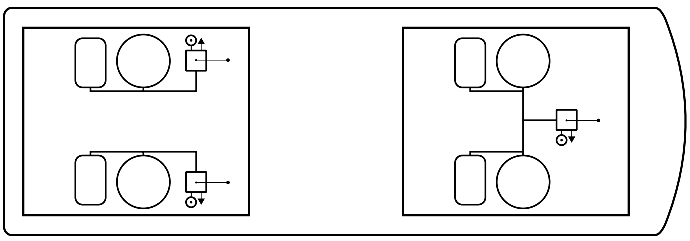

(c) A three-point suspension.

Figure 1.12: Schematic top view of a carbody carried by two bogies and equipped with various levelling configurations.

- The *two-point configuration* (see Fig. 1.12(b)) uses two levelling valves per carbody. The differential pressure valve of the four-point suspension is replaced by a connecting pipe and there is thus only one levelling valve for the two bellows of the same bogie. In this case, the system only ensures height levelling and has no roll stiffness since the pressure is always the same in the two bellows. An anti-roll bar is therefore needed to prevent the carbody from reaching the bumpstops.

- The *three-point suspension* (see Fig. 1.12(c)) consists of an hybrid configuration: one bogie presents a two-point configuration while the other one is equipped with a four point configuration. There is thus three levelling valves per carbody. In this case, the bogie equipped with two-levelling valves will compensate for all the roll excitation in curve, inducing a higher pressure difference between the inner and the outer bellows than the four-point case. The EN 14363 European Standard (see Ref. [1]) also mentions a three-point configuration with a longitudinal connection (see Fig. 1.13(a)): three levelling valves are each connected to one bellows. The fourth bellows is then connected to the bellows on the same side of the other bogie. However, this solution is not often used in practice.

Other criteria can influence the pneumatic circuit topology such as the kind of bogie. For instance if a so-called Jakob's bogie is used, i.e. a bogie placed between two carbodies, all the bellows can be connected together as illustrated in Fig. 1.13(b).

Another suspension modification consists in removing the anti-roll bar and the vertical damper so as to simplify the suspension, the damping being ensured by pneumatic means only. In this case, the two-point levelling system is not possible.
Therefore, many suspension morphologies can be imagined by combining the various parameters such as the kind of bogies, the use of an auxiliary tank, the use of additional hydraulic dampers, etc., some combinations obviously being impossible (see Fig. 1.14).

1.3.3 Pneumatic suspension modelling

Motivation

From an industrial point of view, it appears that the choice among the various pneumatic suspension morphologies presented in section 1.3.2, for a given customer, is partly achieved out of habit. For instance, the use of a specific valve

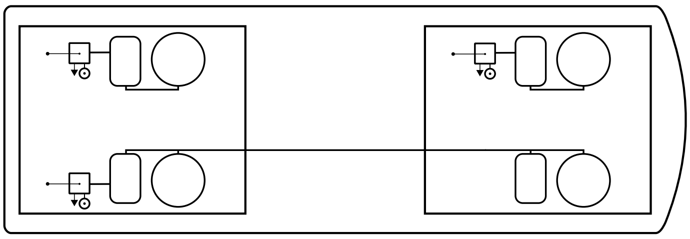

(a) A three-point suspension with longitudinal connection.

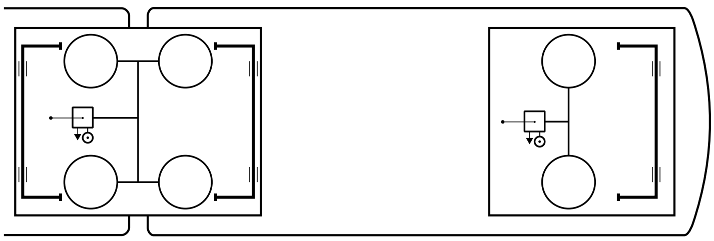

(b) A two-point suspension with a Jakob's bogie.

Figure 1.13: Schematic top view of other levelling configurations.

can be imposed by the customer specifications because it was used on previous vehicles. Actually, the tendency is to reuse well-proven bogie architectures and to make only little changes when designing a new vehicle. Too important modifications could lead to undesired behaviour that would be revealed only during experimental assessment after the vehicle design. Obviously, this approach is not very encouraging to propose innovative suspension morphologies. Furthermore, it does not guarantee that the pneumatic suspension used on an old vehicle will be efficient on a new one, for instance because other properties of the vehicle have changed.

Nevertheless, as for many other fields of engineering, computer aided techniques have become more and more used in the railway industry as depicted by Evans and Berg (Ref. [25]). Finite element techniques are well adapted in order to design specific parts of the bogie such as the frame or the wheelsets. On the other hand, multibody dynamics is especially adapted to analyse the

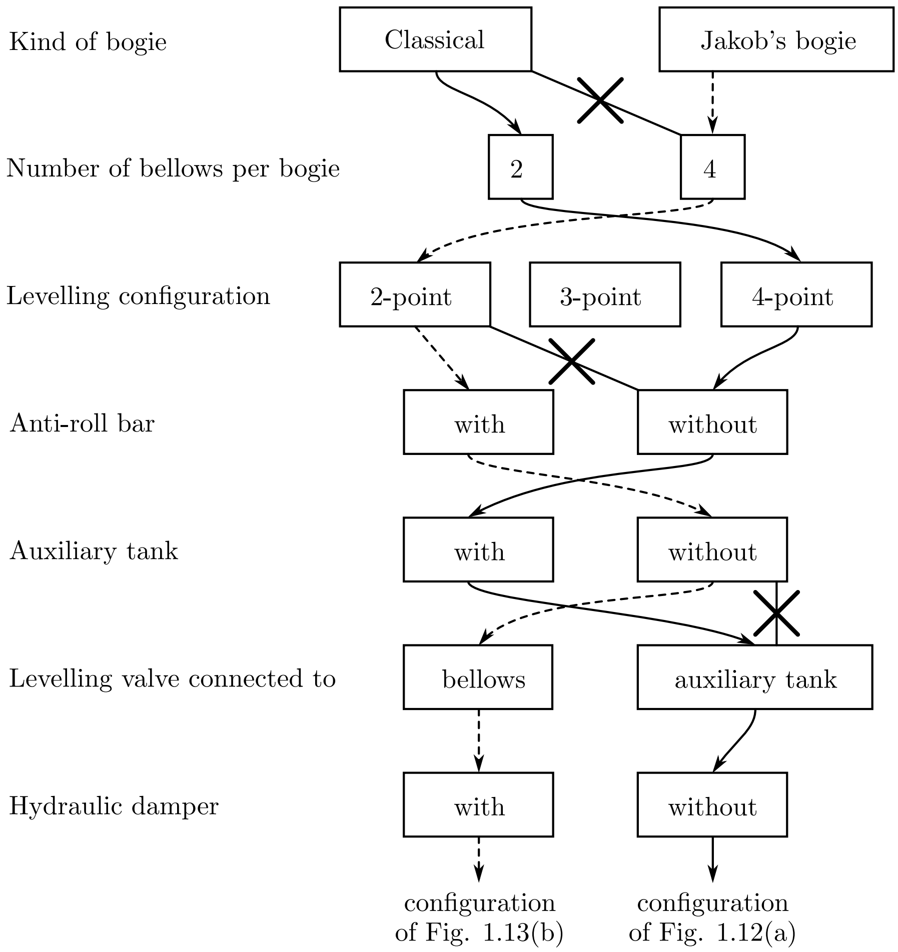

Figure 1.14: Secondary suspension design diagram with two configurations examples: the continuous lines corresponds to a metro and the dashed lines to an intercity train.

dynamic behaviour of the whole train set. It allows engineers to check some vehicle properties such as stability, comfort, etc, directly from the drawing board. Furthermore, much research has been conducted in order to partly replace full-scale experimental testing by computer analysis in the vehicle acceptance process (see Ref. [45]). This is justified by the cost reduction and the decreasing availability of test tracks, partly due to the separation of infrastructure and train operators. Moreover, virtual testing allows to analyse configurations that are difficult to test in practice and gives access to numerical quantities difficult to measure. However, special attention has to be paid to take into account varying running conditions such as the weather, that may strongly impact the wheel/rail friction phenomena.
That justifies the need for accurate and efficient models. Regarding the pneumatic suspension, a suitable modelling tool allows us to more deeply analyse vehicle performances like stability or passenger comfort but also to deal with pneumatic circuit specific concerns such as the valve design, the air consumption calculation or the analysis of a valve failure. Moreover, it is worth noting that the last version of the UIC 518 (see Ref. [4]) standard has introduced the necessity to check the influence of the so-called *failure mode*, referring to the secondary suspension explicitly.
The framework of our work has therefore been set to develop novel models and numerical tools in order to understand in depth railway pneumatic suspension dynamics. This can help quantifying suspension morphology performances and proposing optimal design with respect to the various industrial criteria.

Existing approaches

In order to be integrated into a complete vehicle model, it is needed to calculate the bellows reaction forces on the bogie frame and on the traverse, for given relative positions and velocities of those two bogie parts. Various modelling approaches have already been proposed in the literature. Most of the time, they focus on a subsystem composed of one air spring connected to an auxiliary tank via a pipe.
The most simple modelling technique consists in replacing the air springs by equivalent springs and dampers. More sophisticated combinations of serial and parallel springs and dampers enable to take a frequency dependent stiffness in the vertical direction into account, because air flow toward the tank saturates

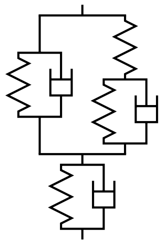

(a) Linear spring-damper model.

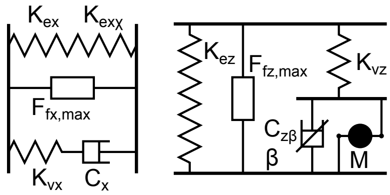

(b) Berg's model.

Figure 1.15: Illustration of bellows-tank equivalent mechanical model.

when the frequency increases. The working air volume is thus reduced and the stiffness rises.
Furthermore, the air present in the connecting pipe can induce a resonance effect due to its inertia. That effect can be taken into account by an additional mass as proposed by Eickhoff et al. in Ref. [24] or by Berg in Refs. [12] and [13]. The approach used by Berg, illustrated in Fig. 1.15(b), proposes a three-dimensional model and distinguishes three main behaviours of the pneumatic suspension:

- the elastic behaviour mainly due to the air compression,
- the friction behaviour induced by the airbag rubber,
- the viscous and singular loss behaviour due to the flow in the pipe.

In Ref. [12], this model is also confronted to a large number of experimental measurements and it is shown how the model parameters can be derived from those experiments.
Another approach consists in calculating the pressure in the bellows and the tanks and then deducing the corresponding force. For instance, in Ref. [65], the air in the pipe is considered as being a constant mass that oscillates between the air spring and the tank inducing volume variation in these devices. Position of the mass is given by its equation of motion and pressure variations are calculated according to the polytropic relations. The Simpack software also provides some possibilites of connecting several bellows together and of considering control valves (see Ref. [70]). However, the proposed procedure

is quite limited in terms of topology and application and the meaning of the model parameters is not straightforward.
In Ref. [55], Quaglia et al. propose to calculate the mass flow between the bellows and the tank according to the ISO 6358 standard (see Ref. [3]). Pressure variations in pneumatic chambers are calculated by considering the mass conservation and polytropic transformations. This approach is used to derive a dimensionless model of an air spring connected to an auxiliary tank via a restriction orifice.
In Ref. [48], Nieto et al. use a similar approach but consider isothermal transformations in the chambers and consider that the flow between the tank and the air spring can be likened to a discharge process.
In Ref. [68], Toyofuku et al. analyse the effect of the pipe using finite differences discretization but it is also shown that considering an incompressible flow in the pipe is sufficient to reveal the resonance effect due to the air inertia.
Facchinetti et al. (Ref. [26]) also use the mass conservation for the chambers and a mass flow formulation for the connecting pipe so as to establish a model calibrated with experimental results. They emphasise that the pipe air inertia must be taken into account so as to correctly assess the vehicle ride comfort, especially when auxiliary tanks are placed far from the bellows. They also show the importance of coupling effects between roll and lateral deformations whereas the air spring vertical behaviour can be considered separately. The impact of the air spring modelling on the accuracy of simulations is also analysed in Ref. [5]. In most of the previous references, the model air spring properties such as its volume-displacement relation are deduced from experimental tests. In Ref. [54], Qing and Yin propose to determine analytically the volume-displacement relation by analysing the geometry of the air spring shell. However, this approach is limited to cushions for which the shell section is almost circular and still require experiments to determine some geometrical properties.

Developed approach

In most of the cases, the proposed models in the literature concentrate on the bellows-tank subsystem which cover a certain number of running conditions, especially in the case of simple pneumatic morphology such as the four-point configuration in which the action of valves is not considered. However, it is quite often needed to take the influence of valves into account and to model complex pneumatic circuit configurations. Approaches based on equivalent spring-mass systems are of course not extendible to more complicated morphologies. On the contrary, using a formulation based on the energy and mass balances for open system permits to connect together as many components as needed. We therefore will concentrate on that kind of modelling approach, the goal of our work being to choose the most suitable model according to the problem to be analysed.

Chapter 2

Pneumatic modelling: development and formulation

As presented in the previous chapter, the modelling of pneumatic circuit is a challenging task especially within the framework of multiphysics dynamics. In order to be coupled with multibody dynamics, the pneumatic model must accurately provide the pneumatic actuator forces for given positions and velocities of the mechanical system. Additionally, it must also reveal how the various components of the suspension interact so as to understand the phenomena that occur under different running conditions. This chapter is therefore dedicated to the modelling of pneumatic circuit components and more specifically to railway pneumatic suspensions. We will focus on the vertical motion of the suspension since it is more affected by pneumatic dynamics than the horizontal motion. Furthermore, it was shown in Ref. [26] that the vertical dynamics is not affected by the lateral or roll deformations of the cushions while the two latter cannot be decoupled.

The various components of a pneumatic circuit will be modelled using energy and mass balances because it offers the possibility to connect each element in many ways and it is therefore more suitable to deal with rather complex and different circuit morphologies. The developed approaches will be compared

with the existing techniques presented in Section 1.3.3.
Three main kinds of pneumatic components are considered:

- pneumatic chambers,
- pipes and restriction orifices,
- valves.

Railway bellows are a special kind of pneumatic chamber and imply a specific modelling explained in Section 2.1. Then we will present a benchmark used to compare the various models. Two models from the literature will be detailed before the modelling of each component. We will especially focus on the pipe flow for which the various approximations strongly affect the results obtained for the defined test case.

2.1 Air spring specificities

Air springs constitute a particular case of pneumatic chambers. They represent the main interface between the multibody and pneumatic subsystems. Pneumatic chambers will be detailed in Section 2.4 but some bellows specificities are introduced in this section.
For the pneumatic modelling, the air spring internal volume has to be known. As suggested in [55] and as we have observed on experimental tests analysed in Chapter 3, we can assume that it only depends on the air spring height (which is an output of the multibody model) and not on the internal pressure. Moreover, as a first approximation, the variation is assumed to be linear with the air spring elongation (Ref. [55]). From a modelling point of view, this is not a restrictive assumption and more general functions could be considered if experimental measurements are performed. We thus have:

$$V_b(z) = V_{b0} + \frac{dV_b}{dz} z; \tag{2.1}$$

where z is the bellows upper plate displacement (positive when the upper plate is moving upward). As explained later, the air spring pressure is provided by the pneumatic chamber model but the multibody model requires the actuator forces. The relation between those two quantities is defined by the so-called *effective area*:

$$F = A_e(p_b - p_a) \ , \tag{2.2}$$

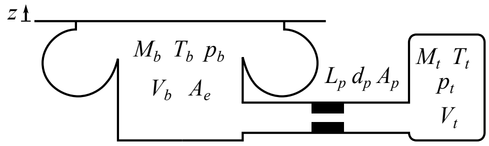

Figure 2.1: Illustration of the bellows-tank subsystem.

where p_b is the absolute pressure in the bellows $[Pa]$;
p_a is the atmospheric pressure $[Pa]$;
A_e is the bellows effective area $[m^2]$.

The effective area A_e can be deduced from experimental force-pressure curves. It can depend on the bellows height and pressure. As proposed in [55], we assume that A_e does not depend on p_b and we consider a linear variation with bellows elongation. This hypothesis will be confirmed by experiments carried out on an actual vehicle suspension in Chapter 3. We thus have:

$$A_e(z) = A_{e0} + \frac{dA_e}{dz} z \tag{2.3}$$

Note that the present work concentrates on spring forces due to air transformations only while the emergency spring effects are not considered. Depending on the cushion configuration, the emergency spring is in series or in parallel, leading to different modelling approaches. If it is in parallel, it can be taken into account simply by adding its reaction force to the pressure force. If it is placed in series, an additional state variable or a constraint between the gas spring crushing and the emergency spring displacement will be necessary.

2.2 Comparison benchmark

In order to validate the proposed models, a simple test case is defined which corresponds to a classical suspension manufacturer experiment. It consists of a bellows connected to an auxiliary tank via a pipe, as illustrated in Fig. 2.1. Using this simplified assembly allows us to consider equivalent spring-mass system approach in the model assessment, what would not be possible if valves were added.

A sinusoidal displacement excitation is applied on the upper plate of the air

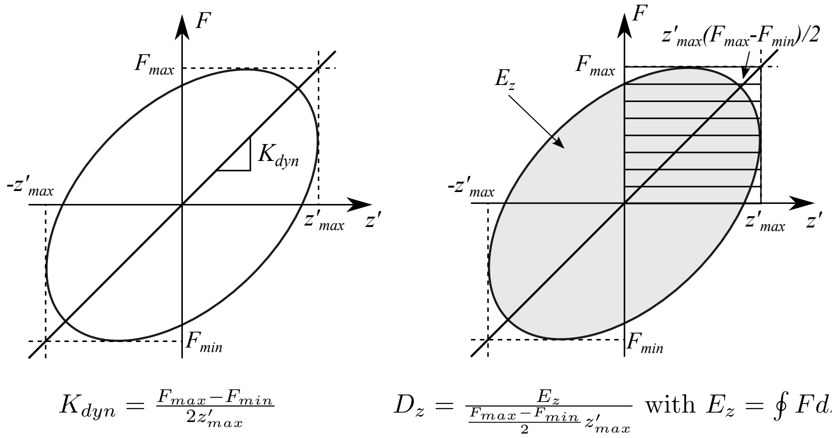

Figure 2.2: Dynamic stiffness K_{dyn} and damping coefficient D_z definition in a similar way to [12] (the bellows crushing $z' = -z$ is positive when the bellows upper plate moves downwards).

spring with a frequency f varying from 0.1 to 30 Hz:

$$z = z_{max} sin(2\pi f t). \tag{2.4}$$

The bellows reaction force history is thus calculated and force-displacement diagrams are drawn. The obtained graphs look like ellipses of which the main axis slope and area are related to the suspension *dynamic stiffness* and *damping*, respectively. Those quantities can be defined in two ways.
First, the dynamic stiffness can be defined as the ratio between the force variation amplitude and the displacement amplitude and the damping can be deduced from the ellipse area as illustrated in Fig. 2.2. A second method consists in computing an harmonic decomposition of the reaction force and considering the fundamental mode:

$$F \approx F_{max} sin(2\pi f t + \phi). \tag{2.5}$$

The ratio F_{max}/z_{max} corresponds to the dynamic stiffness and the phase ϕ is an image of the damping.

According to Quaglia et al. (Ref. [55]), for slow motions, the *quasi-static stiffness* of the bellows-tank subsystem, in the case of reversible adiabatic trans-

Nominal bellows volume	V_{b0}	11.6 dm^3
Bellows volume gradient	dV_b/dz	0.13 m^2
Effective area	A_e	0.13 m^2
Effective area gradient	dA_e/dz	0.0 m
Tank volume	V_t	27 dm^3
Pipe length	L_p	1 m
Pipe diameter	d_p	18 mm
Initial pressure	p_0	4 bar
Initial temperature	T_0	293 K

Table 2.1: Parameters used for the bellows-tank test case.

formations, can be approximated by:

$$K \approx \gamma \frac{A_e \frac{dV_b}{dz} p_0}{V_{b0} + V_t} - (p_0 - p_a) \frac{dA_e}{dz}, \tag{2.6}$$

with γ the specific heat ratio coefficient, p_0 the initial pressure and V_t the auxiliary tank volume. If isothermal transformations are considered, it becomes:

$$K \approx \frac{A_e \frac{dV_b}{dz} p_0}{V_{b0} + V_t} - (p_0 - p_a) \frac{dA_e}{dz}, \tag{2.7}$$

The first term is related to the *volumetric stiffness* and is due to the bellows volume variation and the resulting pressure variation. The second term, the *area stiffness*, comes from the effective area rise when the cushion is crushed which results in a force increase even though the pressure is constant. Since dA_e/dz is negative, it has a positive contribution.

In this chapter, we will consider the case of an air spring without effective area variation. This assumption will allow us to ensure the correspondence between the parameters of the various considered models. Table 2.1 lists the main parameters used in this chapter for the test case. With those values, the quasi-static stiffness of the suspension are given in Table 2.2.

	Adiabatic	**Isothermal**
Bellows-tank stiffness	245 kN/m	175 kN/m
Bellows only stiffness	816 kN/m	583 kN/m

Table 2.2: Quasi-static stiffness of the suspension.

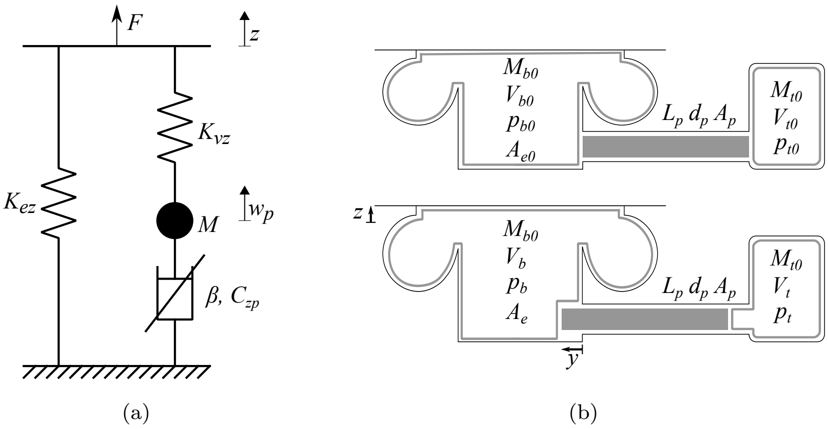

Figure 2.3: (a) Illustration of the "equivalent mechanical" model (Ref. [67]); (b) Illustration of the SIMPACK model.

2.3 Monolithic bellows-tank models

Before detailing the thermodynamical model of each component, we present in more details two approaches from the literature dedicated to the bellows-tank subsystem.

2.3.1 "Equivalent mechanical" model

This first model, developed by Berg (see Ref. [12, 13]), likens the air spring to a spring-mass system with a non-linear damper in series and a second spring in parallel. In Fig. 2.3(a), only the vertical elements that take elastic and viscous effects into account are represented while the complete model is three-dimensional and also consider the friction behaviour of rubber. The effect of the pipe air mass is modelled by the mass M and the non-linear damper in serie. It is suggested in [13] to take a damping term proportional to $\dot{w_p}^{\beta}$ where

Parallel spring stiffness	K_{ez}	245	kN/m
Serial spring stiffness	K_{vz}	571	kN/m
Serial mass	M	155	kg

Table 2.3: Parameters of the “equivalent mechanical” model.

w_p is the mass displacement and β has a value between 1 and 2.
In practice, the parameter must be determined on the basis of experimental tests performed on a real suspension. However, the link between the parameters of figure 2.3(a) and the physical parameters (volume, effective area, pipe diameter...) is presented in Refs. [67] and [53] in the case of a cylindrical air spring for which $dA_e/dz = 0$ and $dV_b/dz = A_e$. The parameters corresponding to the air spring analysed in this chapter are listed in Table 2.3 for the case of adiabatic transformations. Note that K_{ez} corresponds to the quasi-static stiffness of the bellows and the tank and that the sum $K_{ez}+K_{vz}$ to the quasi-static stiffness of the bellows alone.

2.3.2 Oscillating air mass model

The Simpack software (FE 82 in Ref. [65]) proposes an air spring model illustrated in Fig. 2.3(b): it considers the air in the pipe as a constant moving mass and computes its position and velocity by solving its equation of motion:

$$m_p\ddot{y} + \frac{\rho_p}{2}\left(\lambda\frac{L_p}{d_p} + \zeta\right) A_p\dot{y}^2 sign(\dot{y}) + (p_b - p_t)\, A_p = 0\ , \tag{2.8}$$

with: m_p, the air mass in the pipe $[kg]$;
ρ_p, the air density $[kg/m^3]$;
y, the air mass displacement $[m]$;
$\dot{y}$, the air mass velocity $[m/s]$;
$\ddot{y}$, the air mass acceleration $[m/s^2]$;
L_p, the pipe length $[m]$;
d_p, the pipe diameter $[m]$;
A_p, the pipe section $[m^2]$;
λ, the distributed loss coefficient $[-]$;
ζ, the lumped loss coefficient for singularities $[-]$;
p_b, the bellows pressure $[Pa]$;
p_t, the tank pressure $[Pa]$.

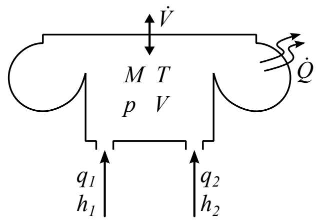

Figure 2.4: Illustration of the pneumatic chamber modelling.

With this approach, the effect of bends, orifices and other pipe singularities is taken into account by the singular loss coefficient. This coefficient can be estimated as the sum of the loss coefficients of each singularity that can be found in tables such as Idel'cik (Ref. [38]).
The air motion induces volume variations in the bellows and the tank and therefore causes pressure fluctuations given by the isentropic equation:

$$pV^k = p_0 V_0^k \ , \tag{2.9}$$

where: V is the volume of the bellows or the tank $[m^3]$;
p is the pressure of the bellows or the tank $[Pa]$;
subscript 0 refers to initial conditions;
k is the polytropic exponent.

The case $k = \gamma$ corresponds to reversible adiabatic transformations and the case $k = 1$ to isothermal transformations.

2.4 Pneumatic chamber model

Bellows and tanks are modelled as pneumatic chambers in which the mass, the temperature and the pressure vary because of the flow coming from the connected pipes or from the valves (see Fig. 2.4).

The continuity equation imposes that the air mass time derivative is directly given by the total mass flow rate entering the chamber:

$$\frac{dM}{dt} = \dot{M} = \sum_i q_i \ , \tag{2.10}$$

where: M is the mass in the chamber;
q_i is an entering mass flow through port i.

The temperature variation is deduced from the internal energy variation using the first law of thermodynamics applied to an open system:

$$\frac{dT}{dt} = \dot{T} = \frac{\gamma - 1}{RM} \left(\sum_i q_i h_i - \frac{RT}{\gamma - 1} \sum_i q_i - \frac{dQ}{dt} - p\frac{dV}{dt} \right) \ , \tag{2.11}$$

where: T is the temperature in the chamber;
$q_i h_i$ is the total enthalpy flow rate at each pipe or valve connection;
dQ/dt is the heat flow rate;
p is the pressure in the chamber;
V is the volume of the chamber;
γ is the specific heat ratio;
R is the perfect gas constant.

In case of tanks, being rigid, the volume variation with time, dV/dt, vanishes. For bellows dV/dt is derived from Eq. (2.1):

$$\frac{dV}{dt} = \dot{V} = \frac{dV_b}{dz}\dot{z}; \tag{2.12}$$

$\dot{z}$ being supplied by the multibody model.
Concerning the heat flow rate term dQ/dt, a first solution is to assume that it is proportional to the temperature difference between the pneumatic chamber and the atmosphere:

$$\frac{dQ}{dt} = \dot{Q} = h_{eq}\left(T - T_a\right) \ , \tag{2.13}$$

where: T is the temperature in the chamber $[K]$;
T_a is the atmospheric temperature $[K]$;
h_{eq} is a heat transfer coefficient $[W/K]$.

A key point is to estimate the heat transfer coefficient h_{eq} since it depends on many parameters such as the component shape and material. It is all the more difficult for the bellows because they are composed of several materials, often rubber and steel, with their own physical properties. As an illustration, Fig. 2.5 shows the reaction force of an airspring submitted to a 20 mm ramp displacement excitation for various values of the heat transfer coefficient. The null value corresponds to the adiabatic hypothesis while for values larger than 10^3 W/K,

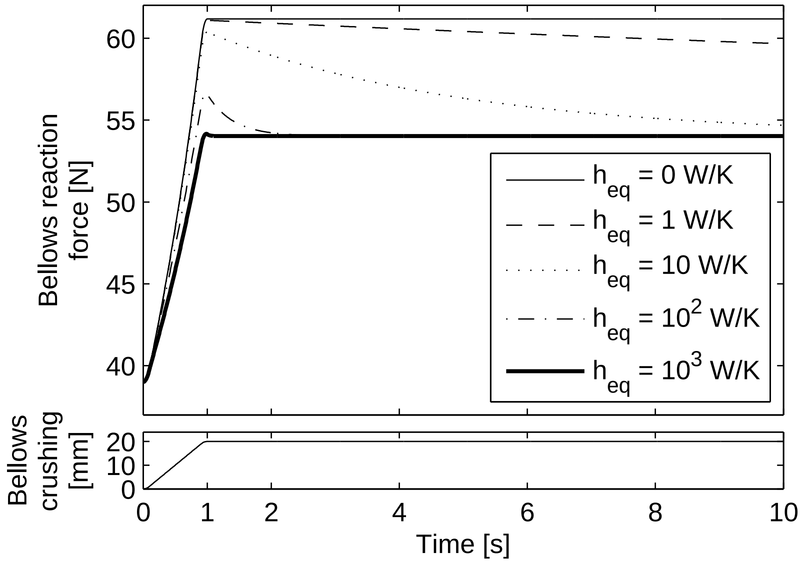

Figure 2.5: Reaction force of a bellows submitted to a 20 mm compression excitation.

the transformation can be reasonably considered as isothermal. Between those two extreme cases, one can clearly distinguish the intermediate behaviours: for transfer coefficients greater than 0 W/K and lower than 10 W/K, the force reaches the adiabatic value and then decreases toward the isothermal level.
A more refined solution consists in taking the thermal inertia of the component wall into account assuming that the temperature in the material is uniform which leads to the following lumped formulation:

$$\begin{array}{rcccl} \frac{dQ}{dt} & = & \dot{Q} & = & h_i(T - T_w); \\ \frac{dT_w}{dt} & = & \dot{T}_w & = & \frac{1}{mc}\left(h_a(T_a - T_w) + h_i(T - T_w)\right); \end{array} \tag{2.14}$$

where: T_w is the chamber wall temperature $[K]$;
m is the mass of the chamber wall $[kg]$;
c is the heat capacity of the chamber wall $[J/kg/K]$;
h_i is a heat transfer coefficient between the wall and the interior $[W/K]$;
h_a is a heat transfer coefficient between the wall and the atmosphere $[W/K]$.

This second approach requires the estimation of three parameters which makes the model calibration more difficult.

Given the temperature and the mass in the chamber, the pressure is deduced assuming a perfect gas :

$$pV = MRT \ . \tag{2.15}$$

This approach allows us to connect several components to bellows or to tanks simply, by considering several mass flows entering in the chamber. In the case of the bellows-tank subsystem, we therefore have to calculate the mass flow rate in the pipe as a function of the bellows and tank pressures and temperatures.

2.5 Pneumatic pipe and orifice modelling

2.5.1 Incompressible flow approach

Incompressible differential model. The first approach consists in assuming a one-dimensional incompressible flow through the pipe. Starting from Eq. (2.8) used for the oscillating mass model and since the air density ρ_p in the pipe is constant, the mass flow is proportional to the air velocity $q_{tb} = \rho_p A_p \dot{y}$ and can be computed as follows (Ref. [21]):

$$\dot{q}_{dif} = \frac{A_p}{L_p}\left((p_1 - p_2) - \frac{1}{2\rho_p A_p^2}\left(\lambda \frac{L_p}{d_p} + \zeta\right) q_{dif}^2 sign(q_{dif})\right) \ , \tag{2.16}$$

with: q_{dif}, the mass flow rate in the pipe $[kg/s]$;
ρ_p, the air density $[kg/m^3]$;
L_p, the pipe length $[m]$;
d_p, the pipe diameter $[m]$;
A_p, the pipe section $[m^2]$;
λ, the distributed loss coefficient $[-]$;
ζ, the lumped loss coefficient $[-]$;
p_1, the pressure at port 1 $[Pa]$;
p_2, the pressure at port 2 $[Pa]$.

Incompressible algebraic model. Neglecting the dynamics in equation (2.16), one obtains an algebraic equation for the steady state mass flow rate:

$$q_{alg} = \sqrt{\frac{2\rho_p A_p^2}{\lambda \frac{L_p}{d_p} + \zeta} |p_1 - p_2| sign\left(p_1 - p_2\right)} \ , \tag{2.17}$$

Note that introducing Eq. (2.17) into the the incompressible differential equation (2.16), we obtain the following relation between the two approaches:

$$\dot{q}_{dif} = \frac{\lambda L_p/d_p + \zeta}{2\rho_p A_p L_p} \left(q_{alg}^2 sign(p_1 - p_2) - q_{dif}^2 sign(q_{dif})\right) \ . \tag{2.18}$$

Heat transfer. In order to be coupled with the pneumatic chamber equations (2.10) and (2.11), the pipe model must provide the exiting and entering flow temperatures so as to calculate the total enthalpy flow rate. For the exiting flow, it can be considered that the temperature is that of the chamber. For the entering flow, various hypothesis can be stated:

- the flow is adiabatic and the temperature to be considered is the temperature of the chamber from which the flow is coming;
- the heat transfer is such that the flow enters at the temperature of the chamber;
- the heat transfer with the atmosphere is very important and therefore the flow enters with the atmosphere temperature;
- the heat transfer is significant but different from the previous cases, it therefore must be calculated to know the entering enthalpy flow rate.

Model comparison. Considering the equations of pneumatic chambers and pipes, it is now possible to analyse the behaviour of the bellows-tank subsystem for the test case defined in Section 2.2 and compare the proposed approaches with models of the literature presented in Section 2.3. The following models will be discussed:

- ***Model 1*** is the "equivalent mechanical" model described in Section 2.3.1. In Ref. [12], it is proposed to take a damping exponent β between 1 and 2 but it is shown that the value $\beta = 1.8$ provides the best match with experimental tests. However, since the damping term is proportional to

$\dot{y}^2$ in *model 2* and to q_{tb}^2 in *models 3* and *4*, we choose $\beta = 2$ for the damping exponent in order to correctly compare the models.

- ***Model 2*** is the oscillating air mass model presented in Section 2.3.2.
- ***Model 3*** combines the differential incompressible pipe model (Eq. (2.16)) with pneumatic chamber equations (2.10) and (2.11).
- ***Model 4*** is similar to *model 3* but uses the algebraic equation (2.17) for the pipe mass flow instead of the differential equation (2.16).
- ***Model 5*** corresponds to the model proposed by Quaglia in [55]. It is the same as *models 3* and *4* but uses the ISO 6358 norm (Ref. [3]) to calculate the flow between the bellows and the tank:

$$\begin{aligned} q_{iso} &= C p_1 \rho_{ref} \sqrt{\frac{T_{ref}}{T_1}} && \text{if } \frac{p_2}{p_1} \leq b; \\ q_{iso} &= C p_1 \rho_{ref} \sqrt{\frac{T_{ref}}{T_1}} \sqrt{1 - \left(\frac{\frac{p_2}{p_1} - b}{1-b}\right)^2} && \text{if } \frac{p_2}{p_1} > b; \end{aligned} \tag{2.19}$$

where: subscripts 1 refer to upstream conditions ($max(p_b, p_t)$);
subscripts 2 refer to downstream conditions ($min(p_b, p_t)$);
subscripts ref refer to reference conditions ($T_{ref} = 293.15\ K$ and $p_{ref} = 1\ bar$);
C is the sonic conductance $[sm^4/kg]$;
b is the critical pressure ratio $[-]$.

Concerning the heat transfer question for *models 3, 4* and *5*, we assume that the flow enters at the chamber temperature because it corresponds to the hypothesis implicitly taken in *models 1* and *2*.
These five models have been implemented in Matlab/Simulink and integrated using the classical *ode45* time integrator. This algorithm is based on the explicit Runge-Kutta method and uses the Dormand-Prince scheme which relies on fourth order and fifth order schemes to control the time step size (see Ref. [23] for more details).

Fig. 2.6 shows two groups of curves when computing the dynamic stiffness and damping coefficient of the system: the first group with the models that use a differential equation for the pipe (*models 1, 2* and *3*) and the second group with those that use an algebraic equation (*models 4* and *5*). Let us mention

Model 1		
Damping exponent	β	2
Damping coefficient	C_{zp}	$54.71\ kN(s/m)^{\beta}$
Models 2, 3 and *4*		
Total pressure drop coefficient	$\lambda\frac{L_p}{d_p}+\zeta$	1.98
Model 5		
Sonic conductance	C	$370\ 10^{-9} sm^4/kg$
Critical pressure ratio	b	0.53

Table 2.4: Pipe parameters for the model comparison.

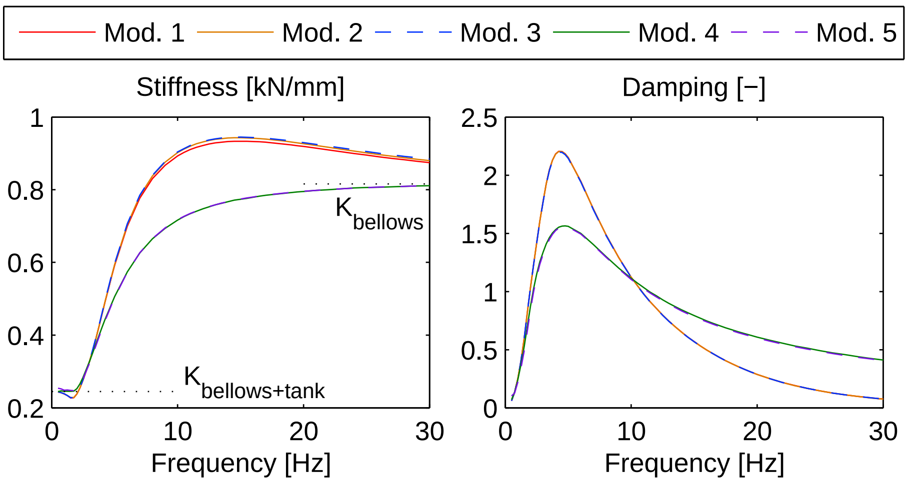

Figure 2.6: Comparison of dynamic stiffness K_{dyn} and damping coefficient D_z for the presented models (excitation amplitude $z_{max} = 10\ mm$).

that, lacking of experimental data, the sonic conductance C of *model 5* was tuned to fit the *model 4* curves.
In all cases, the dynamic stiffness curves exhibit two constant levels. The low frequency one corresponds to the excitation of the bellows and the tank. The high frequency one corresponds to the excitation of the bellows alone as air cannot pass through the pipe and the orifice quickly enough.
Between the two, the models using a differential equation (*models 1, 2* and *3*) exhibit a resonance effect due to the inertia of the air mass in the pipe. Starting from the low frequencies, the dynamic stiffness first decreases. Indeed, around 1.75 Hz, when the bellows crushing is maximal, the mass flow is still positive (towards the tank) while it would be null for a very slow excitation. This small phase angle difference tends to limit the pressure increase due to the compression. A similar effect occurs for the maximal stretching: air is still flowing from the tank to the bellows, limiting the pressure decrease due to the expansion. Consequently, the dynamic stiffness is lower than for quasi-static deformations.
When the frequency increases, the phase difference becomes greater. Around 15 Hz in Fig. 2.6, the air mass moves toward the tank when the air spring is stretched increasing the pressure decrease due to the expansion. A similar but inverse phenomenon occurs when the air spring is crushed, explaining why the dynamic stiffness is larger than the stiffness of the bellows alone.

Influence of the excitation amplitude. Fig. 2.7 compares *models 1* and *3* for several excitation amplitudes. For larger amplitudes, *model 1* shows lower resonance effects on the stiffness curve than the *model 3* in the 8 Hz to 20 Hz range. This difference is due to the use of a linear spring to model elastic effects of the bellows in *model 1* instead of the non-linear isentropic equation of thermodynamical models. This clearly appears in Fig. 2.8 that compares *models 1* and *3* for a 14 Hz excitation which corresponds to the maximal stiffness (see Fig. 2.7). For a 5 mm excitation, the force-displacement diagram looks like an ellipse for the two models. However, for the 20 mm, the *models 3* curve exhibits a second order curvature due to the isentropic relation non-linearity.
Whatever the model, we observe in Fig. 2.7 that the resonance effect is less

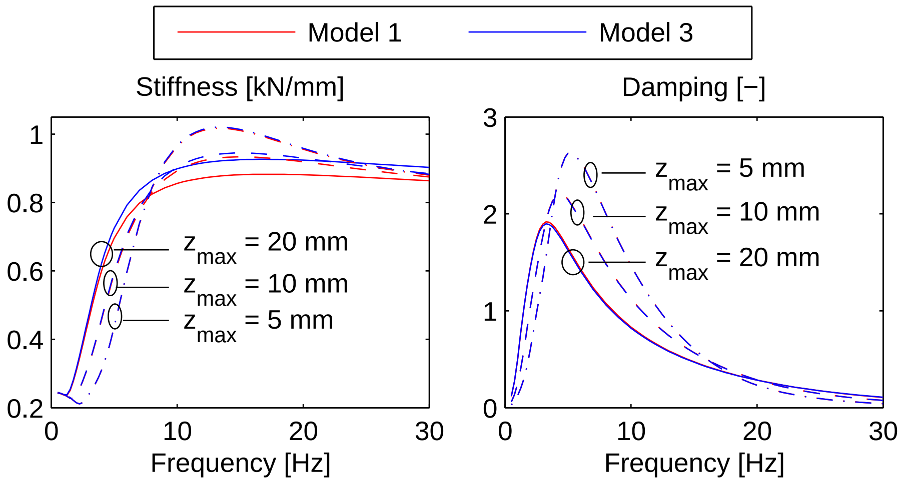

Figure 2.7: Influence of the excitation amplitude on dynamic stiffness K_{dyn} and damping coefficient D_z.

important for large amplitudes. We also notice that all curves cross each other in the same zone between 7 Hz and 8 Hz. The stiffness at this point is nearly equal to the high frequency stiffness which corresponds to the excitation of the bellows alone. This is in good agreement with model and experimental results shown in the literature and with experimental tests carried out on an actual vehicle suspension in Chapter 3.

Influence of the pipe length. Fig. 2.9 shows the differential model (*model 3*) behaviour for decreasing pipe lengths. The pressure drop coefficient $\zeta + \lambda L/d$ is maintained constant whatever the length. Thus, only the factor A_p/L_p in Eq. (2.17) varies.
We can see that the differential model approaches the algebraic one (*model 4*) when the length decreases as the resonance effect becomes negligible. Let us also mention that the *model 3* simulation time increases as the length decreases, since the associated equation naturally becomes stiffer.

Influence of the chamber heat transfer. We consider in this case that the flow in the pipe is adiabatic. The heat flow is assumed proportional to the

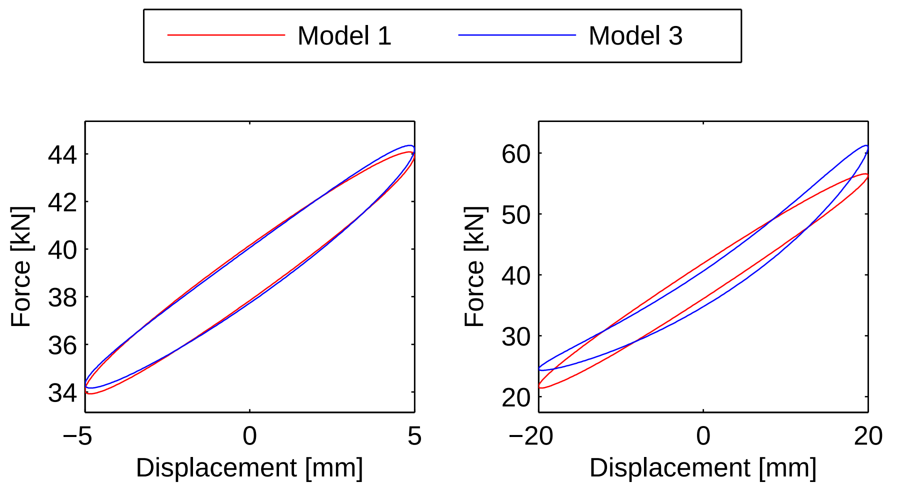

Figure 2.8: Force-displacement diagram for a 14 Hz excitation. Left: 5 mm excitation. Right: 20 mm excitation.

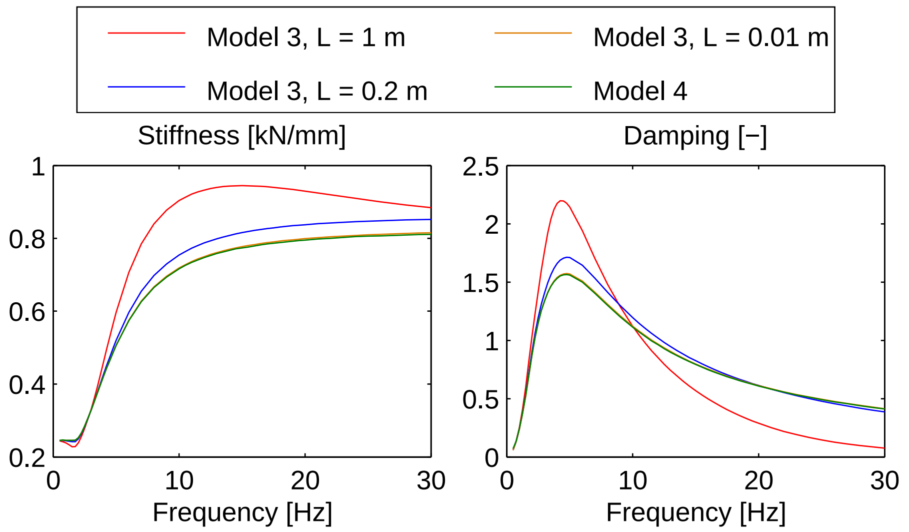

Figure 2.9: Influence of the pipe length on the dynamic stiffness K_{dyn} and the damping coefficient D_z for *model 3* (excitation amplitude equals 10 mm).

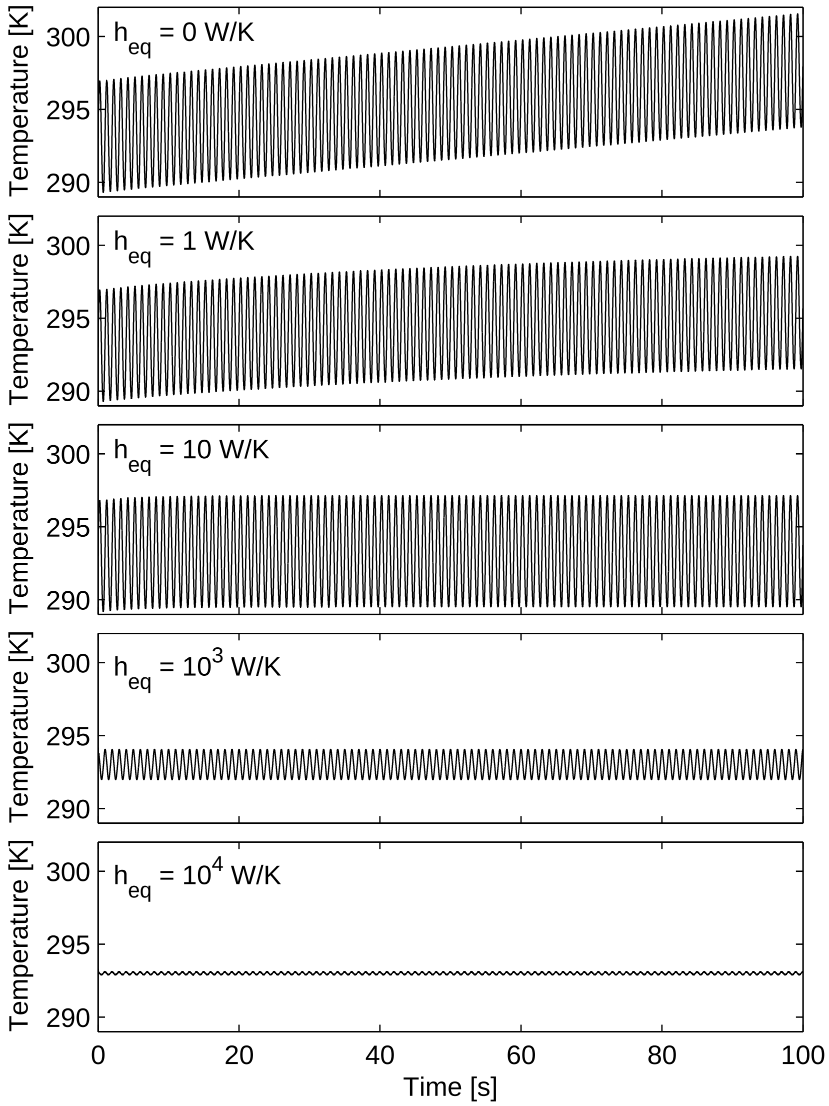

Figure 2.10: Influence of the chamber heat transfer coefficient on the temperature time history at 1 Hz excitation.

temperature difference between the chamber and the atmosphere (Eq. (2.13)). The same transfer coefficient is chosen for the two chambers. Since the heat transfer within the framework of railway suspensions has never been studied deeply, we investigate a wide range of transfer coefficient values, a null value corresponding to adiabatic tranformations while a very large value is close to the isothermal case.
Fig. 2.10 illustrates the temperature time history obtained for a 10 mm amplitude excitation at 1 Hz for several heat transfer coefficient values.
For a null value of the heat transfer coefficient h_{eq}, i.e. the adiabatic case, the temperature increases and does not stabilize since all the dissipated mechanical energy stays in the system. For $h_{eq} = 1\ W/K$, the mean temperature first increases and then stabilizes after several excitation cycles. For $h_{eq} = 10\ W/K$, the mean temperature is almost constant and the oscillation amplitude is similar to the cases $h_{eq} = 0\ W/K$ and $h_{eq} = 1\ W/K$. For $h_{eq} = 10^3\ W/K$, the oscillation amplitude decreases and the case $h_{eq} = 10^4\ W/K$ can be considered as isothermal due to the small temperature variations.
For higher frequencies, the oscillation amplitude begins to decrease for greater h_{eq} values. Furthermore, the mean temperature after stabilization is larger and is reached after a longer time since there is more energy injected in the system per second. For instance, for a 15 Hz excitation, the temperature reaches more than 6000 K for $h_{eq} = 1\ W/K$ which is of course not realistic!

Fig. 2.11 shows the dynamic stiffness after the mean temperature has stabilized for various frequencies and various heat transfer coefficients. The cases $h_{eq} = 0\ W/K$ and $h_{eq} = 1\ W/K$ are not drawn because they induce a non realistic temperature increase and the pressure oscillation amplitude does not stabilize which makes it difficult to calculate the dynamic stiffness.
We can observe that, for $h_{eq} \leq 100\ W/K$, the dynamic stiffness at the two constant levels reaches the adiabatic quasi-static stiffness. For $h_{eq} = 1\ kW/K$, the dynamic stiffness is close to the isothermal quasi-static stiffness for low frequencies and tends to the adiabatic level for high frequencies. For $h_{eq} = 10\ kW/K$, the behaviour is similar but the curve does not reach the adiabatic level for high frequencies in the considered frequency range.
The resonance effect is more important for small values of the heat transfer coefficient because the temperature elevation is more important and tends to increase the mean pressure and stiffness.

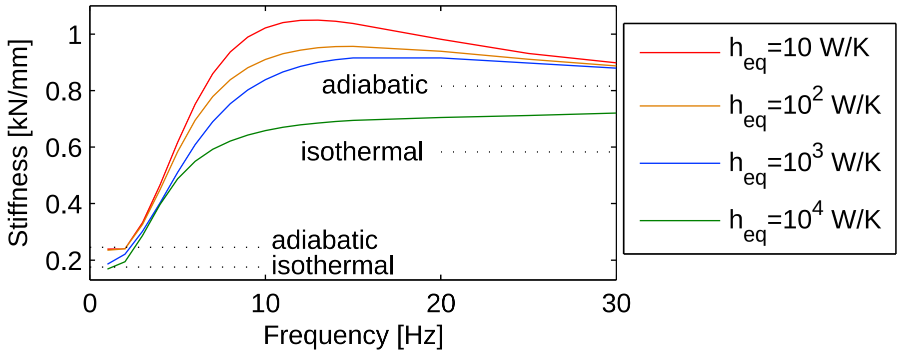

Figure 2.11: Influence of the chamber heat transfer coefficient on the dynamic stiffness. Dotted lines indicate the values of adiabatic and isothermal quasi-static stiffness for low and high frequencies (see Table 2.2).

Conclusion. The choice of a pneumatic suspension model will depend on the envisaged application and analysis: a model based on a differential equation for the pipe (*models 1, 2* or *3*) will be needed when the pipe is long while models with an algebraic equation (*model 4* or *5*) will be more suitable when there is no pipe or a short pipe between bellows and tank.
Contrary to *models 1* and *2*, *models 3* or *4* (as well as *model 5*) have the advantage of being easily coupled with the valve models presented in the following sections.

2.5.2 Compressible flow model

Fanno-based modelling approaches

Fanno line model. Contrary to the above approaches, the Fanno line model takes compressible effects in the pipe into account assuming a one-dimensional adiabatic steady flow. As depicted in Fig. 2.12, the duct is connected to an upstream tank maintained at a constant pressure p_0. On the other extremity, the pipe exhausts to a second tank maintained at a constant pressure $p_2 < p_0$. From point 1 to point 2, the pipe section area is constant and the flow is assumed adiabatic but friction is not neglected. Therefore we can deduce the

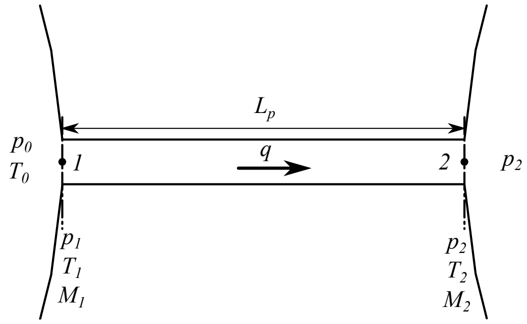

Figure 2.12: Illustration of the Fanno model.

following equations (see Refs. [7] and [44] for more details):

$$\frac{4C_f L_p}{d_p} = f(M_1) - f(M_2) \ , \tag{2.20}$$

where M is the Mach number, $f(M)$ is given by:

$$f(M) = \frac{1}{\gamma}\left(\frac{1-M^2}{M^2} + \frac{\gamma+1}{2} log\left(\frac{\frac{\gamma+1}{2}M^2}{1+\frac{\gamma-1}{2}M^2}\right)\right) \ , \tag{2.21}$$

and C_f is the friction coefficient which is related to the pressure drop coefficient λ by:

$$C_f = \lambda/4 \ . \tag{2.22}$$

The pressures at point 1 and point 2 are related by:

$$\frac{p_2}{p_1} = \frac{M_1}{M_2}\left(\frac{1+\frac{\gamma-1}{2}M_1^2}{1+\frac{\gamma-1}{2}M_2^2}\right)^{\frac{1}{2}} \ . \tag{2.23}$$

In order to determine the entry Mach number M_1, an isentropic transformation is assumed between the rest condition and the entry condition. Therefore, the pressure, the temperature and the Mach number at the nozzle end (point 1) obey the following relations:

$$\frac{T_0}{T_1} = 1 + \frac{\gamma-1}{2}M_1^2 \ , \tag{2.24}$$

$$\frac{p_0}{p_1} = \left(\frac{T_0}{T_1}\right)^{\frac{\gamma}{\gamma-1}} = \left(1+\frac{\gamma-1}{2}M_1^2\right)^{\frac{\gamma}{\gamma-1}} \ . \tag{2.25}$$

Finally, the mass flow rate in the pipe is then calculated by:

$$q_{Fanno} = A_p p_2 M_2 \sqrt{\frac{\gamma}{RT_2}} \; . \tag{2.26}$$

This approach therefore requires an iterative procedure to estimate the flow that establishes for given upstream and downstream pressures. The computational time is thus more important than for the incompressible flow method.

Fanno line differential model. Since the Fanno line model is based on a steady state solution, using it in our applications assumes that the flow establishes instantaneously for given pressure conditions. However the incompressible model comparison has shown that the pipe dynamics may not be negligible due to the air mass inertia. We therefore propose to establish, in an heuristic manner, a differential equation for the mass flow rate so as to take the inertia effect into account. Using the analogy between the incompressible differential (Eq. (2.16)) and incompressible algebraic (Eq. (2.17)) models which are related by Eq. (2.18), we obtain:

$$\dot{q}_{FannoDif} = \alpha \left(q^2_{Fanno} sign(p_0 - p_2) - q^2_{FannoDif} sign(q_{FannoDif}) \right) \; , \tag{2.27}$$

where: q_{Fanno} denotes the flow obtained by Eq. (2.26);
α is a delay parameter $[kg^{-1}]$.

The delay parameter α can be calculated using the analogy between Eqs. (2.18) and (2.27) which gives:

$$\alpha = \frac{\lambda L_p/d_p + \zeta}{2\rho A_p L_p}. \tag{2.28}$$

The fluid density ρ of course varies along the pipe in a compressible flow and does not remain constant over time. A unique value could be calculated by taking the mean value between the density at the two pipe ends for a given time. However, in the present case, we will see that considering a constant value equal to the initial pressure is satisfactory.

Bellows-tank subsystem benchmark

The bellows-tank subsystem benchmark is now used to compare the Fanno line model with the incompressible model presented in previous section. The following equations are used:

Pipe diameter	d_p	18 mm
Pipe wall rugosity	ϵ	0.15 mm
Friction coefficient	λ	0.03567
Delay parameter of Eq. (2.27)	α	1232 kg^{-1}

Table 2.5: Pipe specific parameters for the model comparison.

	Algebraic	Differential
Incompressible	Eq. (2.17)	Eq. (2.16)
Fanno	Eq. (2.26)	Eq. (2.27)

The cushion is submitted to a crushing-stretching sinusoidal excitation with a 20 mm semi-amplitude. The model parameters are the same as used in previous sections (see Table 2.1). Pipe specific parameters are listed in Table 2.5. The friction coefficient λ is assumed constant and is calculated with the Colebrook formula for fully turbulent flow and assuming hydraulically rough regime:

$$\frac{1}{\sqrt{\lambda}} = -2.0 \; log_{10} \frac{\epsilon/d_p}{3.7} \; . \tag{2.29}$$

For the incompressible model, a lumped loss coefficient $\zeta = 1$ must be added to take the exiting flow losses into account.

Model validation using a FLUENT reference solution

So as to obtain a reference solution, the bellows-tank subsystem has been implemented and simulated with the FLUENT software. This model would of course be too complex and time-consuming to be integrated in a model of the complete vehicle and it only serves to compare Fanno-based and incompressible approaches.

The solution is based on an axisymetric approach considering both the bellows and the tank as cylinders aligned with the pipe axis. The parameters are identical to those given in Tables 2.1 and 2.5 and the geometry is illustrated in Fig. 2.13. In this figure, the tank is on the left and the air spring is on the right. The dynamic mesh by layering technique has been used. More precisely, the bellows displacement is modelled with the in-cylinder model (that is designed for reciprocating engine modelling). The mesh is based on rectangular cells in the pipe and on triangular cells in the tank and the bellows. However, the cells adjacent to the moving boundary of the bellows are rectangular. Contrary to

(a)

(b)

(c)

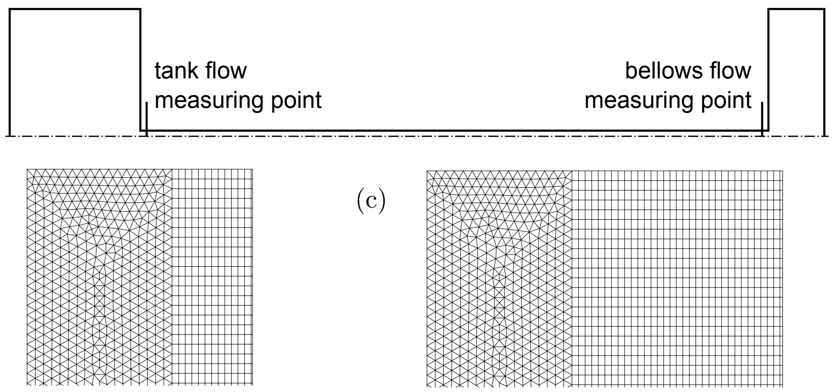

Figure 2.13: Illustration of the FLUENT model mesh. (a) Geometry of the system with the tank on the left and the bellows on the right. (b) Partial representation of the bellows mesh for maximal crushing. (c) Partial representation of the bellows mesh for maximal stretching.

what one may infer from Fig. 2.13 where the mesh for the bellows is shown, the mesh in the pipe was fine enough so as to capture the turbulent velocity profile and thus the losses.

The flow is modelled using the standard $k - \epsilon$ closure for the turbulence. The standard wall modelling approach has been selected as it provides correct predictions for flows inside pipes. The standard energy equation has been used including the viscous heating term in order to take the increase in average temperature observed in other models into account. The air inside the system has been considered as an ideal gas with constant properties.

The flow has been initialized with null velocity and the initial pressure. The equations have been solved using an explicit first order scheme in time and a second order scheme in space. The pressure has been recorded on the bellows and tank walls to compare them with the other models predictions. The mass flow rate in the pipe has been measured on both pipe ends (exactly at 10 mm from the pipe connections with the tank and the bellows, see Fig. 2.13(a)). Since fluid can be accumulated in the pipe due to its compressibility, the two mass flow rate may not be necessarily equal.

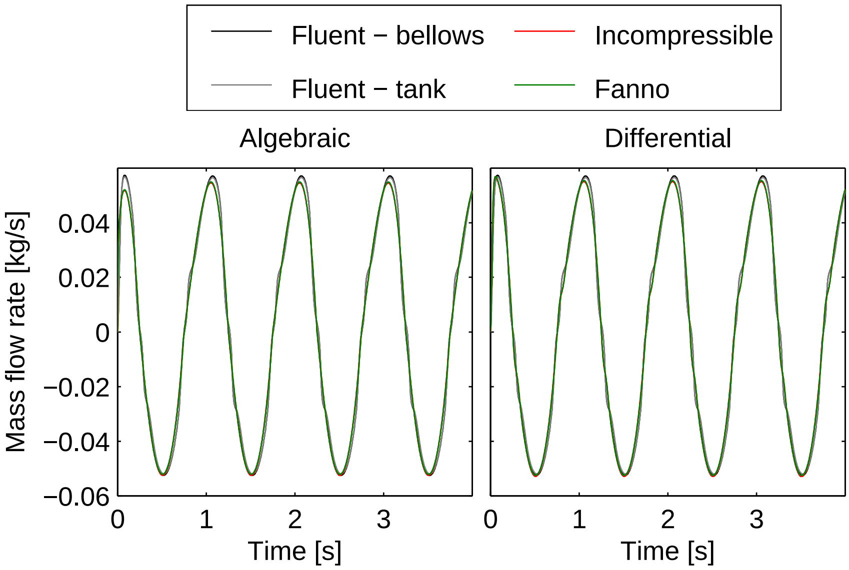

Figure 2.14: Mass flow rate for a 1 Hz excitation. Left: algebraic models compared with the FLUENT results. Right: differential models compared with the FLUENT results.

Comparison for various frequencies. For low frequencies, the four models agree well with the FLUENT curves as illustrated in Fig. 2.14. For FLUENT results, both the mass flow rate entering the tank and exiting the bellows are plotted but they are too close from each other to be distinguished. As the excitation is quite slow, the pressure in the tank "follows" the bellows pressure and therefore the pressure ratio is close to unity (about 0.96). The fluid velocity in the pipe is small and the compressible effects are negligible. The Mach number in the pipe does not exceed 0.13, value for which the incompressible hypothesis is satisfactory. This clearly appears in Fig. 2.15 that shows the impact of the pressure ratio on the steady state mass flow rate and the Mach number.

For higher frequencies, it is shown in Fig. 2.16 that the mass flow curves of the algebraic models precede the FLUENT curve because they do not take the inertia of the fluid into account. We observe that models with a differential equation for the pipe correctly capture this phase effect. The incompressible models present a larger oscillation amplitude than the reference results. Effec-

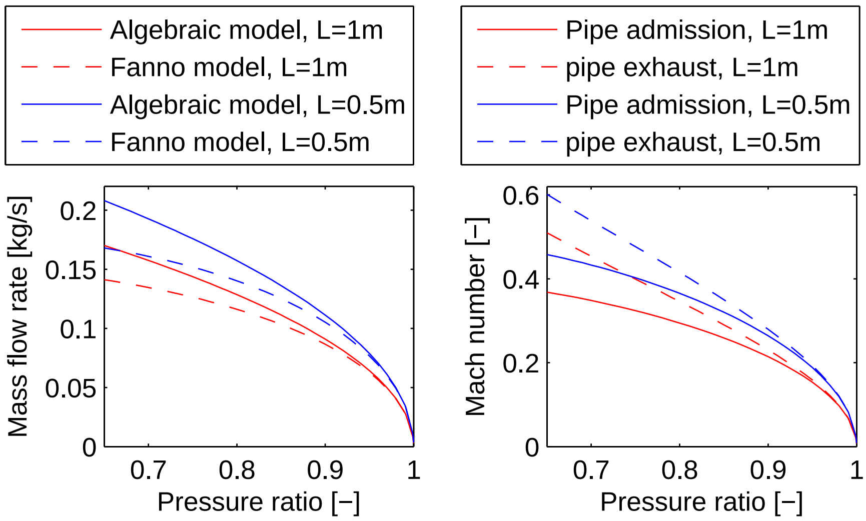

Figure 2.15: Left: influence of the pressure ratio on the steady state mass flow rate with the two models and for two different pipe lengths. Right: influence of the pressure ratio on the Mach number calculated with the Fanno model for two different pipe lengths.

tively, the tank pressure does not oscillate as much as the bellows pressure, the pressure ratio is thus lower (about 0.73), which induces larger fluid velocities in the pipe. The Mach number at the pipe end is about 0.41 and compressible effects are no longer negligible. Those effects induce a mass flow limitation which is not captured by incompressible models. The Fanno differential model is the closest curve to the FLUENT results but still has an amplitude error. In this case, we can distinguish the two mass flow rate curves calculated by the FLUENT model: one corresponds to the flow exhausting the bellows, the other to the flow entering the auxiliary tank.

The influence on the pressure curves is more important for the tank than for the bellows because the bellows pressure variation is more guided by the volume variation than by the mass variation while the pressure fluctuations in the tank only depend on the mass flow rate in the pipe.

The bellows reaction force is therefore well approximated by the four models. The pipe model has more impact on the mass flow rate calculation, which could be of importance if an orifice or a valve was placed on the duct.

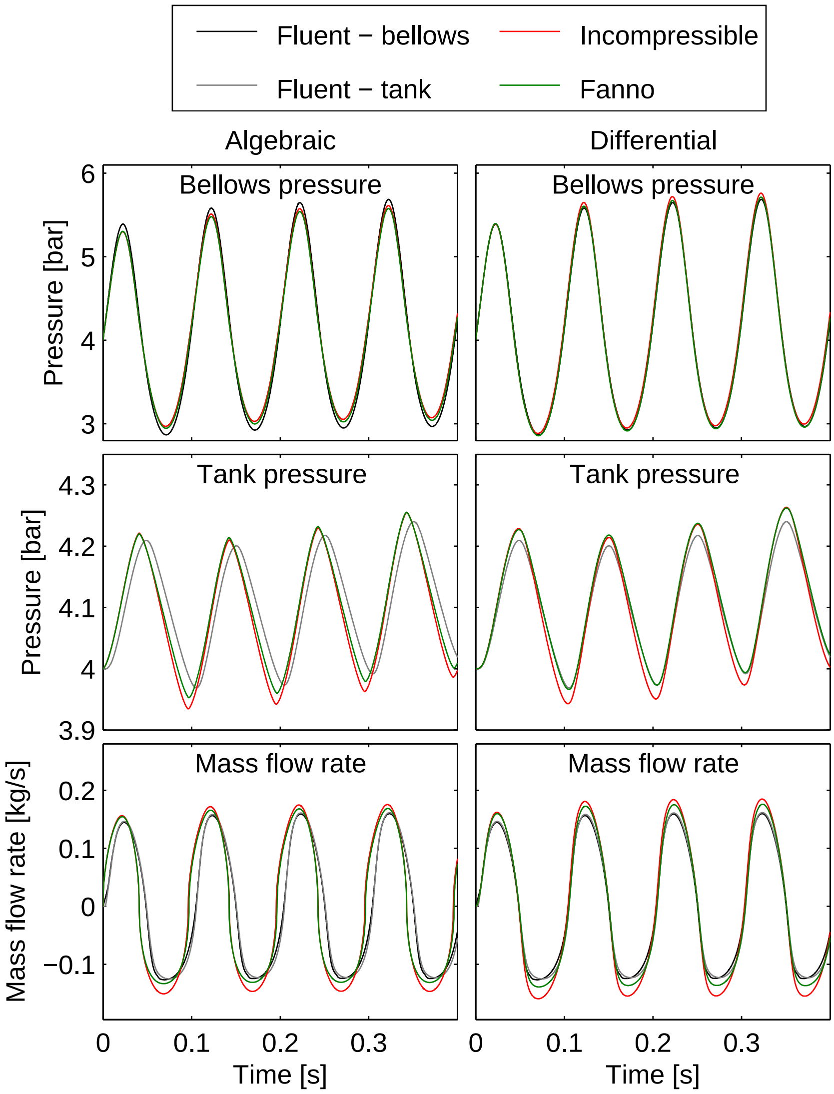

Figure 2.16: Pressure and mass flow rate for a 10 Hz excitation. Left: algebraic models compared with the FLUENT results. Right: differential models compared with the FLUENT results.

Influence of the pipe length. When reducing the pipe length, friction decreases and thus the fluid velocity is higher. The Mach number is about 0.48 at the pipe end even though the pressure ratio does not change compared with the case with a 1 m long pipe. Therefore compressible effects become more important as depicted in Fig. 2.15. As illustrated in Fig. 2.17, the amplitude errors for incompressible models are larger.
The effects on the bellows pressure are more visible but they are still more significant for the tank pressure.

Dynamic stiffness comparison. Fig. 2.18 shows the dynamic stiffness calculated for the four analysed models. A heat transfer coefficient $h_{eq} = 10\ W/K$ is used for both the cushion and the tank. It appears that the impact of compressible effects taken into account by the Fanno model is quite limited. For high frequencies, the dynamic stiffness is a bit lower for the Fanno differential model because the flow saturates earlier due to the compressibility effects.

Conclusion. The present analysis has highlighted that:

- for increasing excitation frequency, a phase difference on the mass flow rate time history appears for models which use an algebraic equation,
- incompressible models overestimate the fluctuation amplitude of the mass flow rate
- compressible effects become significant when the frequency increases, especially for shorter pipes,
- the effects are not so important on the bellows pressure, which mainly depends on the volume variation imposed by the excitation, and thus the impact on the reaction force is limited,
- the mass flow rate and the tank pressure are more influenced by the chosen model.

2.5.3 Discretization method approach

In order to refine the pneumatic modelling and to analyse the impact of the fluid compressibility and pressure waves which are not captured by the Fanno

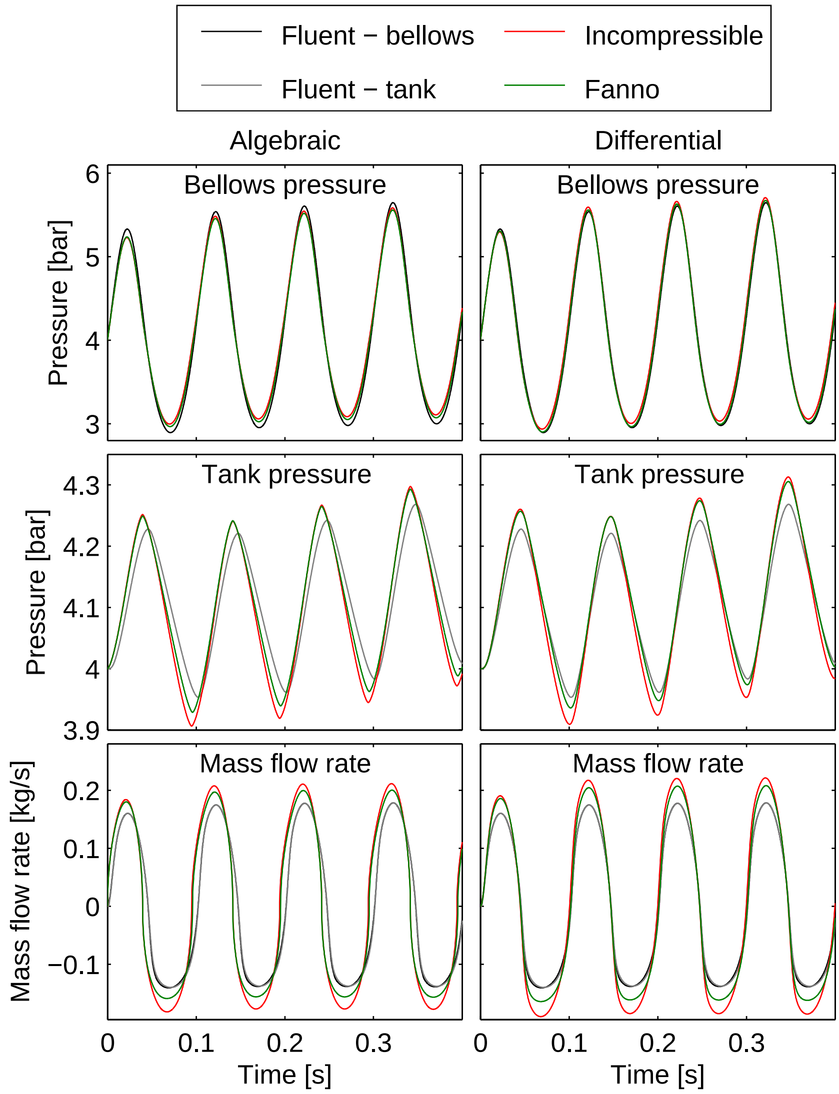

Figure 2.17: Pressure and mass flow rate for a 10 Hz excitation with a 0.5 m pipe. Left: algebraic models compared with the FLUENT results. Right: differential models compared with the FLUENT results.

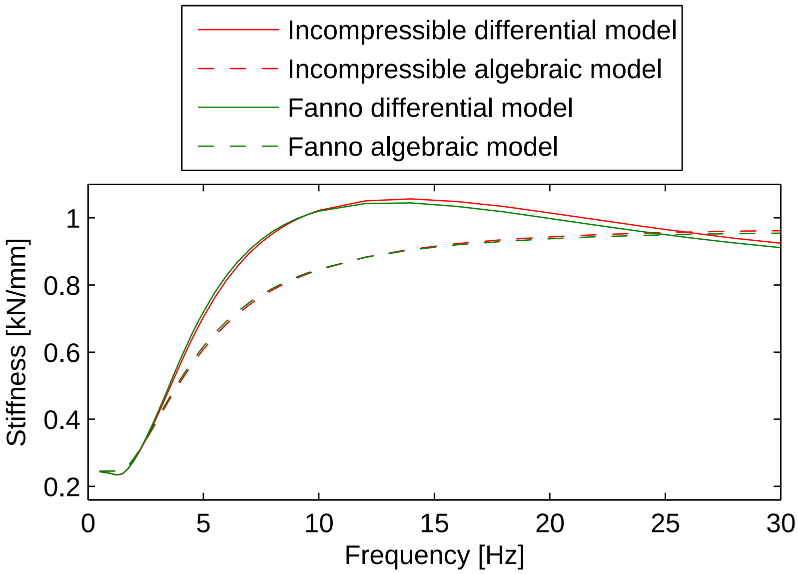

Figure 2.18: Comparison of incompressible and Fanno models: dynamic stiffness of a the bellows-tank subsystem calculated for a 10 mm excitation amplitude and a 1 m long pipe.

line model, a discretized method for the pipe model is implemented and tested on the bellows-tank subsystem.

Discretized method. This approach is based on the work of Seynhaeve et al. (Ref. [64]). The flow in the pipe is assumed one-dimensional and adiabatic. Since the duct section is constant, the flow obeys the following equations:

$$\frac{\partial u}{\partial t} + \frac{\partial F(u)}{\partial x} = B(u); \tag{2.30}$$

where the vector of variables is defined as:

$$u = \begin{pmatrix} \rho \\ \rho w \\ \rho e \end{pmatrix}; \tag{2.31}$$

with: x is the position coordinate along the pipe;
ρ the density;

w the average axial velocity;
$\rho e = \rho\,(u + w/2)$ the energy density.

The fluxes have the following form:

$$F(u) = \begin{pmatrix} \rho w \\ p + \rho w^2 \\ w(\rho e + p) \end{pmatrix}; \tag{2.32}$$

and the right hand side can be written as:

$$B(u) = \begin{pmatrix} 0 \\ -\frac{\partial p}{\partial x}\Big|_f \\ 0 \end{pmatrix}; \tag{2.33}$$

with p the pressure. According to Ref. [64], friction losses can be given by:

$$-\frac{\partial p}{\partial x} = \frac{\lambda \rho w^2}{2 d_p}; \tag{2.34}$$

with: d_p the pipe diameter;
λ the friction coefficient.

Those equations are solved using the Lax-Wendroff integration scheme. This scheme calculates the solution from the current time step n to the following time step $n+1$ using an intermediate evaluation $(n+1/2)$ of the fluxes as illustrated in Fig. 2.19 (more details can be found in Refs. [43, 64, 72]).

Concerning the boundary conditions, the entering and exiting flow conditions must be distinguished. For the entering flow, the fluid velocity is extrapolated from the pipe interior and the pressure and the temperature are imposed assuming an isentropic expansion from the stagnation condition in the pneumatic chamber to the pipe entrance. For the exiting flow, only the chamber pressure is imposed while the temperature and the velocity are extrapolated from the pipe interior. At each time step, the pressure and the temperature to impose to the flow are deduced from the ODEs of the pneumatic chambers (Eqs. (2.10) and (2.11)). The calculated velocities are used to impose the flow entering the bellows and the tank. The ODEs are integrated using a fourth order Runge-Kutta scheme with a time step equal to the Lax-Wenndroff scheme. Interaction variables are exchanged between the two schemes at the beginning of each time step.

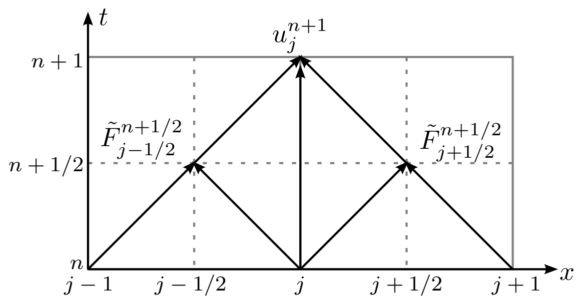

Figure 2.19: Illustration of the Lax-Wendroff integration scheme.

Comparison with Fanno and Fluent solutions. The mass flow rate exiting the bellows and entering the tank are plotted in Fig. 2.20. The difference between those two curves is very small for a 1 m long pipe. Furthermore, the results obtained with the discretized one-dimensional model are very close to the Fanno curves. For the 10 Hz excitation, the difference between the bellows and tank flow rate observed for the Fluent model are reproduced by the discretized one-dimensional method but the oscillation amplitude is larger.
This analysis tends to show that the Fanno differential model with delay is quite satisfactory for the present test case. However further conditions should be tested such the use of longer pipes for which the pressure waves may have more influence. As it will be shown in Chapter 3, the discretized model will be able to reveal resonance effects that are not captured by the two differential models.

2.6 Valves modelling

Pneumatic suspension circuits involve various kinds of valve, the three more important being the levelling valve, the safety valve and the pressure differential valve (see Fig. 1.8). As for the pipes, the valve models define a relation between the mass flow rate and the port pressures. Furthermore, in certain cases, additional inputs must be considered such as the lever position of the levelling valve.

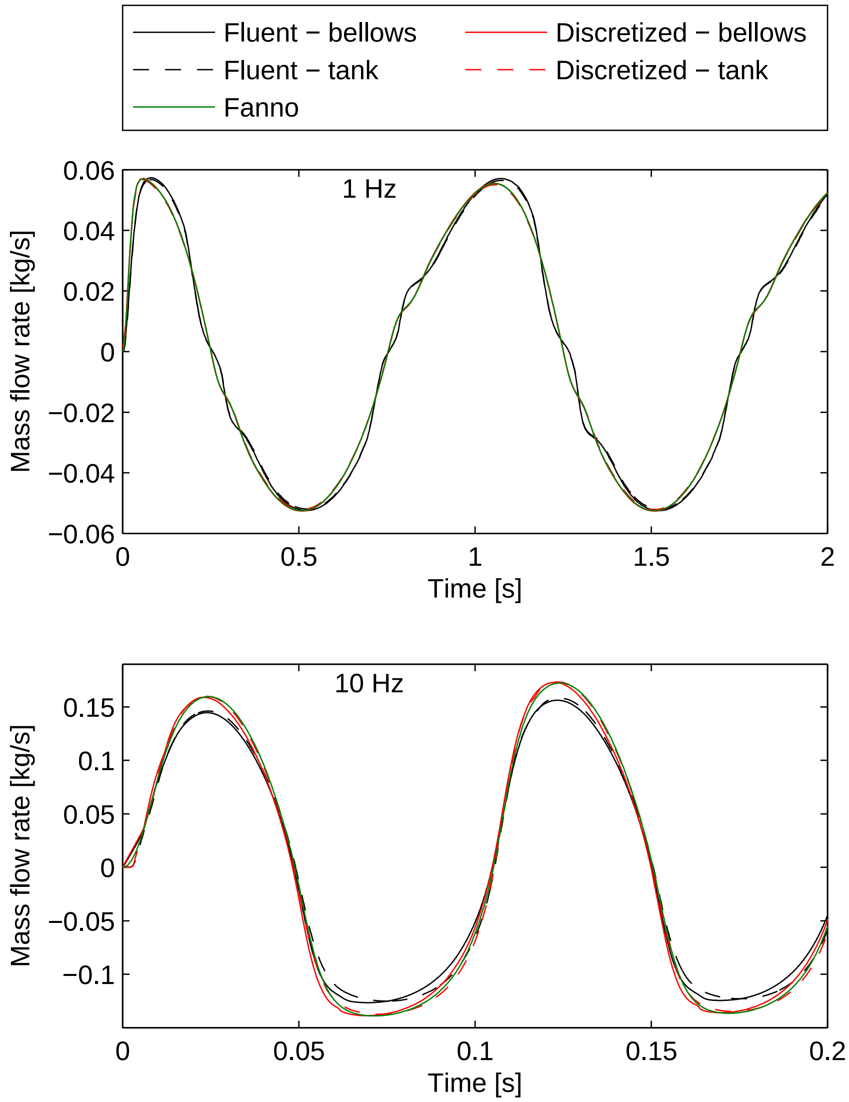

Figure 2.20: Comparison of the numerical solution of the one-dimensional unsteady flow model using the Lax-Wendroff integration scheme with the Fanno-based approach and the FLUENT reference solution.

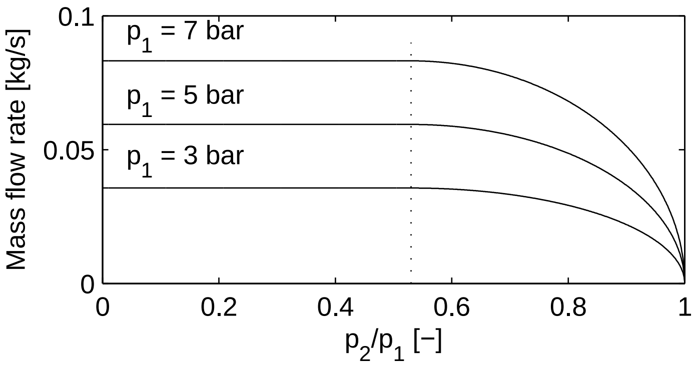

Figure 2.21: Mass flow rate calculated with the ISO 6358 standard for various upstream pressure with $T_{ref} = 293.15\ K$, $p_{ref} = 1\ bar$, $b = 0.53$ and $C = 1\ 10^-7\ sm^4/kg$. The corresponding effective diameter is thus 8 mm, according to Eq. 2.37.

Levelling valve. This valve controls the air quantity in the suspension by inflating or deflating the bellows when the carbody height is varying. It is a three-port valve: one port is connected to the pressure source, one to the atmosphere and one to the chamber. However, the flow establishes between two ports only at the same time. Consequently, the mass flow rate q must be calculated given the upstream and downstream pressures and the valve lever displacement. The ISO 6358 standard is used to calculate the dependence with pressure:

$$q = Cp_1\rho_{ref}\sqrt{\frac{T_{ref}}{T_1}} \quad \text{if} \quad \frac{p_2}{p_1} \leq b \tag{2.35}$$

$$q = Cp_1\rho_{ref}\sqrt{\frac{T_{ref}}{T_1}}\sqrt{1-\left(\frac{\frac{p_2}{p_1}-b}{1-b}\right)^2} \quad \text{if} \quad \frac{p_2}{p_1} \geq b \tag{2.36}$$

where: subscripts 1 refer to upstream conditions ($max(p_b, p_t)$);
subscripts 2 refer to downstream conditions ($min(p_b, p_t)$);
subscripts ref refer to reference conditions ($T_{ref} = 293.15\ K$ and $p_{ref} = 1\ bar$);
C is the sonic conductance [sm^4/kg];
b is the critical pressure ratio [$-$].

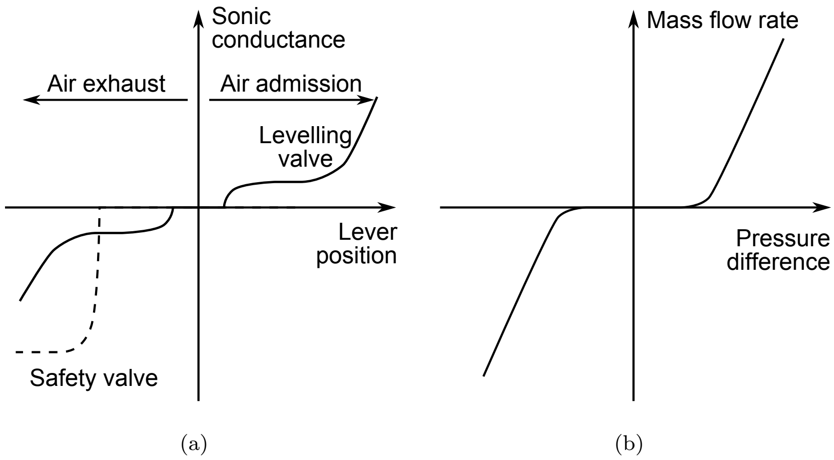

Figure 2.22: Qualitative valve characteristics. (a) Sonic conductance as a function of the lever displacement for levelling and safety valves. (b) Mass flow rate as a a function of pressure drop across a differential pressure valve.

This relation takes into account the sonic cutoff effect: for pressure ratio smaller than b, the mass flow rate does not depend on the downstream pressure (see Fig. 2.21). According to the standard, the sonic conductance is related to the valve effective area by the following equation:

$$A = C\rho_{ref}\sqrt{sRT_{ref}}, \tag{2.37}$$

where $s = \frac{1}{1-b}$ is the coefficient of compressibility effect.

The sonic conductance varies with the valve lever position and is given by a characteristic curve as illustrated in Fig. 2.22(a). This characteristic can be determined using experimental data for various lever position and for at least one constant upstream pressure.

Safety valve. The safety valve is modelled in the same way as the levelling valve. The main difference is that it works only in exhaust mode between the pneumatic chamber and the atmosphere (see Fig. 1.8). As it is illustrated in Fig. 2.22(a), the sonic conductance characteristic is very abrupt so as to generate an important mass flow as soon as the lever reaches the engaging value.

Differential pressure valve. This valve is used in the four-point configuration and transfers air between the two bellows or the two tanks of a same bogie when the pressure difference is too large (typically, the set point is between 1 *bar* and 2.25 *bar*). The mass flow rate is thus a function of the two port pressures only. A first approximation consists in taking it as a function of the pressure difference as illustrated in Fig. 2.22(b). An other solution would consist in taking the mass flow given by the ISO 6358 standard with a sonic conductance depending on the pressure difference.
The first solution has been used in the present work. Further investigations should refine this model and analyse its impact on the suspension dynamics.

2.7 Conclusion

In this chapter, we presented a thermodynamics oriented approach for the modelling of railway pneumatic suspension. This method was confronted to other solutions from the literature for a benchmark composed of an air spring submitted to sinusoidal displacement excitations and connected to an auxiliary tank via a 1 m long pipe. The developed models, which establishes a model for each component, is more flexible since it allows us to combine the various suspension elements in several ways. It is also more suitable to interpret the phenomena that occur in the system since the pressure, the mass flow rate, etc. are directly accessible.
We particularly concentrated on the modelling of pneumatic pipes, for which several approaches were compared. On one hand, algebraic and differential models where analysed. It was shown that inertia effects due to the air mass in the duct, captured only by the differential models, are not negligible, except in the case of very short pipes for which algebraic models are more time-efficient. On the other hand, incompressible flow equations were compared to a compressible flow approach based on the steady-state Fanno line model. The two methods were confronted to a reference solution calculated with the FLUENT software. It appears that compressible effects induce a mass flow rate limitation for high excitation frequencies. However, the impact on the suspension reaction force remains limited. A last solution based on a discretized method

for the pipe was also presented but, in the present case, it did not provide more accurate results than the Fanno line approach. Nevertheless, further conditions should be tested such as longer pipes as it will be shown in the next chapter.
We also showed that the heat transfer between the air in the system and the atmosphere may influence the suspension quasi-static and dynamic responses. However, the impact strongly depends on the heat transfer coefficient which is unknown for the tank and the bellows. It is therefore needed to perform experiments on a real suspension so as to establish the various parameters of the models. This analysis will thus be conducted in Chapter 3.

Chapter 3

Experimental illustration and validation

As we have shown in the previous chapter, many modelling approaches can be adopted to deal with pneumatic suspension circuits. Various hypotheses have been compared and it was shown that the choice among the various possibilities depends on the circuit configuration and on the working conditions such as the amplitude, the frequency, etc. Models based on an energy balance and mass flow formulation are certainly the most flexible since they rely on a component oriented modelling. Furthermore, the model parameters can be straightforwardly interpreted with regard to the physical system.
Concerning the model parameters, some of them, typically the effective are A_{e0}, its gradient dA_e/dz and the cushion volume V_{b0}, are provided by suspension manufacturers. Other parameters are often unknown.
The goal of this chapter is therefore to validate and to quantify the model presented in Chapter 2 by analysing a real suspension. After describing the experimental setup, we will first propose a method to evaluate the bellows model parameters. We will then analyse the heat transfer so as to establish whether it is important. Finally, we will confront experimental results with numerical simulations for the bellows-tank benchmark defined in Section 2.2.
The analyses presented in this chapter are the results of tests that we have performed at the *Laboratoire d'Essai Mécanique* (Laboratory of Mechanical Tests) of the *Université catholique de Louvain*.

3.1 Device description

The test bench is illustrated in Fig. 3.1. It is intended to reproduce the bellows-tank subsystem test case. We will first briefly describe its various components.

The pneumatic cushion

The air spring was provided by Bombardier Transportation France. It corresponds to the size of bellows used for a metro suspension. It is composed of three main parts: the steel upper plate that should be fixed to the bogie traverse, the rubber diaphragm and the base block that contains the emergency spring and a rubber bump stop (see Fig. 3.3). The main parameters are listed in Table 3.1.
Two holes were drilled in the upper plate: one for the pressure and temperature sensors and one for a flexible hose that connects the cushion to the other components (see Fig. 3.2). Therefore, the air spring lies upside down so that all the connections stay at rest.

The auxiliary tank

A compressor reservoir was used as auxiliary tank. Its volume was measured simply by filling it with water and comparing the empty and the filled weight. On one side, the tank was joined to the pressure source via a manual valve and a pressure regulator. On the other, a flexible hose was connected as for the bellows.

The connecting line

In addition to the flexible hoses fixed to the cushion and to the reservoir, an additional duct was used to highlight the dynamic effects revealed in Chapter 2. As shown in Figs. 3.1 and 3.2, it is composed of four long straight 1/2 *inch* galvanized pipes and three shorter ones. Those elements are connected with seven 90° elbows. Quick couplings are placed at the two ends as for the flexible hoses. The air spring can thus be connected to the long pipe or directly to the auxiliary tank. Furthermore, it is also possible to add a pipe restriction in the circuit or to directly feed the bellows with the pressure source so as to test it alone.

Figure 3.1: Test bench illustration. The bent in orange supports the hydraulic cylinder which acts on the cushion. The latter is connected to an auxiliary tank via a 1/2 *inch* galvanized pipe.

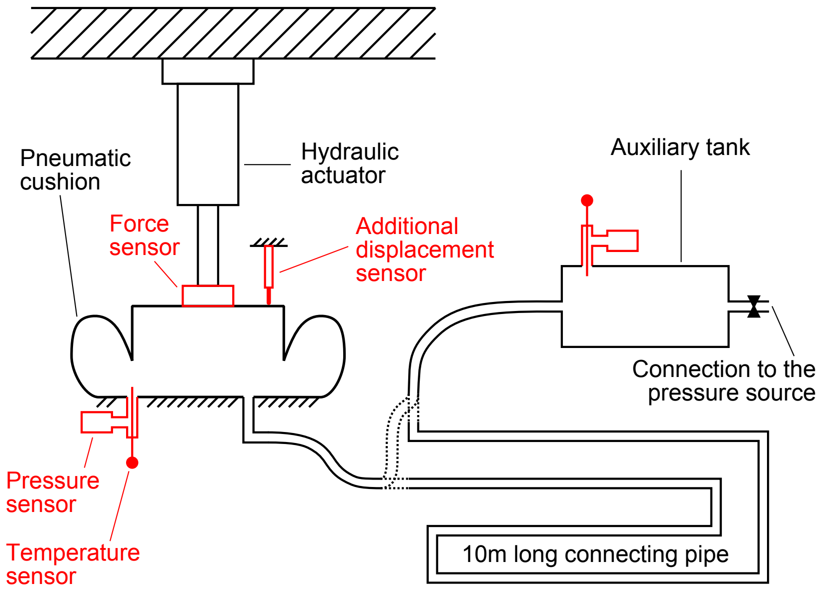

Figure 3.2: Test bench diagram.

Figure 3.3: Illustration of the analysed cushion and its various parts. Top: upside down air spring. Bottom, from left to right: upper plate, rubber diaphragm and emergency spring.

Hydraulic actuator

The cushion was moved via a 10 *tons* hydraulic cylinder fixed to a portal frame. The actuator could be force or displacement controlled with enough accuracy for the performed experiments.

Measuring devices

- The force was measured by a sensor placed between the hydraulic actuator and the air spring.
- The displacements were measured with the LVDT[1] sensor of the hydraulic cylinder. For dynamic tests, an additional LVDT sensor was placed directly between the ground and the moving part of the air spring.

[1] LVDT stands for Linear Variable Differential Transformer

Pneumatic bellows	
Upper plate diameter	500 mm
Stroke	40 mm
Nominal distance from the emergency spring	20 mm
Nominal height	200 mm
Auxiliary tank	
Volume	23.2 dm^3
Length	550 mm
Diameter	240 mm
Flexible hoses	
Internal diameter	13.8 mm
bellows hose length	0.75 m
Tank hose length	0.6 m
Galvanized connecting pipe	
Internal diameter	15.5 mm
Total length	8.9 m

Table 3.1: Main parameters of the bellows-tank experimental setup.

- Two pressure transmitters from Kistler (Type RAG25R10BC1H) were used to measure the relative pressure in the cushion and in the auxiliary tank. Their measuring range was $0 - 10$ bar.

- Two thermocouples were connected to the air spring and to the tank. Due to the thermal inertia of these sensors, we only measured the mean temperature variation during dynamic tests. The tank thermocouple was placed around 40 mm from the cylindrical wall. For the bellows, the thermocouple was placed at almost 10 mm from the upper plate so as to avoid contact with the rubber diaphragm or the emergency spring.

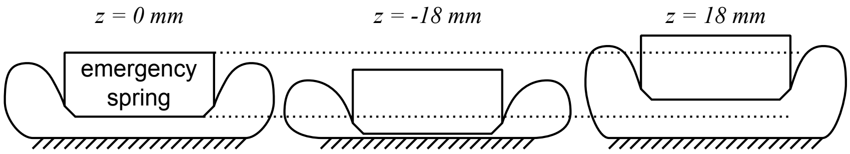

Figure 3.4: Illustration of the bellows displacement z.

3.2 Quasi-static experiments

Two kinds of quasi-static tests were performed so as to determine the parameters of the bellows and auxiliary tank models. Furthermore, the various measurements were also performed when deflating the suspension, which constitutes a third "test". In this section, we describe the performed experiments and then explain how the results are processed to identify the model parameters.

3.2.1 Test description

Isothermal test

The goal of this experiment was to determine the "geometrical" parameters of the suspension presented in Section 2.1:

- the bellows volume V_{b0} (Eq. (2.1)),
- the volume gradient dV_b/dz (Eq. (2.1)),
- the effective area Ae_0 (Eq. (2.3)),
- the effective area gradient dA_e/dz (Eq. (2.3)).

The air spring was submitted to a very slow slope displacement excitation such that transformations can be considered isothermal. The cylinder displacement z is plotted in Fig. 3.5. The position $z = 0$ mm corresponds to the nominal position of the suspension, $z = -18$ mm to the maximal crushing and $z = 18$ mm to the maximal stretching (see Fig. 3.4). For the value $z = -20$ mm, the emergency spring is in contact with the upper plate, which corresponds to the air spring configuration when it is deflated. The test was performed for the cushion alone and for the complete system (see Table 3.2).

	Assembly	Initial pressure
Isothermal A	Bellows - tank - 10m pipe	3 bar_{rel}
Isothermal B	Bellows - tank - 10m pipe	5 bar_{rel}
Isothermal C	Bellows	3 bar_{rel}
Isothermal D	Bellows	5 bar_{rel}
Isothermal E	Bellows - tank	3 bar_{rel}
Isothermal F	Bellows - tank	5 bar_{rel}

Table 3.2: Test conditions for the isothermal test.

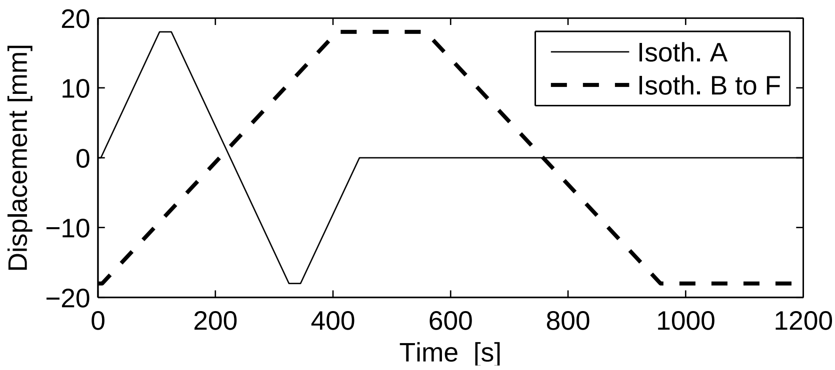

Figure 3.5: Displacement excitation for the isothermal test.

Test ID	Initial pressure	Time to reach $0.5\ bar_{rel}$
Defl. B	$5\ bar_{rel}$	$10\ s$
Defl. D	$5\ bar_{rel}$	$460\ s$
Defl. E	$3\ bar_{rel}$	$6\ s$
Defl. F	$5\ bar_{rel}$	$140\ s$
Defl. G	$3\ bar_{rel}$	$25\ s$
Defl. H	$3\ bar_{rel}$	$7\ s$

Table 3.3: Test conditions for the deflating test.

Deflating test

At the end of a test, the airspring was deflated by connecting the pneumatic circuit to the atmosphere. The force and the pressure were recorded while the displacement was maintained constant by the hydraulic cylinder. Various deflating speeds were tested by opening more or less the valve that connects the system to the atmosphere. This information was used to analyse the force-pressure curve as we will see in Section 3.2.2. The various records are listed in Table 3.3.

Step test

The bellows was submitted to a displacement step excitation as illustrated in Fig. 3.6 (in practice, it is a very short slope excitation, i.e. between 1 s and 2 s). The excitation was maintained until the cushion and tank pressures stabilized. As for the isothermal test, the experiment was performed with the bellows only and with the bellows-tank system, and for various initial pressures (see Table 3.4).

The goal of this test was to analyse how the pressures and temperatures vary after the excitation is applied due to the heat transfer between the chambers and the atmosphere.

Test ID	Assembly	Initial pressure
Step A	Bellows - tank - 10m pipe	3 bar_{rel}
Step B	Bellows - tank - 10m pipe	5 bar_{rel}
Step C	Bellows	3 bar_{rel}
Step D	Bellows	5 bar_{rel}
Step E	Bellows - tank	3 bar_{rel}
Step F	Bellows - tank	5 bar_{rel}

Table 3.4: Test conditions for the step test.

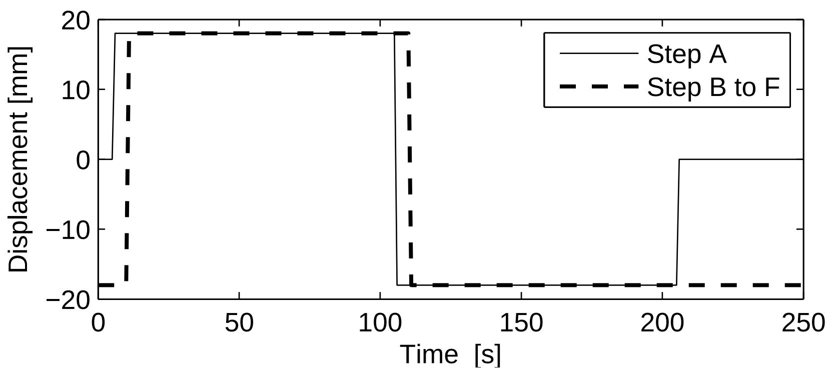

Figure 3.6: Displacement excitation for the step test.

3.2.2 Test analysis and parameter assessment

Volume and volume gradient

For each isothermal test, the temperature is assumed to be constant during all the test (observed temperature variations are less than $2°C$). Furthermore, it is assumed that the total air mass in the bellows and in the tank remains constant. For the 3 *bar* tests, a small pressure loss is observed but does not affect too much the results. For 5 *bar* tests, the pressure drop is a bit more important and makes the results less reliable. Since the deformation is very slow (see Fig. 3.5), the pressure at a given time can be considered uniform in all the system. Therefore, considering the perfect gas equation, we have for any displacement:

$$pV = MRT = p_0 V_0 \tag{3.1}$$

where p is the absolute pressure in the system $[Pa]$;
V is the total air volume $[m^3]$;
M is the total air mass $[kg]$;
T is the temperature in the system $[K]$;
R is the specific gas constant $[287.1\ J/kg/K]$;
subscript 0 refers to the initial conditions.

If only the air spring is used, it becomes, under isothermal conditions:

$$V_b p_b = p_0 V_{b0}, \tag{3.2}$$

where subscript b refers to the bellows properties.
If the bellows and the additional tank are used, we have:

$$(V_b + V_t) p_{b+t} = p_0 \left(V_{b0} + V_t\right), \tag{3.3}$$

where subscript t refers to the tank properties and p_{b+t} stands for the pressure in all the system.

Considering Eqs. (3.2) and (3.3) for corresponding bellows volumes leads to the following system of equations:

$$\left\{ \begin{array}{c} V_b - \frac{p_0}{p_b} V_{b0} = 0 \\ V_b - \frac{p_0}{p_{b+t}} V_{b0} = \left(\frac{p_0}{p_{b+t}} - 1\right) V_t \end{array} \right. \tag{3.4}$$

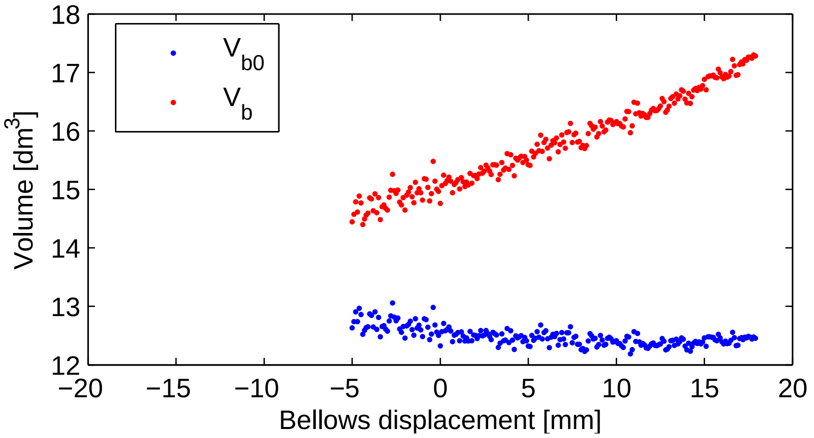

Figure 3.7: Initial volume and volume calculated for a given bellows displacement, computed from the expansion phase measurements of the *isothermal C* and *isothermal E* tests. Values for $z < -5$ mm are not shown because the pressure variation is not sufficient to obtain consistent results.

In this system, the bellows volume at a given time V_b and the initial bellows volume V_{b0} are the unknowns. We must therefore measure the pressure for equal bellows volume in the case of the bellows alone and in the case of the bellows connected to the tank. According to the literature, the bellows volume can be considered independent of the bellows pressure. This hypothesis has not been explicitly checked in this experiments but experimental results are in good agreement with it. Thus, considering 0 conditions for $z = z_0 = -18$ mm, the system 3.4 can be used to calculate V_{b0} and V_b for each bellows crushing value. Fig. 3.7 shows the evolution of V_{b0} and V_b during the expansion phase. We can see that V_{b0} remains essentially constant as expected and that the variation of V_b is almost linear. Therefore, Eq.(2.1) for the bellows volume can be used:

$$V_b = V_{b0} + \frac{dV}{dz} z \tag{2.1}$$

The volume V_b and the volume gradient $\frac{dV}{dz}$ can be estimated in three ways:

- by taking the mean value of V_{b0} in Fig. 3.7 and by taking the mean slope of the V_b curve (imposing $V_b = V_{b0}$ for $z = -18$ mm),
- by doing the same with the compression phase data,

- by taking the pressure mean values during the constant displacement period ($z = 18\ mm$ between 400 and 550 s in Fig. 3.8) and applying the equation system (3.4) only once.

The results appear in the following table:

	$V_{b,z=-18mm}$	dV/dz	$V_{b,z=0mm}$
Mean values of expansion phase	12.7 dm^3	0.142 m^2	15.2 dm^3
Mean values of compression phase	12.5 dm^3	0.137 m^2	15.0 dm^3
Mean values of stabilized phase	12.4 dm^3	0.135 m^2	14.9 dm^3

It clearly emerges that the three calculation methods lead to different results. This can be explained by two factors. First, the influence of temperature variation is not negligible as it can be guessed by examining to Figs. 3.8(a) and 3.8(b) that show a small asymptotic pressure variation after the slope excitation is finished. The second reason is certainly the small pressure loss that is also observed in Fig. 3.8(b).
For the following section, the volume and volume gradient obtained with the mean pressure of the stabilized phase will be considered. Note that this volume includes the volume of the flexible hose which connects the cushion to the tank or to the pressure source.

Effective area

By definition, the effective area is the ratio between the force and the bellows relative pressure (see Section 2.1):

$$A_e = \frac{F}{p - p_a}. \tag{3.5}$$

Deflating measurements illustrated in Figs. 3.9 show that the force varies linearly with the relative pressure, at least for pressure superior to 1 bar_{rel} (Fig. 3.10). It means that the effective area is independent of the pressure. However, the force is null before the pressure reaches 0 bar_{rel}. This is partly due to the mass of the air spring base. The correction to be applied is calculated via a linear regression that gives values between 975 N and 1070 N. Taking that into account, Fig. 3.10 confirms that the effective area is independent of pressure.

Since the effective area is independent of the pressure, we can use the isothermal test to study how it varies when the bellows is crushed. Fig. 3.11

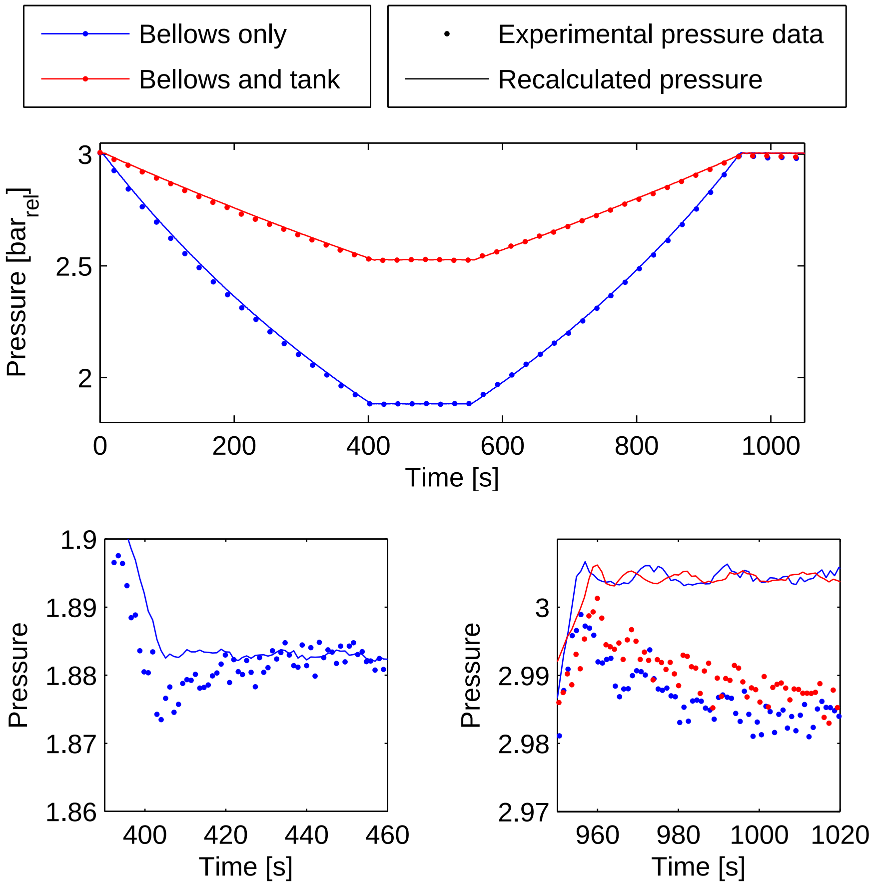

(a) (b)

Figure 3.8: Measured pressure versus pressure calculated with the perfect gas equation (2.15) in which the volume variation is computed from the measured displacement and Eq. (2.1) (in which V_{b0} and V_b are estimated from the mean value of the stabilized phase). Top: complete time history with a subset of the measured points. Bottom: (a) zoom at the end of the expansion phase, (b) zoom at the end of the compression phase. Measurements from the *isothermal C* and *isothermal E* tests are used.

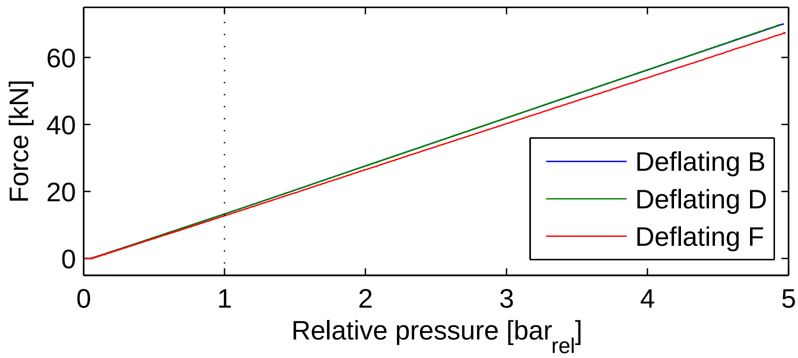

Figure 3.9: Force-pressure diagram during deflating.

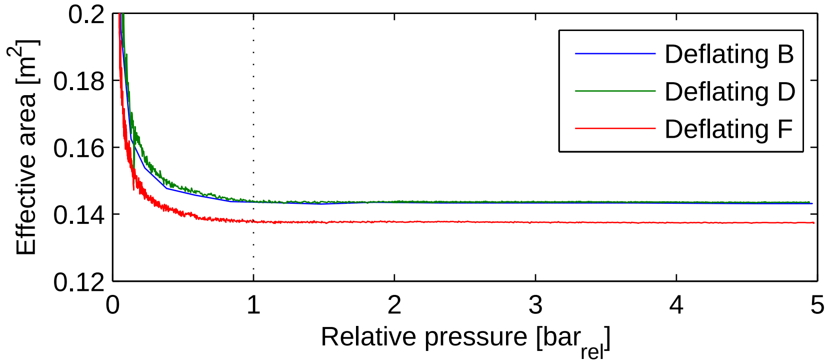

Figure 3.10: Effective area as function of relative pressure during deflating.

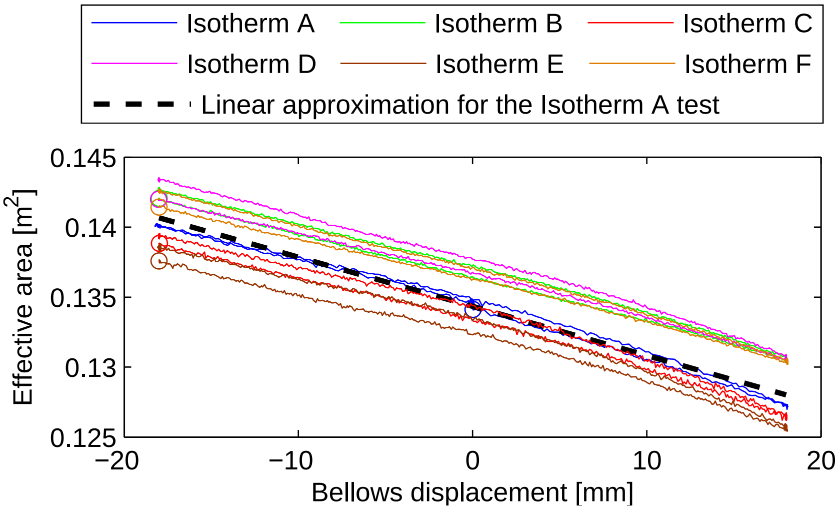

Figure 3.11: Effective area versus bellows displacement during the isothermal test.

shows the evolution of the effective area as a function of the bellows crushing during the isothermal tests. A quite important variability can be observed between the various tests even though the correction force factor calculated with the deflating test is taken into account. Nevertheless, in all the cases, the linear relation (2.3) can be considered:

$$A_e = A_{e0} + \frac{dA_e}{dz} z \tag{2.3}$$

Using initial conditions ($z = -18\ mm$) and conditions obtained at the maximal bellows displacement (i.e. $z = 18\ mm$), this gives for the *isothermal A* test:

$$A_{e0} = 0.134\ m^2 \qquad \text{and} \qquad \frac{dA_e}{dz} = -0.352\ m, \tag{3.6}$$

with 0 conditions for $z = 0\ mm$.

Heat transfer coefficient

The heat transfer coefficient can be estimated on the basis of the step test. Indeed, the gas cools down during the expansion phase, and then warms up toward the ambient temperature during the constant displacement phase inducing a pressure increase. The inverse phenomenon occurs for the compression

phase.
The parameter calculated in the previous sections are introduced in the bellows-tank model established in Chapter 2. Since the pipe dynamics is not important, the incompressible flow approach is used for the pipe modelling. The heat transfer is assumed proportional to the temperature difference between the chamber interior and the atmosphere (see Eq. (2.13)).
First, the *Step C* test is considered (bellows only and $p_0 = 3\ bar$). The test is simulated for various values of the bellows heat transfer coefficient $h_{eq,b}$. The results in Fig. 3.12 show that there is no value that provides a good match for the pressure time history. The value $h_{eq,b} = 3\ W/K$ seems to have the same slope globally than the experimental curve in the logarithmic decrement figures. However the peak is quite strongly overestimated in this case. The value $h_{eq,b} = 10\ W/K$ looks better when looking at the linear scale diagram of the compression phase. But for the expansion phase the experimental curve decreases more slowly.
Assuming $h_{eq,b} = 10\ W/K$, the bellows-tank case is now simulated for various values of the tank heat transfer coefficient $h_{eq,t}$ (*Step E* test). Same remarks as for the "bellows only" case apply, but here, $h_{eq,t} = 5\ W/K$ appears to be the best approximation (see Fig. 3.13).
It clearly appears that the temperature decrement in the logarithmic diagrams is not exactly linear, as it would be the case if the heat transfer obey the relation (2.13), at least when only the cushion is considered. It thus can be thought that the heat transfer does not simply occur between the chamber gas and the atmosphere. We will therefore investigate whether the thermal inertia of the air spring and the tank can affect the results.

In order to take the thermal inertia of the bellows and tank materials into account, we use the lumped model of Section 2.4 for each chamber:

$$\begin{aligned} \dot{Q} &= h_i(T - T_w); \\ \dot{T}_w &= \frac{1}{Mc}\left(h_a(T_{atm} - T_w) + h_i(T - T_w)\right); \end{aligned} \qquad (2.14)$$

The models are calibrated in the same way as previously: the *step C* test (bellows only and $p_0 = 3\ bar$) is firstly used to determine the bellows parameters. Fig. 3.14 compares experiment and simulation results obtained with the following parameters:

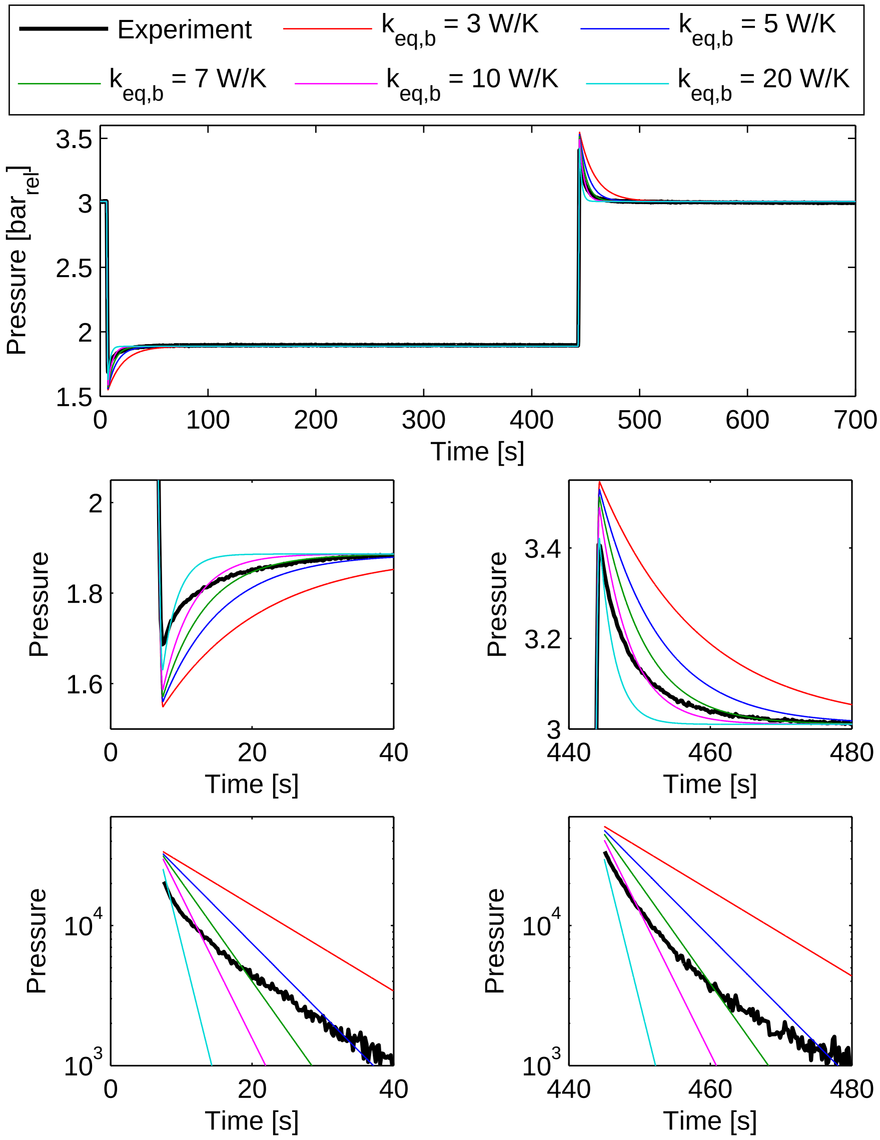

Figure 3.12: Comparison of simulation and experiment results for the pressure time history of the *step C* test. Top: complete time history. Middle: zoom on the expansion phase (left) and on the compression phase (right). Bottom: zooms on the difference between the current value and the stabilized value using a logarithmic scale.

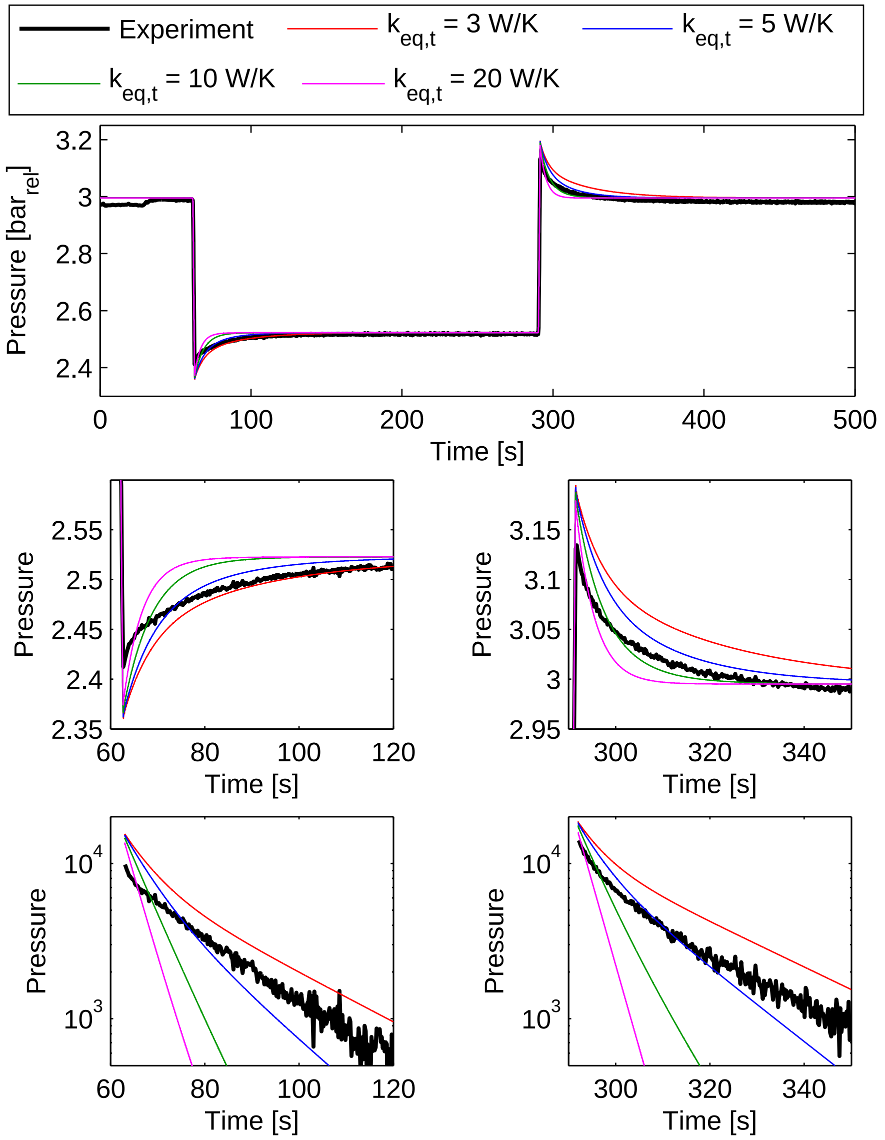

Figure 3.13: Comparison of simulation and experiment results for the pressure time history of the *step E* test. Top: complete time history. Middle: zoom on the expansion phase (left) and on the compression phase (right). Bottom: zooms on the difference between the current value and the stabilized value using a logarithmic scale.

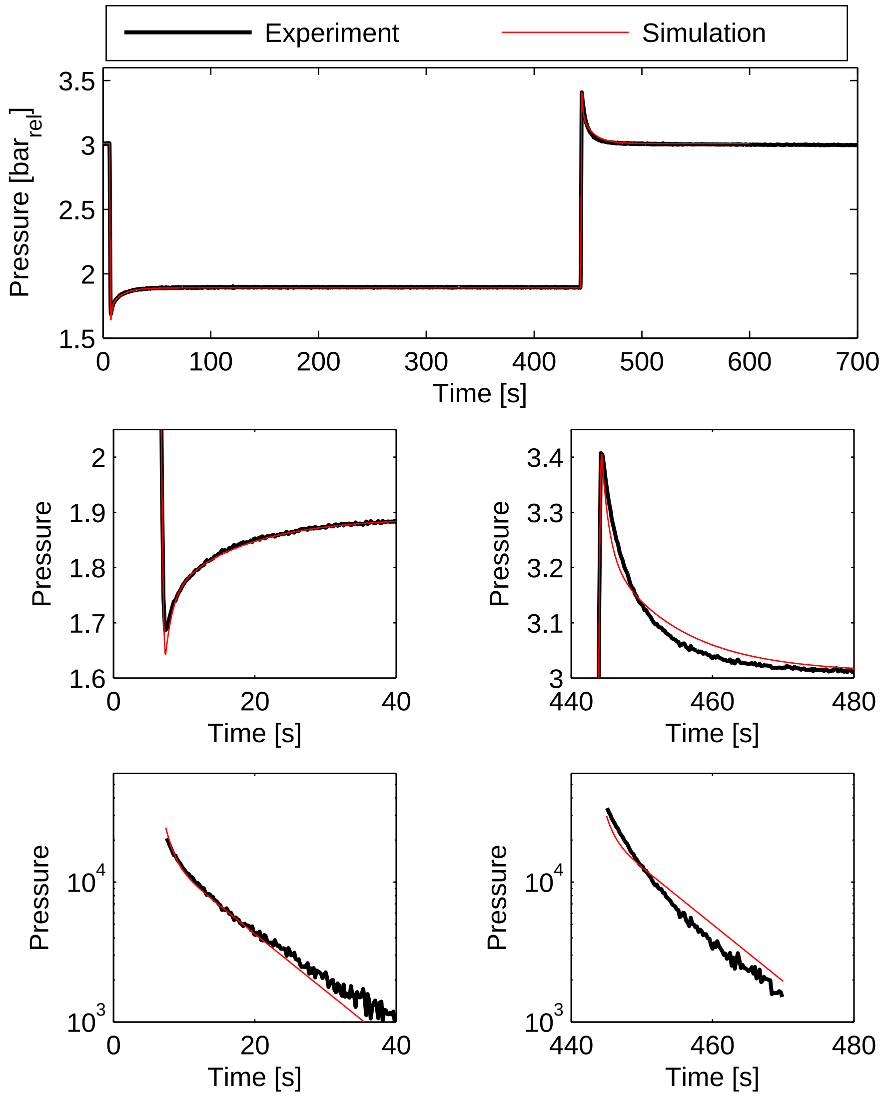

Figure 3.14: Comparison of simulation and experiment results for the pressure time history of the *step C* test. Top: complete time history. Middle: zoom on the expansion phase (left) and on the compression phase (right). Bottom: zooms on the difference between the current value and the stabilized value using a logarithmic scale.

$$h_{i,b} = 25\ W/K, \qquad h_{a,b} = 12.5\ W/K, \qquad (Mc)_b = 83.3\ J/K,$$

where subscripts b refer to the bellows parameters. Then, the auxiliary tank values are estimated on basis of the *step E* test for which the complete system is considered, keeping the previously determined parameters of the bellows. Fig. 3.15 illustrates results obtained with the following values for the tank:

$$h_{i,t} = 17\ W/K, \qquad h_{a,t} = 7\ W/K, \qquad (Mc)_t = 150\ J/K,$$

where subscripts t refer to the tank parameters.

Physically speaking, the obtained values seem too small. For instance, for the tank, we have $M \approx 12\ kg$ and $c \approx 450 J/kg/K$ (steel specific heat capacity), and thus we should find $Mc \approx 5400\ J/K$ which is more than thirty times the obtained value. For the air spring, the calculation is more complex since it is mainly composed of two materials (rubber and steel) and, due to its complex shape, the mass to be taken into account is more difficult to estimate.

This analysis shows that considering a uniform temperature in the wall does not correspond to the reality. For the bellows, since the involved air mass is quite small compared to the steel and rubber masses, the heat transfer would be better approached by considering a heat transfer between the air and a semi-infinite media. This is reinforced by the presence of the helical emergency spring inside the cushion. Concerning the tank, its wall thickness is smaller and it is essentially composed of steel which presents a good thermal conductivity. Therefore, the outer part of the wall is affected by the temperature variations inside the chamber. Considering a heat flow that establishes between the inner and the outer walls would be more realistic. Nevertheless, establishing a more accurate and more physical model of the heat transfer would require further experiments and further measurements which are beyond the scope of this thesis. The proposed model is satisfactory enough to deal with the analysis of a complete railway vehicle.

Fig. 3.16 shows the temperature time history for the *step E* test. The experimental measurements and simulation results are compared. The thermal inertia model was used and therefore both the air temperature and the wall temperature are plotted. Concerning the bellows, we observe that the measured temperature varies less than the calculated ones. For the tank, the experimental curve is closer to the model wall temperature. It seems that the

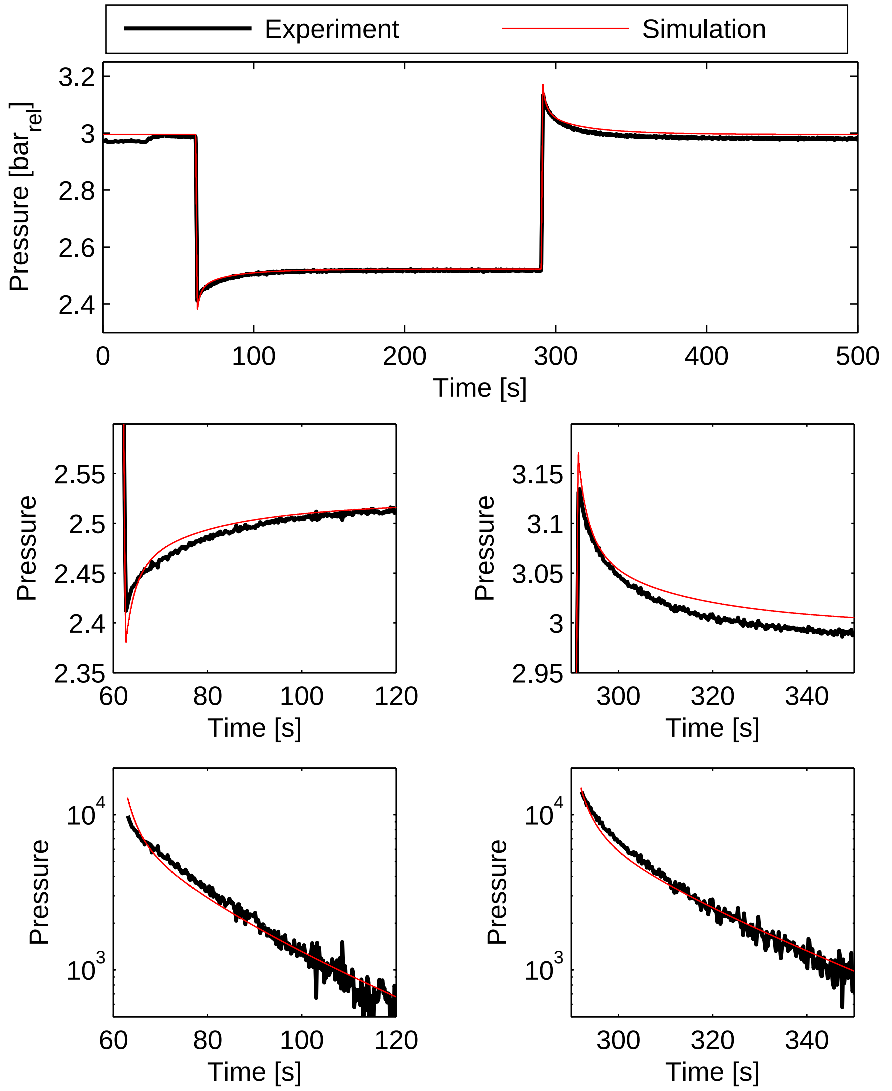

Figure 3.15: Comparison of simulation and experiment results for the pressure time history of the *step E* test. Top: complete time history. Middle: zoom on the expansion phase (left) and on the compression phase (right). Bottom: zooms on the difference between the current value and the stabilized value using a logarithmic scale.

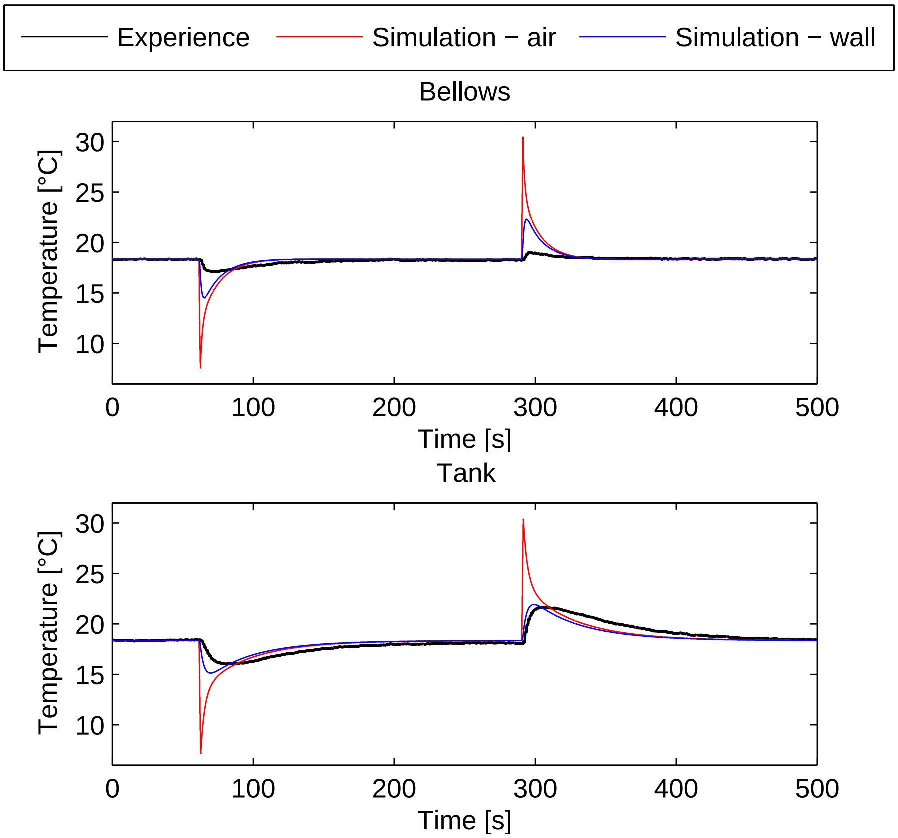

Figure 3.16: Comparison of simulation and experiment results for the temperature time history of the *step E* test.

experimental data follows the simulation temperature with a rather important delay. This would lead to conclude that the wall temperature was measured instead of the air temperature!

Even though the experimental and simulation temperatures do not match, those tests give a good indication about the influence of heat transfer on the suspension dynamic response. Heat transfer coefficients can be estimated for the two heat transfer models presented in Section 2.4. Nevertheless, in running conditions, those parameters could be affected by the convection mode that could be closer to forced convection than natural convection because of the vehicle speed.

3.3 Dynamic experiments

3.3.1 Test description

During this test, the air spring was submitted to a sinusoidal displacement excitation. Several frequencies were tested for a given displacement amplitude in order to highlight the resonance effect revealed in Chapter 2. Unfortunately, because of the limited capacity of the electro-valve used to drive the hydraulic cylinder, a trade-off between the excitation amplitude and the maximal frequency had to be taken. Most of the tests were performed in the $0.5\ Hz - 10\ Hz$ range. It was possible to reach $20\ Hz$ for the smallest amplitude ($1\ mm$). The various test conditions are listed in Table 3.5.
For each frequency, several samples were recorded. For each of them an harmonic decomposition of force measurements was computed and the fundamental mode was used to calculate the dynamic stiffness.
For the highest frequencies, the force measurements are disturbed by the inertia effect due to the emergency spring and force sensor acceleration. Instead of trying to correct the experimental data, the force is recalculated from pressure measurements using Eq. 2.2 ($F = A_e(p_b - p_a)$). This method has the advantage to eliminate the uncertainty due to effective area estimation (see Section 3.2.2) since the force is calculated from pressure values for both experiments and simulations.

The various cases have been calculated with the model parameters esti-

	Assembly	Initial pressure bar_{rel}	Amplitude $[mm]$	Freq. range $[Hz]$
Dyn. A	Bellows - tank - 10 m pipe	3	2.6	$0.5-10$
Dyn. B	Bellows - tank - 10 m pipe	3	5.5	$0.1-5$
Dyn. C	Bellows - tank - 10 m pipe	3	1.0	$0.5-20$
Dyn. D	Bellows - tank - 1.35 m pipe	3	1.0	$0.5-20$
Dyn. E	Bel. - tank - 10 m pipe - orifice	3	2.5	$0.5-10$
Dyn. F	Bellows only	3	2.5	$1-10$
Dyn. G	Bellows - tank - 10 m pipe	5	2.5	$0.25-10$

Table 3.5: Test conditions for the dynamic test.

mated in the previous sections for the bellows and the tank for which the thermal inertia model was used.
Concerning the pipe modelling, the pipe geometry was chosen to emphasize the resonance effect and thus differential models are required. It was checked that compressible and incompressible approaches give similar results. The length and the diameter of the pipe can be determined by simple geometrical measurements. When different pipes segments are connected (galvanized steel pipe and flexible hose), unique equivalent diameter and length are calculated so that the total internal volume of the duct is conserved. Only the pressure loss coefficient remains unknown. It is the reason why we will determine it for each pipe configuration on basis of the observed resonance effect amplitude. We will then check that the obtained values are plausible with respect to standard pressure drop tables.

In the following sections, the several test conditions are analysed. In each case, the experiment and simulation results are compared.

3.3.2 Influence of the displacement amplitude

During the *Dyn. A, Dyn. B* and *Dyn. C* tests, the system was excited with amplitude varying between 1 mm and 5.5 mm. For the 5.5 mm amplitude, the maximal frequency was limited to 5 Hz.
For the simulation parameters, since both incompressible and Fanno models

do not take into account the accumulation of air in the pipe, the duct volume must be added to the connected chamber. Therefore, one half of the volume is added to the cushion and the other half is added to the tank. The following parameters are thus used:

- bellows volume: 15.75 dm^3,
- tank volume: 24.1 dm^3,
- pipe length: 10 m,
- pipe diameter: 15.5 mm,
- total pressure drop coefficient: 58.

The pressure drop coefficient was determined on basis of the 1.3 mm amplitude test to have a good correspondence between experiment and simulation, as illustrated in Fig. 3.17. It appears that this value gives a good fit for the two other amplitudes, both for the dynamic stiffness and the phase angle. However, for high frequencies, the experimental phase angle reaches a non-null constant level whereas the simulation curves tends toward zero. We have no sure explanation for that. Nevertheless, it is coherent that the numerical values reach zero since, for high frequencies, there is no more mass flow through the pipe and then no damping anymore. For the experimental results, the remaining phase angle could be due to the influence of other parts of the system, such as the dissipation of the cushion rubber or the dissipation due to air motions inside the chamber and in the first part of the pipe.
Furthermore, it can be noted that the resonance effect is more pronounced for small excitation amplitude. This is in good agreement with other tests presented in the literature such as in Refs. [12] and [26].

3.3.3 Influence of a damping device

On some railway vehicles, restriction orifices are placed on the duct to increase the suspension damping. In order to test the influence of such device, a restriction was added to the system (*Dyn. E* test). It consists of a 40 mm long piece of pipe with a 6 mm inner diameter. Note that the multiple pipe diameter adaptors and the additional quick-coupling also contribute to increase the loss coefficient.

Concerning the model, it is assumed that the pipe length is not affected by this damping device because the additional air volume is very small. Therefore, only the pressure drop coefficient has changed.
Fig. 3.18 compares the experiment and simulation results of the *Dyn. E* test with the *Dyn. A* case for which the original duct was used. The *Dyn. E* test calculation was performed with the following parameter modification:

- total pressure drop coefficient: 87.

As expected, the additional pipe restriction increases the pressure drops and therefore limits the maximal dynamic stiffness. Note that the difference between the two curves could have been greater if the same excitation amplitude had been used. For the additional orifice, a smaller amplitude was used which increases the resonance effect, according to the conclusions of Sections 3.3.2 and 2.5.1.

3.3.4 Influence of the auxiliary tank

Fig. 3.18 also presents the results obtained when only the air spring is excited. The considered volume is the volume calculated in Section 3.2.2. For high frequencies, the dynamic stiffness simulation curve shows the influence of the volume difference due to the duct volume. This difference seems less important for the experimental data.

3.3.5 Influence of the pipe length

To test the influence of the pipe length, the galvanized steel duct is bypassed and the bellows flexible hose is directly connected to the tank one. Since, according to Section 2.5.1, the resonance effect moves toward high frequencies when the pipe length is reduced, the smallest excitation amplitude was used so as to test the system in the $0 - 20\ Hz$ frequency range (*Dyn. D* test). For the simulation, the following parameters are used:

- bellows volume: 14.86 dm^3
- tank volume: 23.28 dm^3
- Pipe length: 1.35 m
- Pipe diameter: 13.7 mm

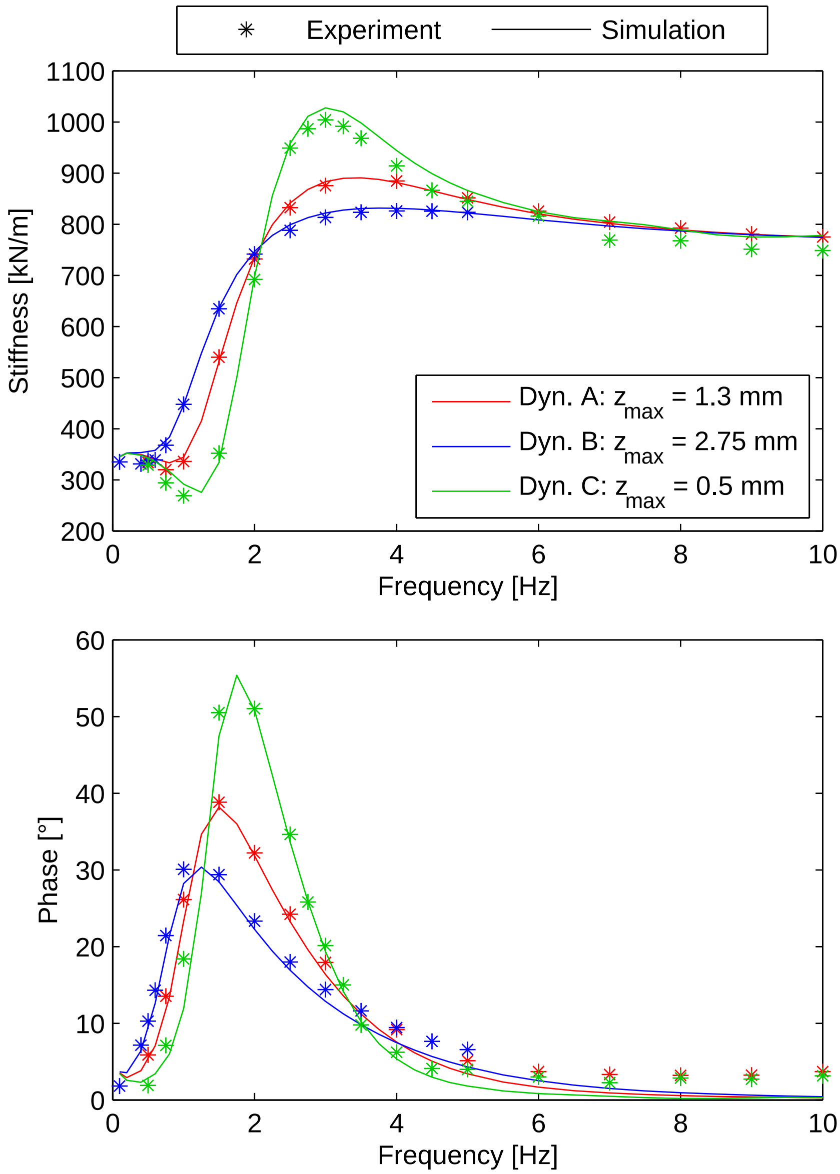

Figure 3.17: Influence of the excitation amplitude on the dynamic stiffness (top) and phase angle (bottom).

		10 m pipe	10 m pipe + orifice	1.35 m pipe
Simulation coef	ξ_{simu}	58	87	16
Estimated coef				
distributed	$\lambda L_p/d_p$	23	23	1.1
lumped	ζ_{tot}	35	64	14.9
Elements		Number of elements		
Elbow	n_{elbow}	8	8	1
Quick-coupling	$n_{coupling}$	2	3	1
Restriction orifice	$n_{orifice}$	0	1	0

Table 3.6: Upper part: summary of calculated and estimated pressure drop coefficients for each duct configuration. Lower part: number of main components causing located pressure loss.

- Pressure drop coefficient: 16

Experimental data and simulation results are compared in Fig. 3.19 for the *Dyn. D* and *Dyn. C* tests. Even though the pressure drop coefficient has been tuned to obtain a good match, this parameter does not control the whole curve. It is therefore important to note that, except for high frequencies in the case of the *Dyn. C* test, the experiment and simulation give coherent results. As expected the eigenfrequency is shifted toward higher values when the pipe length is reduced. The resonance effect in the dynamic stiffness curve is also less important in the case of the shortest duct.

Even though further experiments should be performed so as to check the robustness of the loss coefficient parametrization, Table 3.6 gives interesting hints about the obtained values.
Table 3.6 first records the total pressure drop coefficient ξ_{simu} used in the numerical analysis for the various cases. It also mentions the distributed pressure drop coefficient $\lambda L_p/d_p$ calculated on basis of the pipe dimensions and the Colebrook formula for fully turbulent flow and assuming hydraulically rough regime (Eq. (2.29)). The remaining lumped pressure drop coefficient is calculated as the difference between the simulation coefficient and the estimated distributed coefficient:

$$\zeta_{tot} = \xi_{simu} - \lambda L_p/d_p.$$

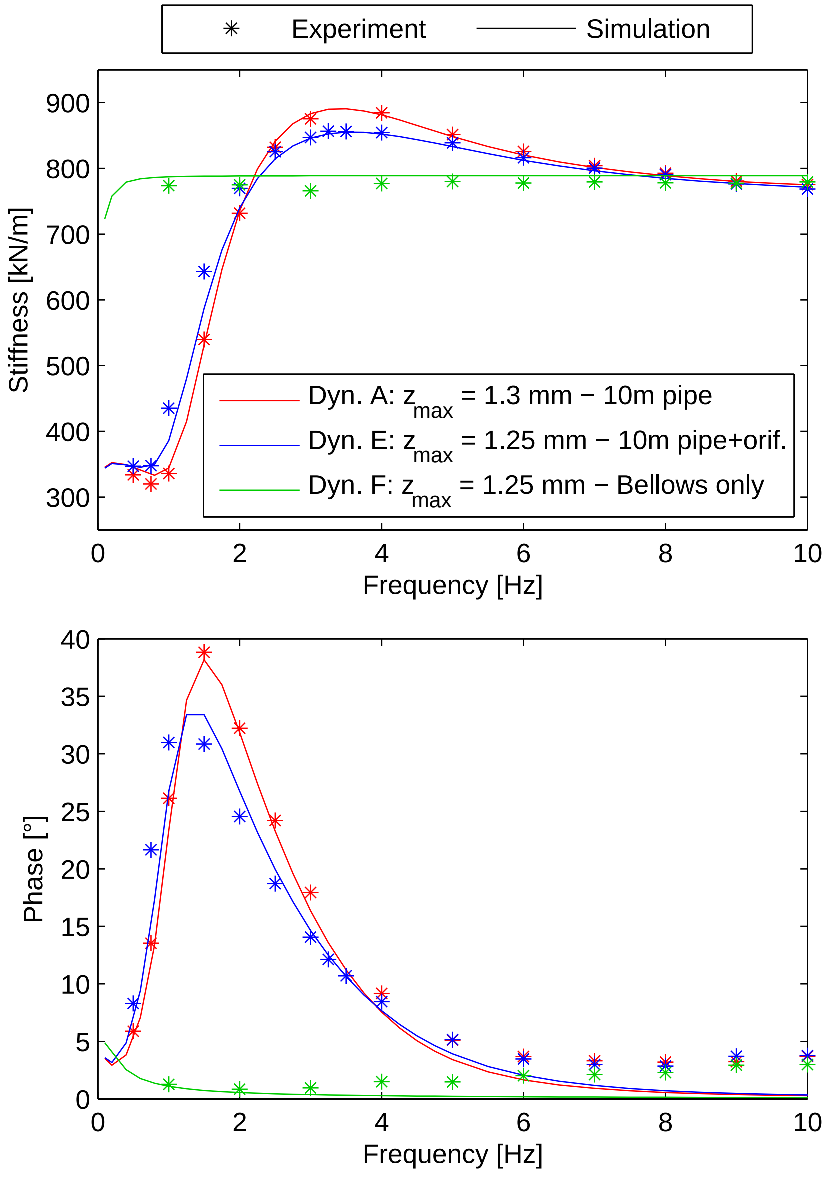

Figure 3.18: Influence of a damping device on the dynamic stiffness (top) and phase angle (bottom). The figure also shows the curve obtained when only the air cushion is excited.

In the second part of Table 3.6, the potential source of pressure loss (elbows, quick-couplings and restriction orifices) are enumerated for each duct configuration. We could try to estimate the loss coefficient of each element on basis of tables such as the ones available in Ref. [38] but it is difficult to find an exact value because of the geometrical complexity of components such as a quick-coupling or a pipe reduction adaptor. However, using a "reverse engineering" approach, it is possible to roughly estimate the pressure drop coefficient of each element. Since, for an incompressible flow, the coefficients of each element are added to obtain the total coefficient, we should have, for each pipe configuration:

$$\zeta_{tot} = n_{elbow}\zeta_{elbow} + n_{coupling}\zeta_{coupling} + n_{orifice}\zeta_{orifice} + \zeta_{end}; \tag{3.7}$$

where: n_i is the number of each element;
ζ_i is the associated loss coefficient;
$\zeta_{end} = 1$ is the loss coefficient of a pipe exit.

Applying Eq. 3.7 for the three pipe configurations, we obtain a system with three equations and three unknowns which allows us to estimate the loss coefficient of each element, as it appears in the following table:

component	elbow	quick coupling	restriction orifice
ζ	...1...	...13...	...16...

After checking several sources in the literature such as [38], those values seem rather realistic. The quite important loss coefficient for the quick coupling can be explained by the presence of an anti-back-flow device that automatically closes the pneumatic circuit if its two parts are decoupled. Let us note that we have only considered the main loss elements. We have for instance neglected the inflow losses at the upstream pipe end. Therefore, a deeper investigation of the literature or additional experiments could provide more accurate coefficients for the various components of a pneumatic suspension circuit.

Even though the incompressible model gives satisfactory results for the $0-10\ Hz$ frequency range, it must be noticed in Fig. 3.19 that, for the long pipe configuration, a discrepancy appears in the dynamic stiffness graph between 12 and 20 Hz. For these frequencies, the experimental phase angle shows a second resonance. In order to highlight this effect, the dynamic stiffness curve has been calculated with the discretized one-dimensional unsteady flow model integrated

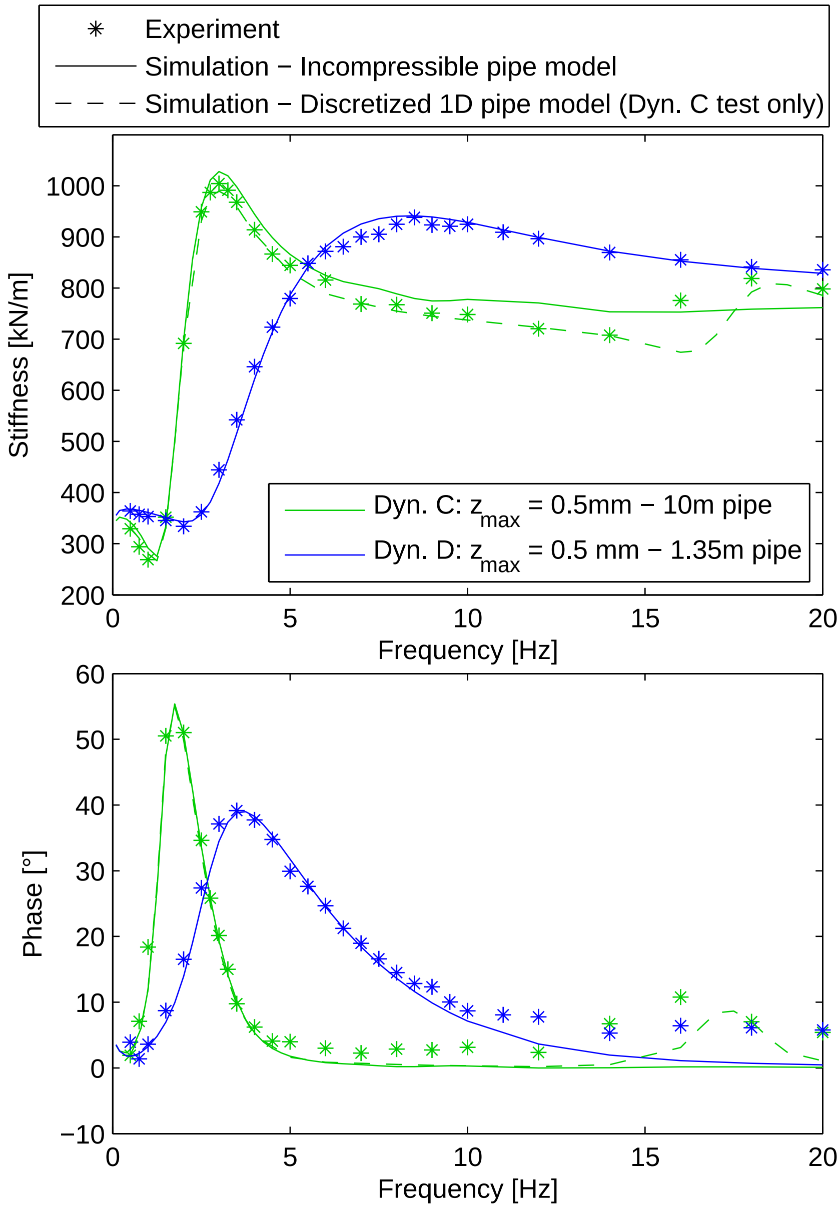

Figure 3.19: Influence of the pipe length on the dynamic stiffness (top) and phase angle (bottom).

with the Lax-Wendroff scheme (see Section 2.5.3). Since singular losses are not taken into account by this approach, the distributed loss coefficient has been set such as to obtain an equal total pressure drop coefficient.
It appears that the resonance effect is quite well caught by the discretized model, with a small frequency shift (of about 1.5 Hz). This model shows that, for these frequencies, the mass flow at the two pipe ends are in opposite phases: air is entering or exiting the pipe via its two ends at the same time, inducing larger pressure variation in the middle of the pipe than at its two extremities. This effect can not be captured by the incompressible model or by the Fanno based model since they consider a uniform mass flow throughout the pipe.

3.3.6 Influence of the initial pressure

The last parameter variation concerns the initial pressure, which, in practice, depends on the load carried by the suspension. In Fig. 3.20, the cases of a 3 *bar* (*Dyn. A* test) initial pressure and a 5 *bar* (*Dyn. G* test) initial pressure are compared. The increased stiffness due to the higher pressure is illustrated in Fig. 3.20. The resonance effect keeps proportionally the same amplitude for the two curves. It also clearly appears that the pressure has no effect on the phase angle, as it was observed in Refs. [12] and [26].
A small difference between experimental and simulation results is observed for the high pressure. It can be mainly explained by the pressure loss during the test. The simulation curve obtained with 4.84 *bar*, the pressure measured at the end of the test, gives a better fit.

3.3.7 Heat transfer remarks

During the dynamic test, no significant temperature variations were observed. This is due to the displacement which remained quite small. Indeed, for the tested amplitude, the numerical analysis reveals that the temperature does not really vary.
Nevertheless, a final test performed at the end of the experimental process highlighted more important temperature increase when the cushion is excited with larger amplitude even for low frequencies. The temperature time history obtained with a 40 mm displacement amplitude and a 0.5 Hz frequency is plotted in Fig. 3.21. The wall temperature obtained via the numerical integra-

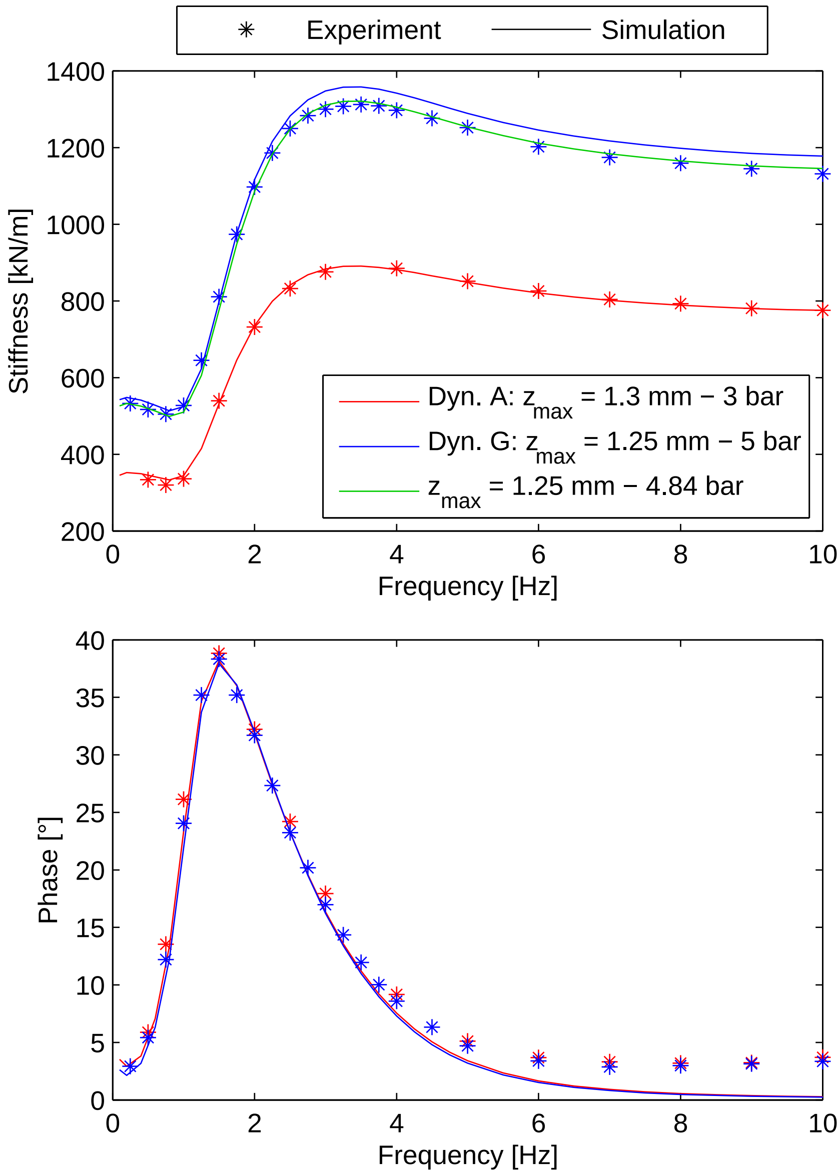

Figure 3.20: Influence of the initial pressure on the dynamic stiffness (top) and phase angle (bottom).

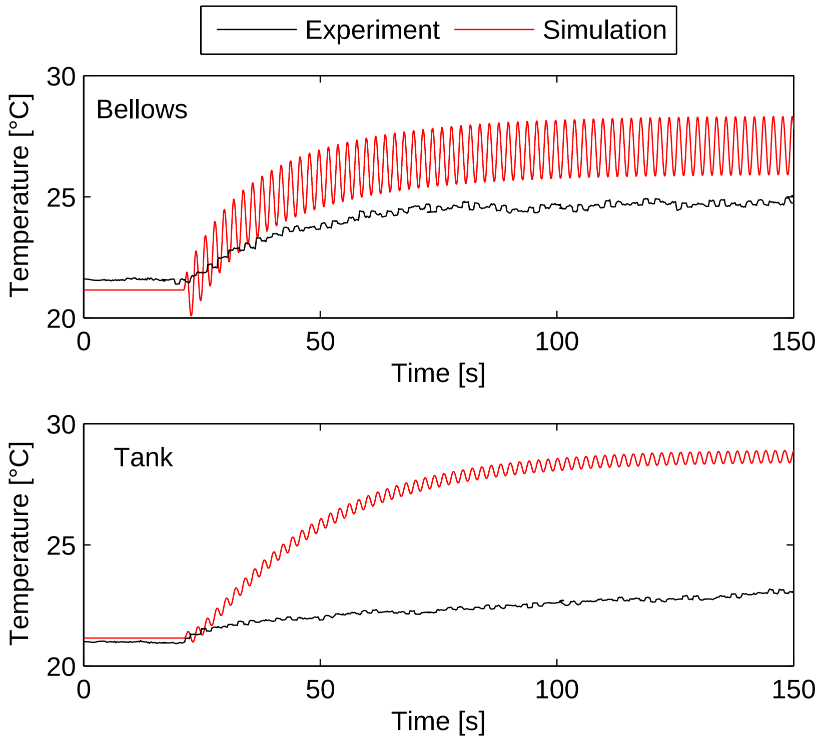

Figure 3.21: Comparison of experiment and simulation temperature time histories for a test performed at low frequency ($0.5\ Hz$) and large amplitude ($20\ mm$).

tion is also shown. A difference of $2\ °C$ is observed for the bellows but we are not sure that the initial temperature was corresponding to the ambient one. Concerning the tank, the experimental curve varies more slowly. It is certainly due to the fact that the galvanized duct was not insulated, the flow being then not adiabatic, contrary to the model assumption.

3.4 Conclusion

In this chapter, we determined the whole set of model parameters presented in Chapter 2. We first focused on the cushion parameter for which we confirmed the linear dependence of the volume V_b and effective area A_e with respect to the bellows displacement z. Order of magnitude for the heat transfer coefficients of the two heat flow models presented in Section 2.4 were also given on basis of the quasi-static step test. It would be interesting to check the obtained values using a sinusoidal excitation performed at low frequency and with a large amplitude.

Finally, the pipe loss coefficient was assessed on basis of the resonance effect observed for dynamic stiffness curves. The dynamic experiment revealed a good match between experimental and simulation curves. It appeared that the differential compressible model was sufficient to achieve those results.

Chapter 4

Railway modelling applications

In Chapters 2 and 3, we have shown that a pneumatic suspension can be suitably modelled using a thermodynamical approach. In this chapter, we will present how pneumatics and multibody dynamics can be coupled so as to analyse the global behaviour of a railway vehicle and its pneumatic suspension.
In the first section, we describe the analysed vehicle and we explain how the multibody model and the pneumatic equations are coupled. We then define four tests for which the system is analysed showing the influence of the various pneumatic models. Finally, we take advantage of the flexibility of the developed approach in order to compare various pneumatic circuit topologies and investigate the performance of novel morphologies.

4.1 Vehicle description

4.1.1 Main properties

The vehicle used in the present study corresponds to a single metro car equipped with two conventional bogies. A characteristic of such a train is that it is submitted to important load variations in running conditions: the carbody mass doubles when passing from an empty situation to full occupancy. The main parameters of the coach are listed in Table 4.1.

Carbody mass	17 000	kg
Bogie frame mass	1 900	kg
Wheelset mass	800	kg
Bogie center distance	10	m
Wheelset base distance	2	m
Primary suspension stiffness		
Longitudinal (x)	9000	kN/m
Lateral (y)	4500	kN/m
Vertical (z)	1000	kN/m
Secondary suspension stiffness		
Longitudinal (x)	500	kN/m
Lateral (y)	500	kN/m

Table 4.1: Main characteristics of the analysed vehicle in the empty situation.

In the reference configuration, the vehicle is equipped with a four-point suspension, without any anti-roll bar nor hydraulic damper. The auxiliary tanks are placed next to the bellows and are directly connected via orifices (i.e., there is no pipe). The pressure differential valves placed between the left and right auxiliary tanks are set with a 2.25 *bar* engaging value.

4.1.2 Multibody modelling of the vehicle

Main toplogy. The multibody model of the vehicle is implemented with the multibody package Simpack. As it can be observed in Fig. 4.1, it is composed of three main parts: the *carbody* and the two *bogies*. The carbody flexibility is neglected and it is therefore modelled as a single rigid body. The bogies, implemented as Simpack substructures, are composed of four bodies:

- the *traverse* which is rigidly fixed to the carbody in the complete system and is connected to the bogie frame via the secondary suspension;
- the *bogie frame* which has six degrees of freedom with respect to the rail;
- the two *wheelsets* whose positions are defined using a six degrees of freedom joint but their motion is restricted by the wheel/rail contact that induces two algebraic constraints for each one.

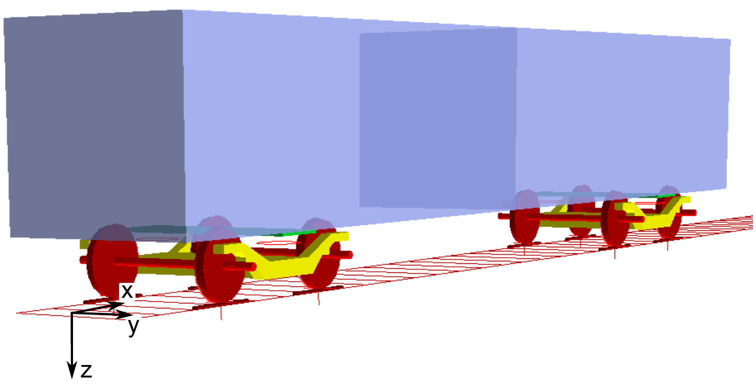

Figure 4.1: Illustration of the SIMPACK multibody model of the vehicle.

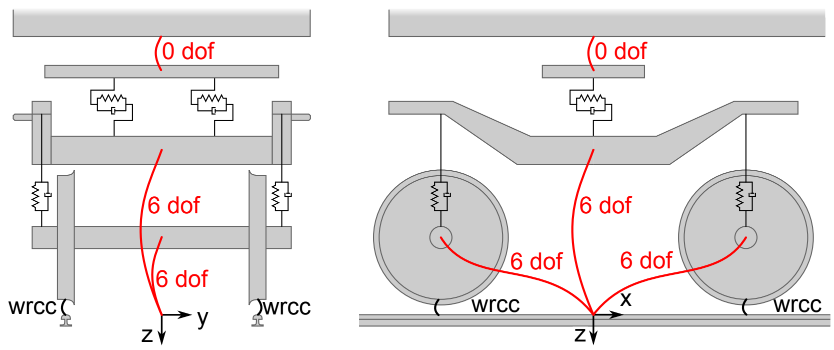

Figure 4.2: Multibody model of the bogie (dof: dregrees of freedom; wrcc: wheel/rail contact constraint).

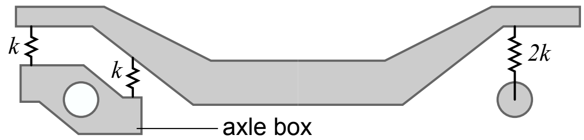

Figure 4.3: Multibody modelling of the primary suspensions and axle boxes.

Force elements. Classically, components such as the suspension take part to the system dynamics, not because of their mass but via the forces they apply on the linked bodies. They are therefore modelled using force elements and their mass can be added to the main bodies. In the present system, the following force elements are considered.

- The *primary suspensions* are modelled via linear springs and dampers in parallel with different stiffness and damping in each direction. The associated force elements are directly connected between the bogie frame and the wheelsets. The axle boxes that contains the wheelset bearings are neglected, as illustrated in Fig. 4.3.

- For the *secondary suspensions*, since the present work focuses on the vertical behaviour of the pneumatic suspensions only, the horizontal interaction forces are implemented in the multibody environment using linear spring-damper elements.

- The *secondary vertical bumpstops* are modelled using high stiffness elements. A force is exerted only if the vertical secondary suspension displacement is larger than 20 mm in compression or extension.

- The normal component of the *wheel/rail contact force* is taken into account via the constraints that impose the contact between each wheel and the rail. However, a force element must be added for each wheel so as to include the tangential friction forces. This effort are modelled using the Kalker theory which computes the force from the contact creepages, the normal force and from material properties (Ref. [40]).

Anti-roll bar. In order to analyse a two-point configuration, an anti-roll bar must be added to the system. As depicted in Fig. 4.4, it is classically introduced

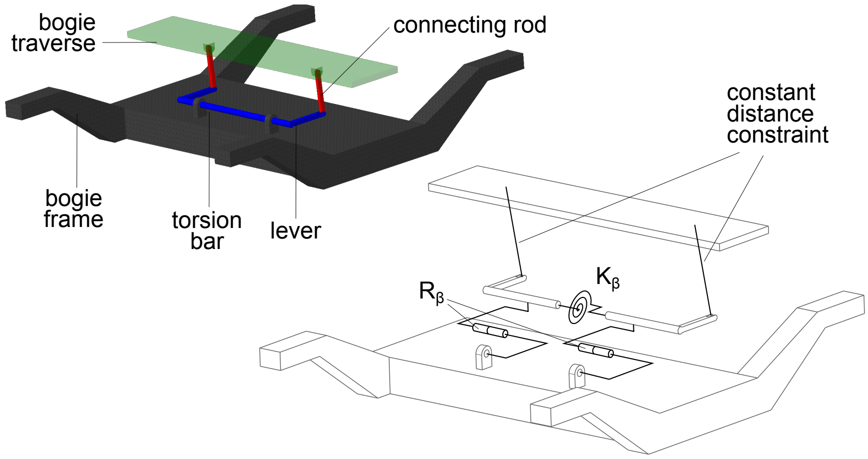

Figure 4.4: Illustration of the anti-roll bar modelling.

in the multibody model via a lumped modelling approach. Two rigid bodies are used: each one represents a half of the torsion bar and one lever. They are fixed to the bogie frame via two revolute joints along the transverse axis (R_β in Fig. 4.4). Between those two bodies, a torsional spring element (K_β in Fig. 4.4) is added so as to represent the torsional stiffness of the anti-roll bar. The connecting rod located between the bogie traverse and each lever is taken into account via a constant distance constraint, its mass being negligible.
The roll stiffness of this device is related to the stiffness of the torsion bar by the following relation:

$$K_\alpha = \left(\frac{l}{a}\right)^2 K_\beta \tag{4.1}$$

with: K_α, the roll stiffness $[Nm]$;
K_β, the equivalent stiffness of the torsion bar $[Nm]$;
l, the torsion bar length $[m]$;
a, the lever length $[m]$.

4.1.3 Pneumatic modelling

The pneumatic suspension corresponds to that tested in Chapter 3 (see Table 4.2). The cushion parameters are those obtained in Section 3.2.2. Concerning the auxiliary tank, the volume of Chapter 2 is used. The heat transfer is

Nominal bellows volume	V_{b0}	14.9 dm^3
Bellows volume gradient	dV_b/dz	0.135 m^2
Effective area	A_e	0.134 m^2
Effective area gradient	dA_e/dz	-0.352 m
Tank volume	V_t	27 dm^3
Orifice diameter	d_p	9 mm
Loss coefficient	ζ	1.5
Levelling valve dead band for admission		3 mm
Levelling valve dead band for exhaust		-3 mm
Safety valve engaging value		-14 mm
Pressure differential set point		2.25 bar

Table 4.2: Main parameters of the pneumatic circuit.

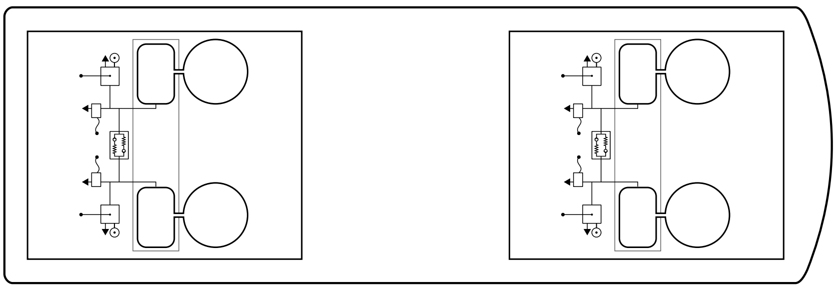

Figure 4.5: Pneumatic circuit of the reference vehicle.

modelled using the simplest model for which the heat flow is proportional to the temperature difference between the chamber and the atmosphere (Eq. (2.13)). Since there is no pipe but only an orifice between the auxiliary tank and the air spring, the algebraic incompressible model is used (*model 4* in Section 2.5.1). The approach based on the *ISO* 6358 standard could also be retained (*model 5* in Section 2.5.1).

4.1.4 Implementation: coupling via co-simulation

The multibody and the pneumatic models are coupled using the co-simulation technique. There are consequently two parallel integration processes that interact at fixed time step. The output of one system is the input of the other and vice versa. As shown in Fig. 4.6, the following data are exchanged between the two models during the interaction phase:

- multibody output / pneumatic input:
  - vertical positions of secondary suspension connection points (z);
  - vertical velocities of secondary suspension connection points ($\dot{z}$);
  - levelling valve lever displacement (L);
  - safety valve lever displacement (L);
- pneumatic output / multibody input:
  - vertical component of the reaction force of the bellows acting on the bogie frame and the traverse (F).

The same multibody output is used for the levelling valve and the safety valve levers (L) because those two components are placed close to each other.

The pneumatic models have been implemented using the C programming language. A user interface has been developed in order to easily create the code of a given suspension circuit. Once the C code is written, it is compiled so as to obtain a MATLAB/SIMULINK S-FUNCTION. This one is coupled to the SIMPACK model using the SIMAT co-simulation block (see Fig. 4.7). This block ensures the communication between the Simulink and Simpack time-integration processes.

On one hand, the pneumatic equations are solved using the *ode45* integrator

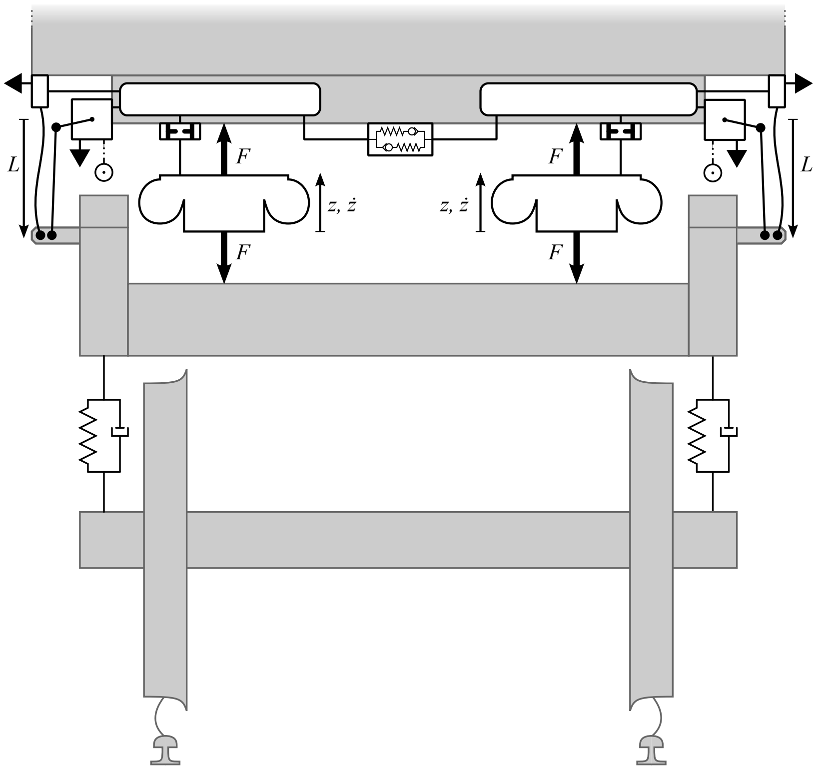

Figure 4.6: Interaction between the multibody system and the pneumatic circuit.

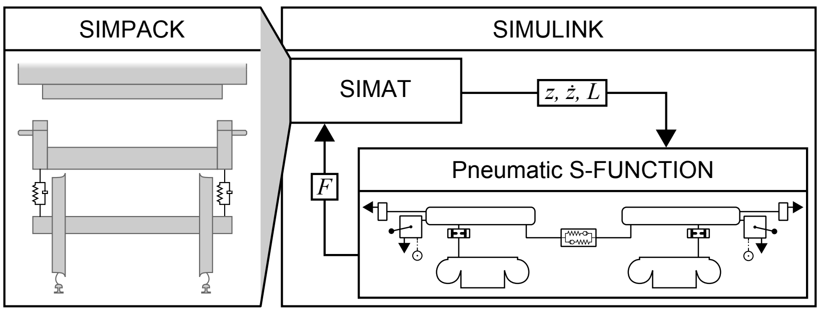

Figure 4.7: Illustration of the model coupling using the SIMAT co-simulation block.

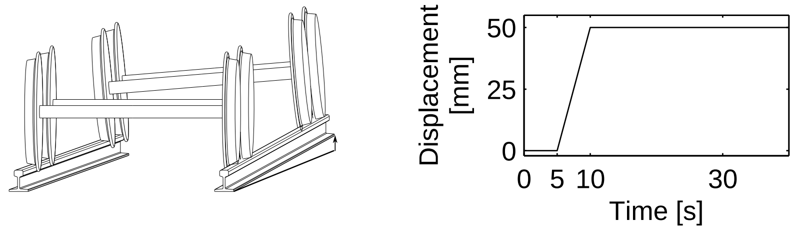

(a) (b)

Figure 4.8: (a) Illustration of the twist excitation. (b) Vertical displacement imposed to the right wheels of the front bogie to simulate the twist excitation.

of SIMULINK which is based on the Dormand-Prince method (see Ref. [23]). On the other hand, the multibody system is integrated with the SIMPACK SODASRT algorithm which is based on the differential-algebraic system integrator DASSL (see Refs. [8, 71] for more details).
The co-simulation time step size has been fixed to 1 ms which is satisfactory for most of the considered tests and is in good agreement with the recommendations of Ref. [9]. The inner time step size of each integration process is equal to the interaction time step size.

4.2 Test description

In this section, we describe the various tests that are implemented to highlight the vehicle performances and to analyse the models presented in Chapter 2.

4.2.1 $\Delta Q/Q$ test

The so-called $\Delta Q/Q$ test consists in measuring the variation ΔQ of the wheel/rail force vertical component $Q(t)$ when the vehicle passes through a rail twist, i.e. a situation in which the two rails are not parallel (see Fig. 4.8(a)). The variation is normalized by the initial value of the force vertical component Q_0:

$$\Delta Q/Q = \frac{Q(t) - Q_0}{Q_0} \tag{4.2}$$

It aims at verifying the vehicle's torsional rigidity to prevent curve derailment. Since the situation is more critical for low speed, the analysis is conducted on

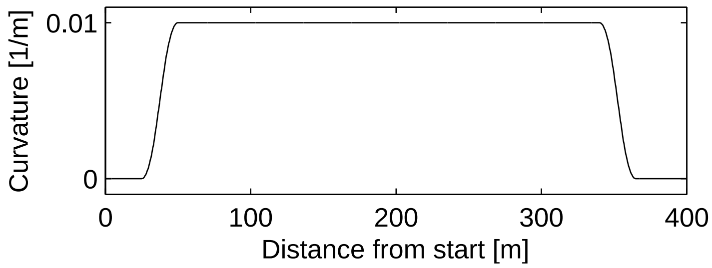

Figure 4.9: Track curvature for the curve passing test.

a stationary train. In practice, such a situation can also occur when a metro is at rest in a station followed immediately by a curve with cant.
The excitation can be applied by placing wedges under the two right wheels of the front bogie or by placing the coach on hydraulic actuators that reproduce the excitation. As a result, the front right and rear left bellows are crushed and the front left and rear right ones are extended. In this situation, the levelling system inflates the crushed bellows and deflates the extended ones. This tends to accentuate the force variation and often lead to large pressure differences between the right and left air springs, so that the pressure differential valve is engaged.
Practically, this test is simulated with the vehicle at rest and by imposing the motion of the two front wheelsets, as illustrated in Fig. 4.8(b). The maximal displacement imposed to the right wheels of the front bogie reaches 50 mm in this case. This value is a good order of magnitude with regards to standards (see Ref. [1]) even though it is not the exact maximal value for this vehicle. The wheelsets are moved between 5 s and 10 s and are then maintained in the twisted position. Both the transient behaviour and the steady state solution are analysed by means of time integration.

4.2.2 Curve passing

Even though we focus on the vertical dynamics of the pneumatic suspension, it is useful to analyse how the vehicle reacts to lateral acceleration. Indeed, the pneumatic cushions must compensate for the centripetal acceleration when

passing a curve, situation in which levelling valves play an important role.
The coach starts running on a straight track with a 10 m/s constant speed. It then passes through a 100 m radius curve without any cant, causing a 1 m/s^2 lateral acceleration. The vehicle finally exits the curve and goes on a straight track. The straight track parts are connected to the curved track via 15 m long transitions as it can be observed in Fig. 4.9.

4.2.3 Loading/unloading in station

It is interesting to analyse how the secondary suspension react when people enter or exit the metro at the station. It must be checked for instance that the bumpstops are never reached and that the valves adapt the air pressure in the suspension quickly enough. It is also an important phase to consider so as to assess the compressed air consumption.
Concerning the modelling, a stationary vehicle without wheel/rail contact model is used. The people mass is represented by a force acting on the carbody. Its intensity is illustrated in Fig. 4.10(a). The initial loading, from 0 s to 30 s represent the ingress of four persons per square meter. The force is maintained until 150 s. Afterwards, the force magnitude is reduced to a value equivalent to the exit of two passengers per square meters. From 165 s to 180 s, the maximal load is applied again. Note that the force application point is moved from the right side toward the center so as to take the passenger ingress motion into account (see Fig. 4.10(b)). The application point is moved in the other sense when passengers are exiting.

4.2.4 Comfort test

This analysis consists of a vehicle running a straight track at a constant speed during 100 s. Stochastic track irregularities are added in the vertical direction and around the track longitudinal axis (i.e., the roll axis). Two vehicle speeds are considered: 10 and 20 m/s.
The passenger comfort is assessed using the vertical acceleration measurements at the floor level in the carbody. A weighted root mean square (RMS) acceleration is computed according to the ISO 2631 standard (Ref. [2]).

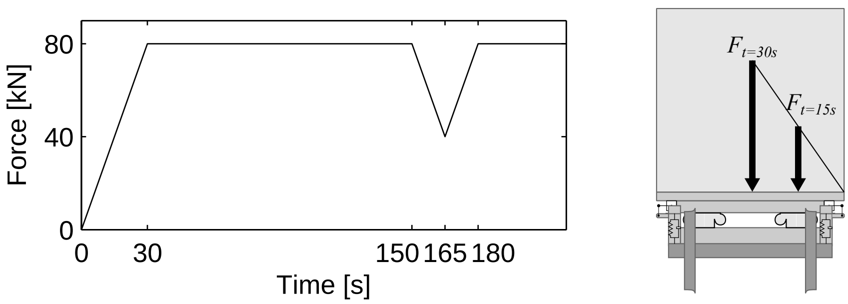

(a) (b)

Figure 4.10: (a) Force magnitude representing the passenger mass for the loading/unloading in station test. (b) Illustration of the lateral motion of the force application point during the first loading phase (Vehicle view along the longitudinal axis).

4.3 Reference vehicle analysis

4.3.1 Curve passing analysis

In this section, we analyse the behaviour of the train for the test defined in Section 4.2.2. We especially investigate the heat transfer influence.

First, we consider that the levelling and safety valves are not connected. As expected, when the vehicle is in the curve (i.e. between 5 s and 55 s), the roll angle is lower for the $h_{eq} = 0$ W/K case because the suspension is stiffer as shown is Chapter 2. The $h_{eq} = 10^4$ W/K case is close to the isotherm behaviour. For the two intermediate values, the roll angle is close to the adiabatic curve ($h_{eq} = 0$ W/K) when entering the curve and then tends towards the isotherm situation. The difference between the $h_{eq} = 10$ W/K and $h_{eq} = 1$ W/K must be noticed since it was shown in Chapter 3 that the heat transfer coefficient is bounded by those two values. The discrepancy is quite significant since one case reaches the isotherm roll angle before the end of the curve while the other stays close to the adiabatic case.
When exiting the turn, a similar behaviour occurs and for the two intermediate transfer coefficient values, the roll angle does not stabilize immediately to zero.

When valves are connected (Fig. 4.12), the differences are less important

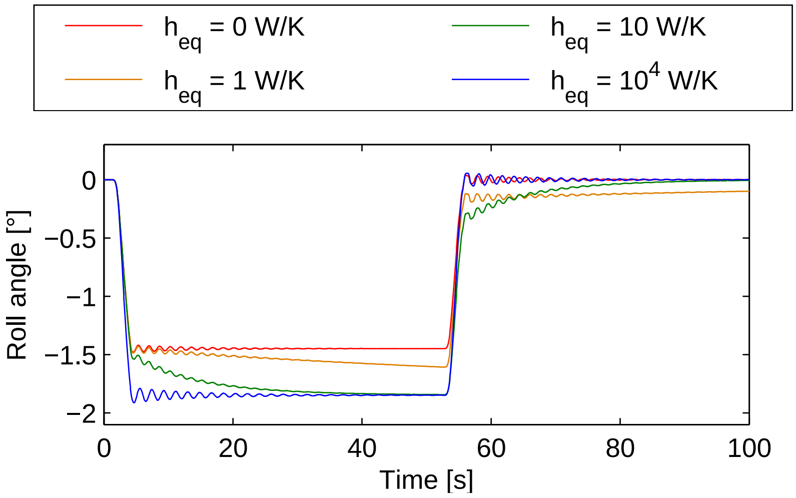

Figure 4.11: Carbody roll angle time history when passing a 100 m radius curve at 10 m/s. Levelling and safety valves are disconnected.

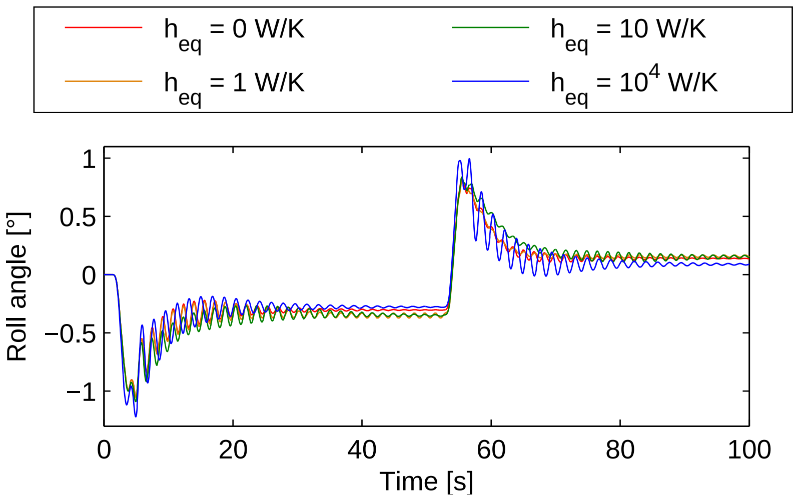

Figure 4.12: Carbody roll angle time history when passing a 100 m radius curve at 10 m/s. Levelling and safety valves are connected.

$h_{eq} = 0\ W/K$	$h_{eq} = 1\ W/K$	$h_{eq} = 10\ W/K$	$h_{eq} = 10^4\ W/K$
$0.049\ kg$	$0.052\ kg$	$0.067\ kg$	$0.072\ kg$

Table 4.3: Total air mass injected in the pneumatic suspension via the levelling valves during the curve entry for several heat transfer coefficient h_{eq} values.

because the levelling valves inflate the outer bellows and deflate the inner ones so as to keep a constant air spring height. In the cases $h_{eq} = 1\ W/K$ and $h_{eq} = 10\ W/K$, there is small oscillations when the train is in the curve because, as the temperature gradually decreases, the air spring stiffness also decreases and the valves are therefore engaged sporadically which prevents the system to reach an equilibrium.
When the coach leaves the curve, a similar phenomenon occurs in the other sense. Due to the air added and removed from the cushions in the curve, the maximal roll angle is almost the same as after the curve entry.
It can also be noticed in Table 4.3 that the isotherm case induces a larger air consumption which is measured by the total air quantity injected from the pressure source towards the bellows via the levelling valves. This analysis demonstrates that the heat transfer influence must be known if the air consumption must be numerically assessed.

4.3.2 Loading/unloading in station analysis

We now analyse the impact of the heat transfer coefficient in the case of the loading/unloading test defined in Section 4.2.3.

Fig. 4.13 presents the left and right front bellows displacements for the initial loading phase. The rear bellows displacements are identical to the front ones.
It can be observed that due to the applied force, the bellows are crushed (negative displacement) and the levelling valves must inject air in the suspension to recover the initial position. Nevertheless, because of the force application point lateral offset, the left bellows are first extended. Consequently, the levelling valves deflate the left air springs in the first seconds. This explain why the maximal compression is then more important than for the right cushions. The bellows displacement stabilizes around $-3\ mm$ and not zero because of

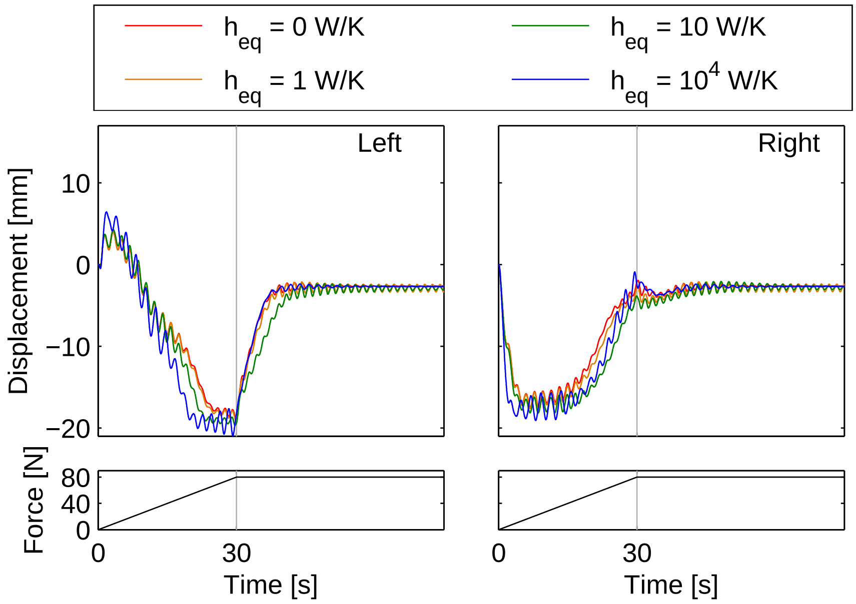

Figure 4.13: Bellows displacement time history for an initial loading in station

the dead band of the valve characteristic.
It also appears that the impact of the heat transfer coefficient is quite limited. In all cases, the bellows crushing approaches the limit value of the bumpstops (which are not activated in this simulation). For the almost isotherm case ($h_{eq} = 10^4\ W/K$), the bumpstop is reached.

During the unloading phase in the intermediate station (Fig. 4.14), the displacement becomes positive and the air exhausts to the atmosphere through the levelling valves. The safety valves are also engaged causing larger oscillations due to the abrupt valve characteristic, especially for the $h_{eq} = 10^4\ W/K$ case.
The ingress of new passengers starts before the carbody comes back in the neutral position. This certainly prevents from larger displacement and limits the air consumption. At this moment, the discrepancies due to the heat transfer coefficient are the most important. The larger quantity of air exhausted during the unloading for the $h_{eq} = 10^4\ W/K$ case explains why the crushing is more important during the reloading.

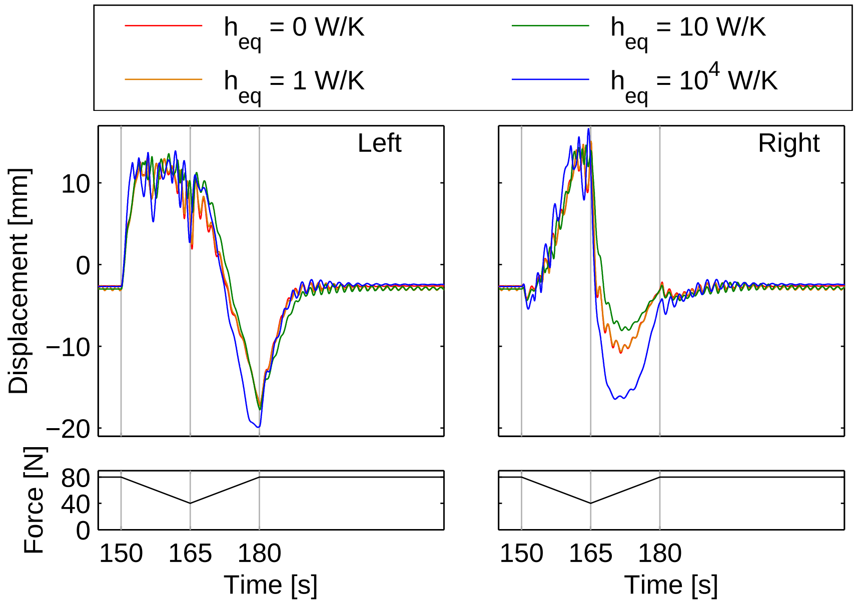

Figure 4.14: Bellows displacement time history for an unloading and loading in an intermediate station.

As for the curve passing analysis, it can be observed that the two intermediate curves present small oscillations between the stations because the temperature in the pneumatic chambers is still varying and consequently the levelling valve lever oscillates around its engaging position.

As previously, Table 4.4 reveals that the heat transfer coefficient clearly impacts the air consumption. Nevertheless, the difference is quite small between $h_{eq} = 1\ W/K$ and $h_{eq} = 10\ W/K$ which corresponds to the order of magnitude measured in Chapter 3. For $h_{eq} = 10\ W/K$, most of the air is admitted during the unloading and loading phases whereas, for $h_{eq} = 1\ W/K$, one quarter is injected during the small remaining oscillations, between the stations when the force is constant.

$h_{eq} = 0\ W/K$	$h_{eq} = 1\ W/K$	$h_{eq} = 10\ W/K$	$h_{eq} = 10^4\ W/K$
$0.29\ kg$	$0.36\ kg$	$0.38\ kg$	$0.41\ kg$

Table 4.4: Total air mass injected in the pneumatic suspension via the levelling valves during the loading/unloading in station test for several heat transfer coefficient h_{eq} values.

4.3.3 Comfort analysis

As it was revealed in Chapter 2, the frequency response of the suspension is influenced by the chosen pipe model. In this section, we thus compare the various pipe models and their influence on the passenger comfort. The comfort test is certainly the best case to check whether the observed differences impact the complete vehicle dynamics since various frequencies are involved. In Ref. [26], it was already shown that the influence of the pipe air mass cannot be neglected for a train running in straight track at 300 km/h.

In the reference pneumatic circuit, the auxiliary tanks are connected to the bellows via a single orifice. The comparison between the various pipe equations does not make sense in this case since the inertia effects will be negligible. Therefore, the orifice is replaced by a longer pipe as it could be encountered in other suspension morphologies. The pipe parameters of Chapter 2 and Chapter 3 are tested.

It clearly appears that the pipe geometry strongly affects the passenger comfort. Furthermore, the various configurations behave differently for the two considered vehicle speeds. Indeed, for the 10 m/s case, the measured RMS accelerations are more important for the short pipe configuration (parameters of Chapter 2). The long pipe (parameters of Chapter 3) and the single orifice cases give results that are quite close from each other. On the contrary, when the vehicle is running at 20 m/s, the RMS acceleration is more important for the long pipe configuration while the short pipe and the single orifice present similar results. It can be explained looking at Fig. 4.15. For the 10 m/s speed, the lower frequencies (around 1 Hz) are excited. For those frequencies, on one hand, the dynamic stiffness remains limited in all the cases, it only begins to increase for the long pipe curves due to the resonance effect. On the other

	10 m/s	20 m/s
Reference vehicle (9 mm orifice)		
Incompressible algebraic (Eq. (2.17))	0.0836 m/s^2	0.1587 m/s^2
Pipe parameter of Chapter 2 ($L_p = 1\ m$ and $d_p = 18\ mm$)		
Incompressible algebraic (Eq. (2.17))	0.1209 m/s^2	0.1690 m/s^2
Incompressible differential (Eq. (2.16))	0.1172 m/s^2	0.1617 m/s^2
Fanno differential (Eq. (2.26))	0.1170 m/s^2	0.1587 m/s^2
Pipe parameter of Chapter 3 ($L_p = 10\ m$ and $d_p = 15.5\ mm$)		
Incompressible algebraic (Eq. (2.17))	0.0825 m/s^2	0.2060 m/s^2
Incompressible differential (Eq. (2.16))	0.0796 m/s^2	0.2146 m/s^2
Fanno differential (Eq. (2.26))	0.0797 m/s^2	0.2161 m/s^2

Table 4.5: Weighted RMS values of the vertical acceleration measured at the carbody centre for different pipe modelling approaches and pipe configurations.

hand, the damping is important for the short pipe and the single orifice while it is lower for the long pipe. For the 20 m/s case, the higher frequencies are more involved, inducing an important stiffness and a small damping for the long pipe whereas, for the short pipe, the stiffness remains limited and the damping increases. Therefore, it could be concluded that, when the vehicle is running at 10 m/s, the larger RMS accelerations observed for the short pipe are due to an insufficient damping while, for the 20 m/s case, the long pipe configuration suffers from the pipe cut-off effect which induces a higher dynamic stiffness.

It must also be noticed that the difference between algebraic and differential models are not so important whereas the incompressible differential and Fanno differential models give rather equivalent results. Considering the carbody flexibility, as in Ref. [26], could perhaps lead to an other conclusion if the carbody own modes interact with the suspension.

4.3.4 $\Delta Q/Q$

The $\Delta Q/Q$ test will contribute to analyse in more details the impact of the various valves. The reference pneumatic circuit is considered and all transformations are assumed adiabatic.

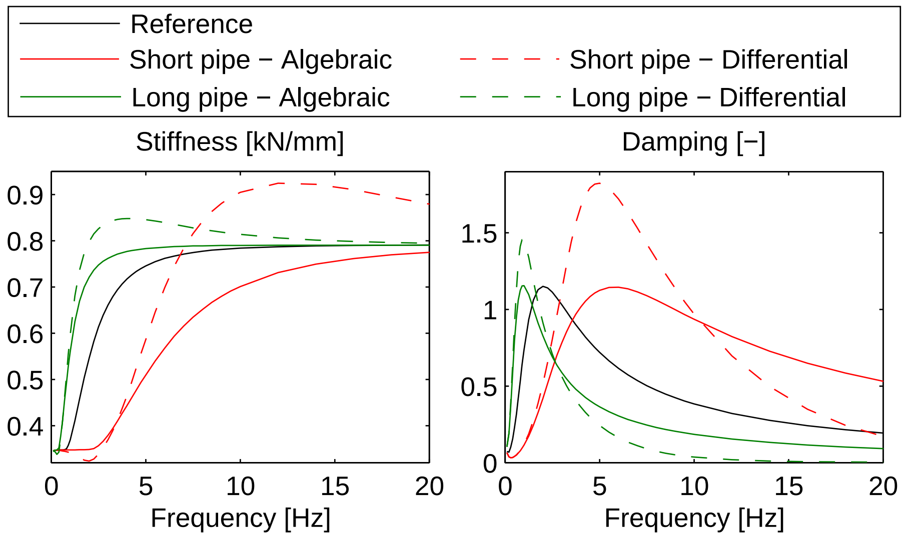

Figure 4.15: Comparison of dynamic stiffness K_{dyn} and damping coefficient D_z for various pipe modelling approaches and pipe configurations.

In Figs. 4.16 and 4.17, the situation with all valves connected and the case without any valve are compared. The overloaded diagonal (front right - rear left) and the unloaded diagonal (front left - rear right) can clearly be distinguished. When there are no valve, the bellows behave as classical helical springs: they are crushed or extended when the ramp excitation is applied and an equilibrium is rapidly reached. When the valves are active, several zones can be identified:

1. During and just after the excitation is applied (i.e. from 5 s to 23 s), the levelling valves react so as to increase the pressure in the overloaded bellows and to decrease the pressure in the unloaded ones. This induces a torsion torque on the carbody and excites the primary suspensions. Furthermore, some large oscillations begin when the lever displacements on the unloaded diagonal reach the engaging value of the safety valve. This is due to the abrupt characteristic of the safety valve. Due to the valve action, the mean displacements of the extended bellows slowly decrease between 10 s and 23 s (Fig. 4.16). Moreover the pressure difference on

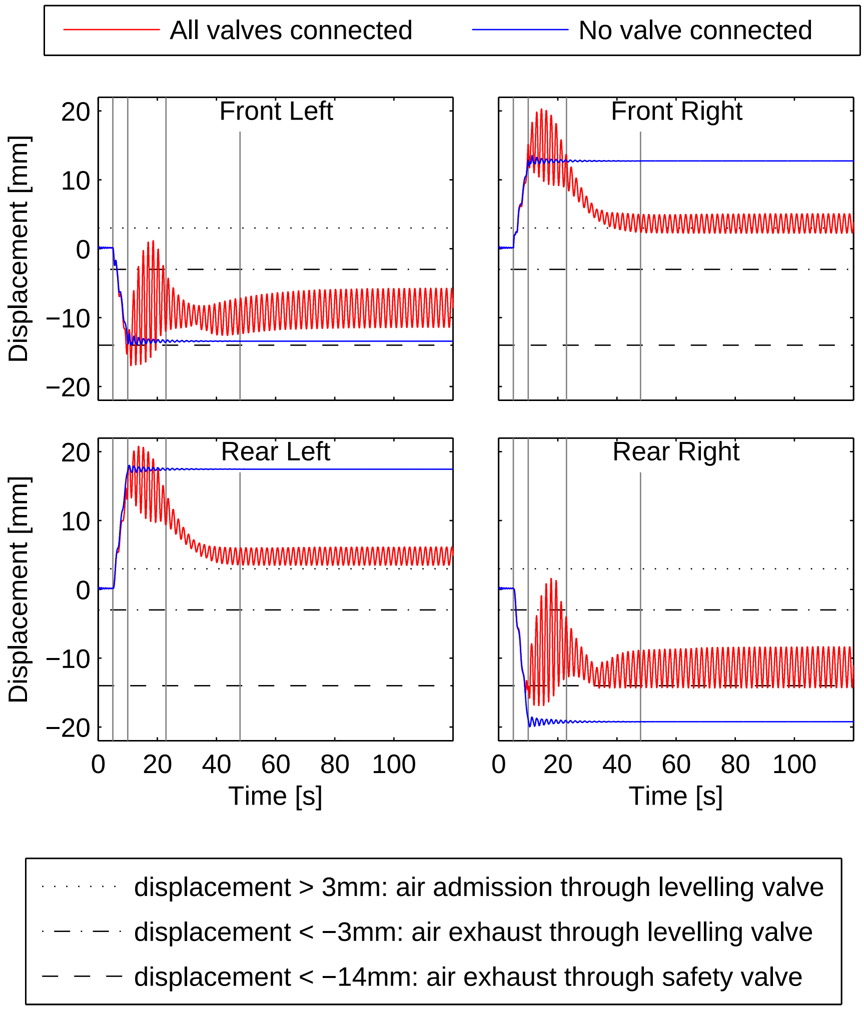

Figure 4.16: Valve lever displacement for the $\Delta Q/Q$ test with all valves connected or without any valves. A positive displacement corresponds to air admission in the system and thus to a bellows crushing (negative bellows displacement).

each bogie grows continuously.

2. Between 23 s and 48 s, the pressure difference between the two bellows of a same bogie becomes sufficient to activate the differential valve. Air exhausts from the crushed bellows to the extended ones. This tends to increase (in absolute value) the valve lever displacement of the unloaded bellows.

3. When the rear right valve lever displacement reaches the engaging value of the safety valve, a sudden exhaust flow passes through this valve and thus decreases (in absolute value) the lever displacement. The repetition of this process causes undesirable oscillations. It must be noticed that such a phenomenon has been practically observed on real metros.

It clearly appears in Fig. 4.17 that the valve action induces large pressure fluctuations which result in important wheel/rail vertical force variations. The set point of the differential valve is therefore very important to not overpass the limit value. A small engaging value is better in rail twist to limit the wheel unloading but it must be sufficient to prevent the differential valve to be engaged when passing a curve. The $\Delta Q/Q$ curve will be analysed in Section 4.4 when comparing the four-point configuration with other morphologies.

As the safety valves seem to be responsible for the oscillating motion, their removal would allow to reach an equilibrium. Fig. 4.19(a) shows that the system tends toward a stable situation but it is still disturbed by small oscillations due to the abrupt portion of the levelling valve characteristic. The mean value of those oscillations is greater (in absolute value) than the engaging value of the safety valve. This is why larger perturbations appear when the safety valves are connected.

To avoid the observed oscillations even when safety valve are connected, the differential pressure valve could be modified to make it to exhaust directly to the atmosphere (see Fig. 4.19). Even though initial oscillations due to the safety valves cannot be avoided, this solution reaches an equilibrium illustrated in Fig. 4.18. In the final state, the lever displacements are such that the levelling and the safety valves on the unloaded diagonal are not engaged. There is thus no flow entering or exiting those air spring. However, for the overloaded bellows,

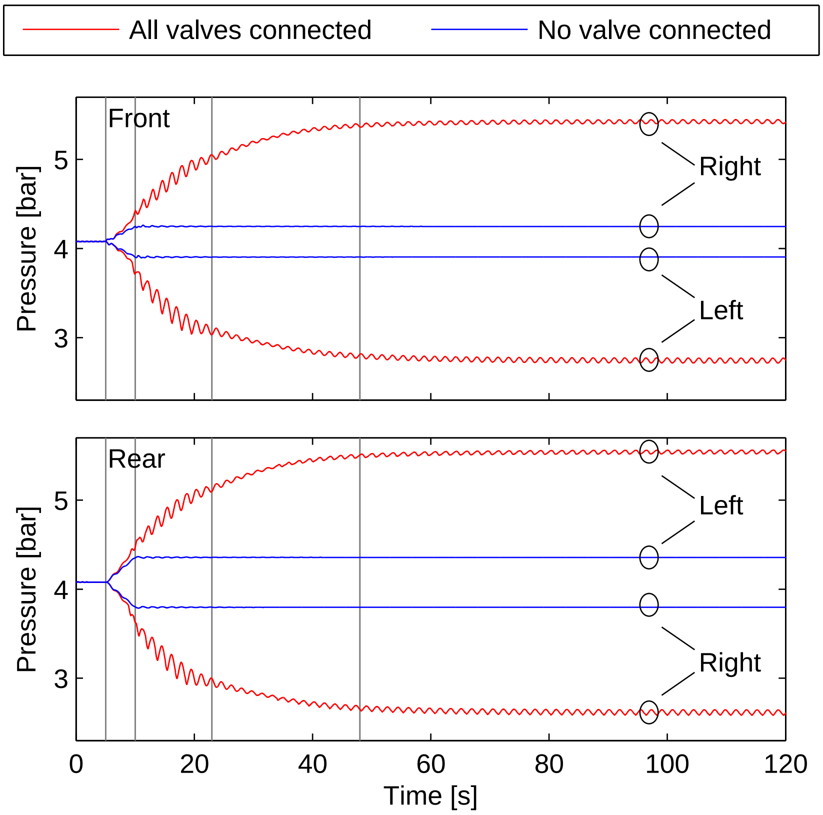

Figure 4.17: Tank pressure for the $\Delta Q/Q$ test with all valves connected or without any valves.

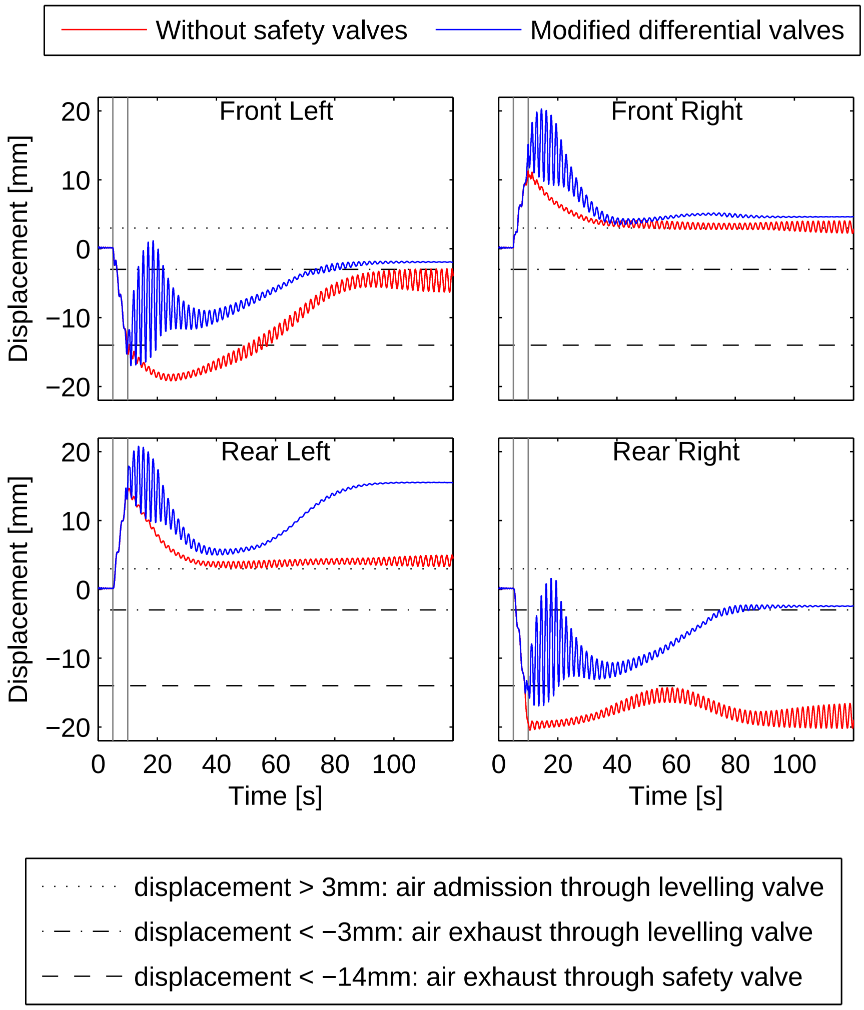

Figure 4.18: Valve lever displacement for the $\Delta Q/Q$ test when safety valves are not connected or when the pressure differential valve exhaust directly to the atmosphere. A positive displacement corresponds to air admission in the system and thus to a bellows crushing (negative bellows displacement).

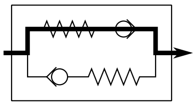

(a) Original pressure differential valve.

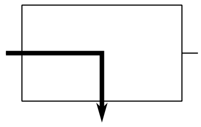

(b) Pressure differential valve exhausting to atmosphere.

Figure 4.19: Illustration of the pressure differential valve modification.

the levelling valve admits air that is directly exhausted to the atmosphere via the modified pressure differential valve, resulting in an important compressed air consumption.

4.3.5 Failure mode analysis

A very useful advantage of the developed approach based on component modelling is that critical situations can be analysed. For instance, it is possible to check how the vehicle reacts when a failure mode occurs such as a punctured cushion, a leakage in a pipe connection, a levelling valve locked in admission position, etc. As recommended by the UIC 518 standard (Ref. [4]), the various failure modes that may arise on a train, not only for the pneumatic suspension, have to be identified. The probability they occur and their potential impact on the vehicle safety determine whether the failures have to be tested and investigated.
Using a simulation tool allows us to study a wide range of situations that may be difficult, costly or dangerous to test in practice. A lot of configurations can be investigated in order to identify what are the consequences of the failure. Furthermore, data that are difficult to measure in practice can be obtained more easily via the numerical analysis.

The question of pneumatic suspension failure modes is addressed in more details in Misonne's Master thesis (Ref. [47]) who has investigated extensively this concern using the tools developed in the present thesis. In this section, we propose to analyse a particular case of failure called the *simple leakage*. It encompasses several real problem such as a more or less important hole in the cushion, a levelling valve or safety valve not completely closed, a leakage in a

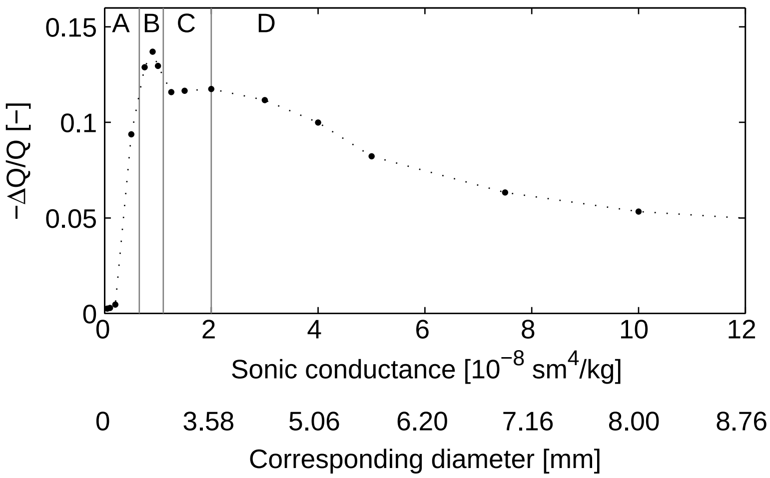

Figure 4.20: Wheel load variation for a leakage occurring on the front right cushion. The leakage sonic conductance and the equivalent diameter according to Eq. (2.37) are indicated on the abscissa.

pipe connection, etc. The goal of this analysis is to show how such a problem can be dealt with using the developed tools.

The leakage is modelled as an orifice placed between the front right cushion and the atmosphere. The mass flow rate through the orifice is computed using the ISO 6358 standard (see Ref. [3] and Eq. (2.36)).
The leakage effects are analysed with the metro at rest. A constant sonic conductance C is imposed and the wheel unloading is measured once the vehicle has stabilized.
Fig. 4.20 shows the front right wheel unloading for various values of the leakage sonic conductance. Since only the steady solution is analysed, the transient behaviour is not shown and could be more critical if the leakage occurs in a curved track. Nevertheless, four main parts can be distinguished on this graph.

- **Part A.** (Fig. 4.21(a)) Due to the leakage, the air spring is crushed and the levelling valve is therefore engaged to compensate for the air loss. An equilibrium establishes between the mass flow rate entering via the levelling valve and the one exiting via the leakage. Nevertheless, the wheel unloading and the bellows crushing rise as the sonic conductance increases. This part of the curve strongly depends on the levelling valve characteristic.

- **Part B.** (Fig. 4.21(b)) The bellows crushing is such that the levelling valve lever reaches the abrupt part of its characteristics. Roll oscillations ensue and cause more important wheel load variations. Furthermore, the air spring reaches intermittently the bumpstop.
- **Part C.** (Fig. 4.21(c)) The front right air spring is resting on the bumpstop and oscillations have vanished. In this zone, the pressure difference between right and left bellows increases rapidly because the levelling valve can not increase the entering mass flow rate anymore since the lever displacement is blocked by the bumpstop.
- **Part D.** (Fig. 4.21(d)) The pressure difference between the left and right bellows is greater than the engaging value of the differential valve. Consequently, the fluid goes from left to right and the front left cushion begins to deflate. The corresponding levelling valve compensates by injecting air in the air spring. When the leakage size increases, the left bellows crushing rises and the pressure decreases, which reduces the load difference between the left and right wheels, and thus reduces the front right wheel unloading.

This analysis shows how various equilibria establish for various running conditions. It must be noticed that the presented curve strongly depends on the valve characteristics. Taking the emergency spring into account instead of a rigid bumpstop can also modify the suspension response. This analyse therefore highlights that the valves design is important to achieve good properties in critical situations.

4.4 Comparison of various configurations

In this section, we use the developed models to compare the three well-established pneumatic suspension configurations described in Section 1.3.2. To do so, the four-point pneumatic circuit of the reference vehicle is modified so as to consider the three-point and the two-point morphologies.

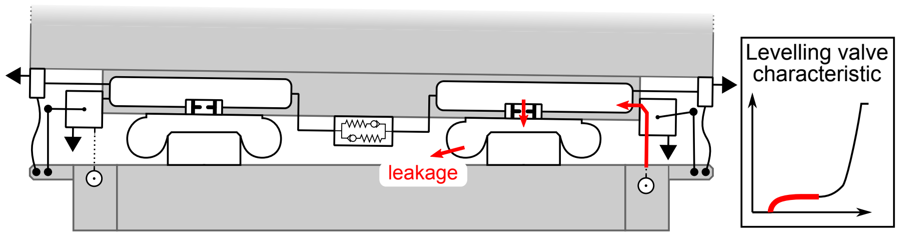

(a) Part A.

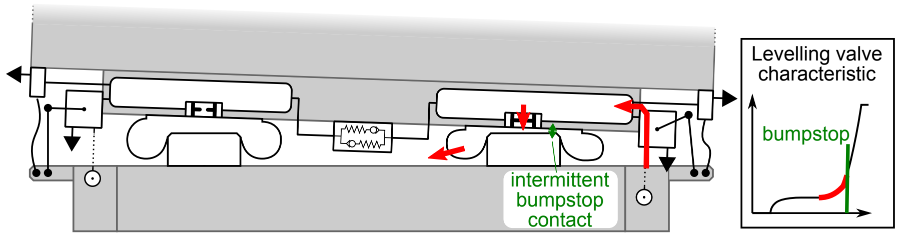

(b) Part B.

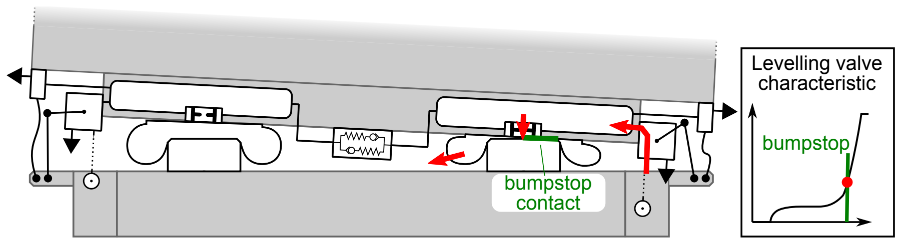

(c) Part C.

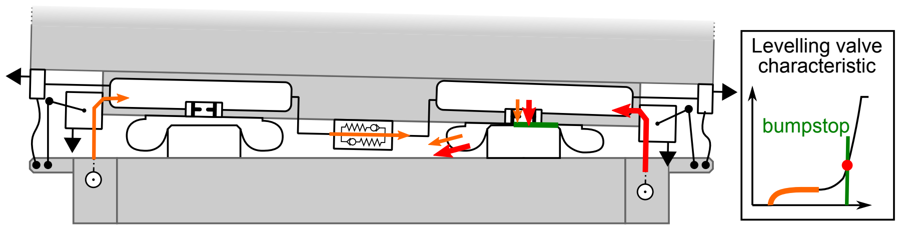

(d) Part D.

Figure 4.21: Illustration of the various zones of the wheel load variation curve during the leakage test. Levelling valve working positions are illustrated on the right (red: right levelling valve, orange: left levelling valve).

4.4.1 Morphology description

Four-point suspension

The four-point suspension circuit corresponds to the reference case presented in Section 4.1.3 (see Fig. 4.5).

Two-point suspension

The two-point configuration is illustrated in Fig. 4.22(a). The direct connection between the bellows and the auxiliary tank via an orifice remains unchanged. Only one levelling valve per bogie is kept and placed in the centre of the traverse. With the present model, the valve must be connected to a pneumatic chamber. Therefore, an additional tank is added between the two auxiliary tanks. The characteristic of the valve was adapted so that the mass flow is doubled for equivalent position and pressure in order to guarantee that the inflating time will not be modified with respect to the four-point configuration. Finally, the safety valve and the differential valve are removed.
As it was mentioned in Section 1.3.2, the two-point suspension requires the presence of an anti-roll bar. The anti-roll bar model described in Section 4.1.2 is thus added to the vehicle multibody model. The torsion bar stiffness is determined so as to obtain an equivalent carbody roll angle for the curve passing test of Section 4.2.2 using Eq. (4.1). The equivalent roll stiffness of the four air spring is equal to 360 Nm. Only the volumetric stiffness is considered since the area stiffness due to the effective area gradient is not null for the two-point configuration. The following parameters are thus used for the anti-roll bar:

Torsion bar length	l	1 m
Lever length	a	0.3 m
Torsion bar stiffness	K_β	33 kNm

Of course, other criteria such as the lateral comfort or the gauging should be taken into account and practical design considerations could lead to another dimensioning but it is out of scope of the present work. Let also note that anti-roll bars can also be used with a four-point suspension.

Three-point suspension

The three-point morphology is an hybrid configuration between the two-point and the four-point suspensions. As illustrated in Fig. 4.22(b), it is implemented

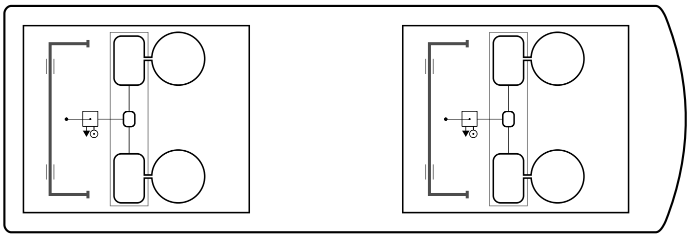

(a) Two-point suspension.

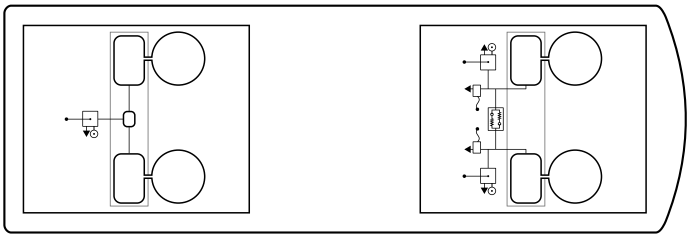

(b) Three-point suspension.

Figure 4.22: Pneumatic circuit of the two-point configuration (top) and the three-point configuration (bottom).

by combining the two-point circuit for one bogie and the four-point one for the other. This suspension is thus asymmetrical: the bogie equipped with two levelling valves has an important roll stiffness whereas the other has almost no roll stiffness since the air can flow freely from left to right and vice versa.
The connection between right and left side may be on the rear bogie (as illustrated in Fig. 4.22(b)) or on the front bogie. The two possibilities will be considered. In practice, one configuration corresponds in fact to the other running in the opposite direction on the track.

4.4.2 Analysis of the suspension response without valves

Curve passing test. Fig. 4.23 shows the roll angle time history when the coach passes the curve defined in Section 4.2.2 without any valve connected. The four-point and the two-point configurations present very similar time histories. Considering a heat transfer would lead to more differences since the four-point suspension roll stiffness decreases when the temperature varies. For the two-point suspension the pressure does not change significantly and only the anti-roll bar, whose stiffness is constant, compensates for the centripetal acceleration.
As expected, the roll angle for the three-point morphology is larger since only the bogie equipped with two levelling valves compensates for the lateral acceleration. In the present case, the bump stops are not taken into account. Otherwise, the roll angle would have been more limited. The position of the left-right connection, on the leading or on the trailing bogie, does not affect the vehicle response.

$\Delta Q/Q$ test. The wheel load variations during the $\Delta Q/Q$ test are plotted in Fig. 4.24. Only the first and the fourth wheelsets are shown. The force acting on the second and the third wheelsets are similar to the other one of the same bogie. Once again the two-point and the four-point suspension curves are very close to each other. This test also reveals the advantage of the three-point configuration that limits the vertical wheel/rail contact force in rail twist. When the left-right connection is placed on the rear bogie, the roll stiffness of the front bogie is more important. Consequently, the carbody roll angle, which is more guided by the front bogie, is more influenced by the twist excitation

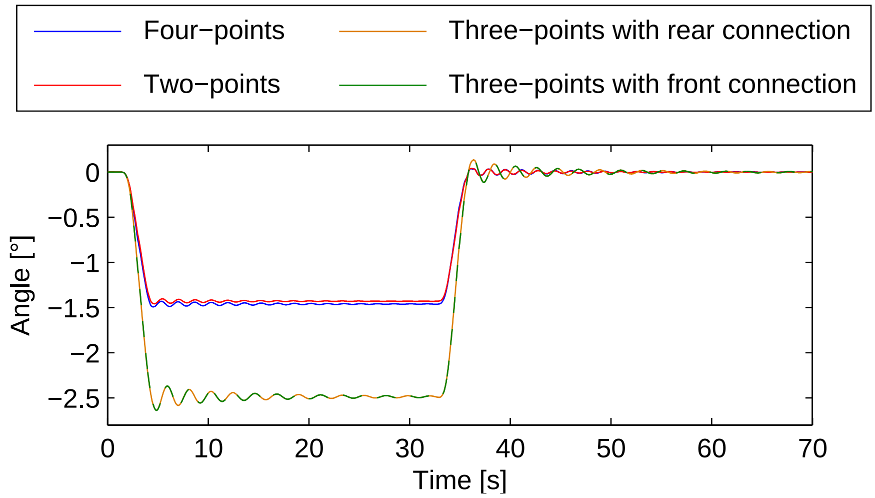

Figure 4.23: Carbody roll angle for the curve passing test.

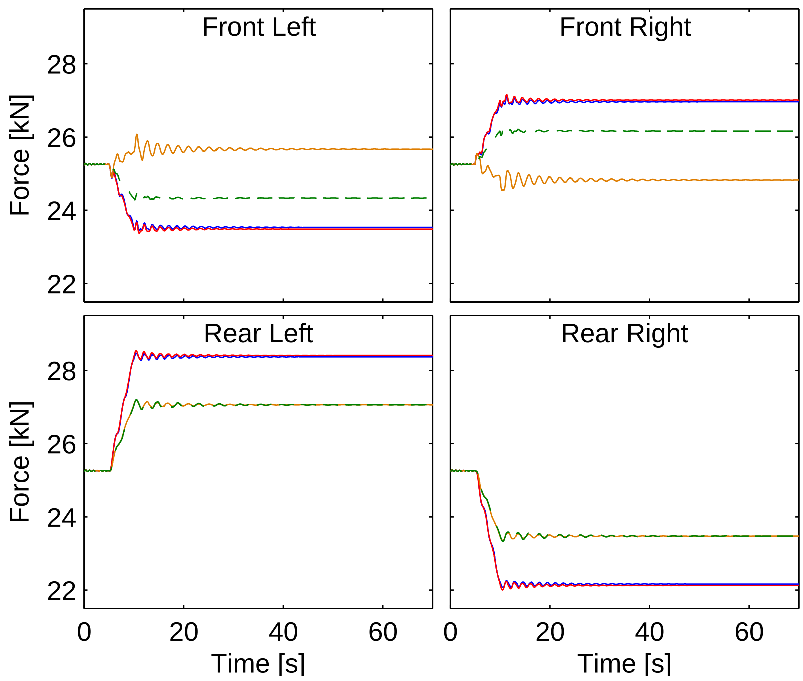

Figure 4.24: Vertical component of wheel/rail contact forces for the $\Delta Q/Q$ test.

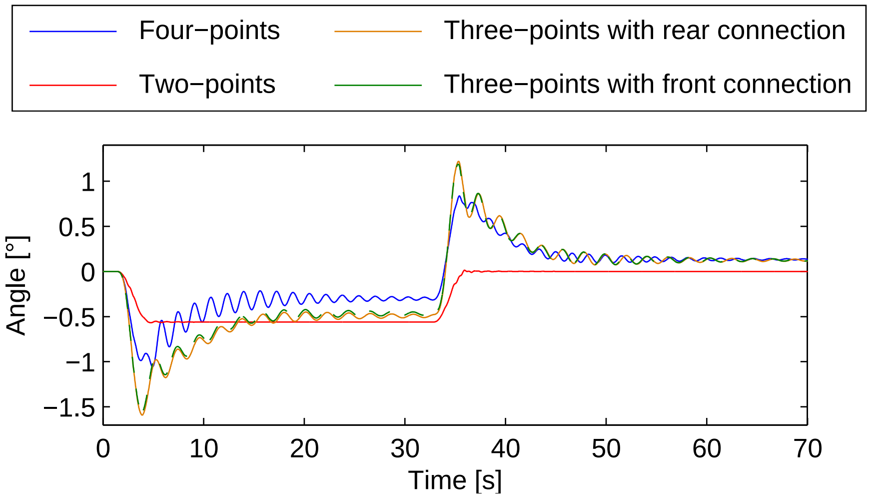

Figure 4.25: Carbody roll angle for the curve passing test.

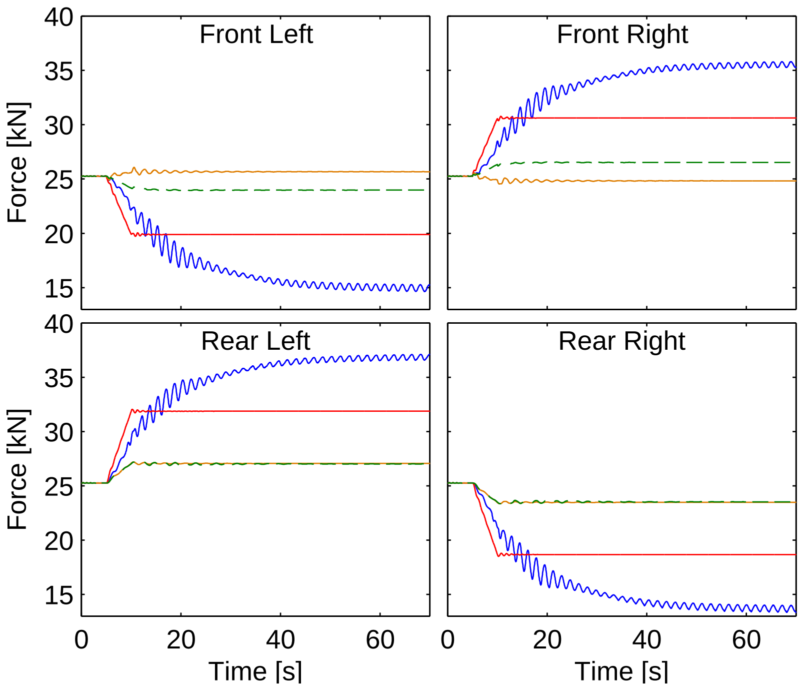

Figure 4.26: Vertical component of wheel/rail contact forces for the $\Delta Q/Q$ test.

and it is therefore more important than for the front connection case. This explains why the two three-point topologies have different forces acting on the first wheelset.

4.4.3 Analysis of the suspension response with valves

Curve passing test. When the valves are connected, the levelling valves tend to reduce the roll angle in curve for the four-point suspension as it was noticed in Section 4.3.1. The anti-roll bar of the two-point suspension must be four times stiffer ($K_\beta = 132\ kNm$) so as to obtain an equivalent roll angle. This stiffness has been chosen to obtain an intermediate value between the maximal and the stabilized four-point roll angle, as it can be check in Fig. 4.25.
In this graph, the roll angle of the three-point suspension is always more important than the four-point one even after the levelling valve reaction. It is due to the primary suspension crushing which is more important on the bogie equipped with two levelling valves. The pressure difference will also be more important on this bogie. This can cause some problems when considering a full carbody because the pressure differential valve can be engaged or the tank maximal pressure can exceed the maximal acceptable value.

$\Delta Q/Q$ test. The $\Delta Q/Q$ test results are plotted in Fig. 4.26. The behaviour of the three-point suspension is not really affected by the valves.
For the two-point topology, the levelling valves do not operate because the displacement in the bogie centre does not go over the valve engaging limit. However, load variations are more important than for the situation without valves because the anti-roll bar is stiffer.
For the four-point morphology, the valve action described in Section 4.3.4 induces important variations of the contact force. It is the reason why the engaging pressure value of the differential valve must be limited.
The present analysis would lead to conclude that, for equivalent roll angle in curve, the two-point configuration is preferable since it induces lower wheel/rail force variation. Nevertheless, it is important to note that the mass of a metro carbody can double when it is full. Therefore, the anti-roll bar stiffness should be self-adapting to the mass, which is quite difficult to implement. The advantage of the four-point suspension, regarding this concern, is that it can

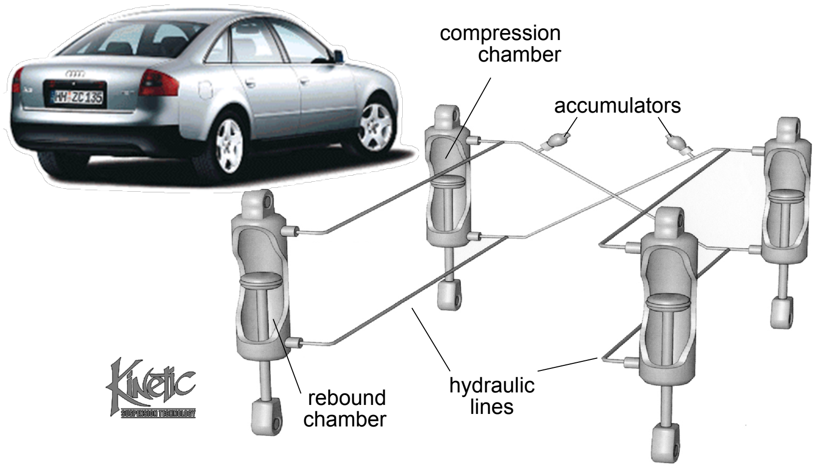

Figure 4.27: Illustration of the Kinetic H2 system from Tenneco-Kinetic (illustration from Tenneco Automotive).

compensate, via the levelling valves, for the lateral acceleration whatever the payload.

4.5 Novel configurations

The previous section has shown that the pneumatic suspension design implies a trade-off between a large roll stiffness in curve and a low stiffness when passing through rail twist. A solution would consist in using an active suspension system and take information about the track into account. However, for railway applications, even though many research programs are conducted to introduce active suspensions (see Refs. [35, 16]), the industrial tendency is still to favour purely passive and mechanical solutions, at least for the vertical secondary suspension. It can partly be explained by the important forces acting on the system and the hard working conditions at the bogie level. Such a problem also appears for ground vehicles, especially for sport cars. In this domain, active suspension are perhaps more spread.
Nevertheless, some pure mechanical devices are still investigated and developed such as the *Kinetic H2* system proposed by the shock absorber manufacturer Tenneco (see Ref. [14]). As illustrated in Fig. 4.27, this system replaces the

shock absorbers by double acting hydraulic cylinders and avoid the use of a classical anti-roll bar. The rebound chambers on one side are connected via hydraulic line to the compression chambers on the other side, resulting in two hydraulic circuit with a “H” shape which explains the “H2” name.
This system as already been studied by the CEREM[1] leading to the development of hydraulic models coupled to a complete multibody model of the car (see Ref. [22]). The goal of this section is to investigate how a railway vehicle equipped with such a system would behave. First, we detail the working principle of the *Kinetic H2* system and explain how it could be adapted to the reference metro. A full pneumatic version of this device is also proposed so as to avoid the use of oil. The two solutions are finally compared with the classical two-point and four-point suspensions.

4.5.1 The *Kinetic H2* system

Working principle

The operation principle of the *Kinetic H2* system is illustrated in Fig. 4.28. When the vehicle is submitted to a cornering roll excitation (Fig. 4.28(a)), the inner cylinders are unloaded and the outer ones are overloaded. Consequently, the oil tends to leave the outer compression chambers and the inner rebound chambers. Since all those chambers are connected, the fluid escapes toward the accumulator in which the pressure increases. On the other circuit, the inverse phenomenon occurs and the pressure goes down. The combination of the two results in a high roll resistance.
When the two axles are rolling in opposite sense (Fig. 4.28(b)), or *articulating*, there are two crushed and two extended chambers on each circuit. The fluid can therefore flow freely between the cylinders without modifying the air volume in the accumulator and thus does not induce important pressure modifications.
Furthermore, when the car is submitted to bounce motion, the left compression chambers fluid flows toward the right rebound chamber and vice versa. Only the rod volume flows toward the accumulator. Therefore, the vertical stiffness is not significantly modified. Moreover, various valves located at the cylinder and accumulator connections are used to tune the suspension damping.

[1] Centre for Research in Mechatronics of the Université catholique de Louvain.

Hydraulic modelling

The hydraulic modelling is quite similar to the thermodynamical approach developed in Chapter 2 for the pneumatic components. We will briefly review the main ideas, further details being available in Ref. [22]. A copy of this paper is provided in appendix A.

For the cylinder, each chamber is considered as a control volume in which the pressure is given by a differential equation depending on the entering flow and the volume variation. Those differential equations are quite stiffer due to the low compressibility of oil. Given the pressures, the cylinder reaction forces can be calculated on the basis of the effective area of each chamber.

The accumulator is composed of a volume of gas that is assumed to be compressed and expanded under adiabatic conditions. The gas volume varies because of the entering or exiting oil flow. In this case, the oil compressibility is negligible compared to that of the gas.

Valves and hydraulic lines are both resistive components. Their governing equations are equivalent to the incompressible differential pipe model discussed in Section 2.5.1. For the valves, a classical pressure drop coefficient or a pressure-flow characteristic is used. Special care is taken when connecting several pipes: the flow are calculated by imposing a constraint such that no oil accumulates at the connection node. This approach is more reliable than the use of small virtual volumes that would lead to time-integration problems due to the very low fluid compressibility.

Concerning the time-integration, the co-simulation exchange time interval must be reduced to 0.1 ms due to the stiffness of the hydraulic cylinder equations. The inner time step sizes of the two integration processes remain equal to this interaction time step size.

Integration in the railway secondary suspension

The *Kinetic H2* system only provides roll resistance but no vertical stiffness. So as to adapt this device to railway secondary suspensions, we therefore propose to combine it with a two-point suspension in which the classical anti-roll bar is removed. The resulting hydro-pneumatic circuit is depicted in Fig. 4.29. Among the pneumatic components, the circuit contains four double acting hydraulic cylinders, two accumulators and twelve hydraulic lines with valves. The hydraulic cylinders are mounted between the same anchor points as the pneu-

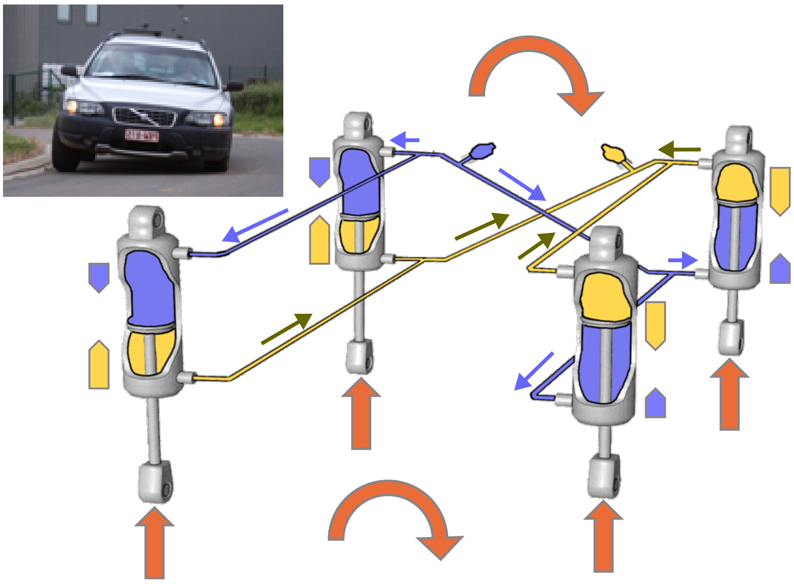

(a) Cornering roll resistance.

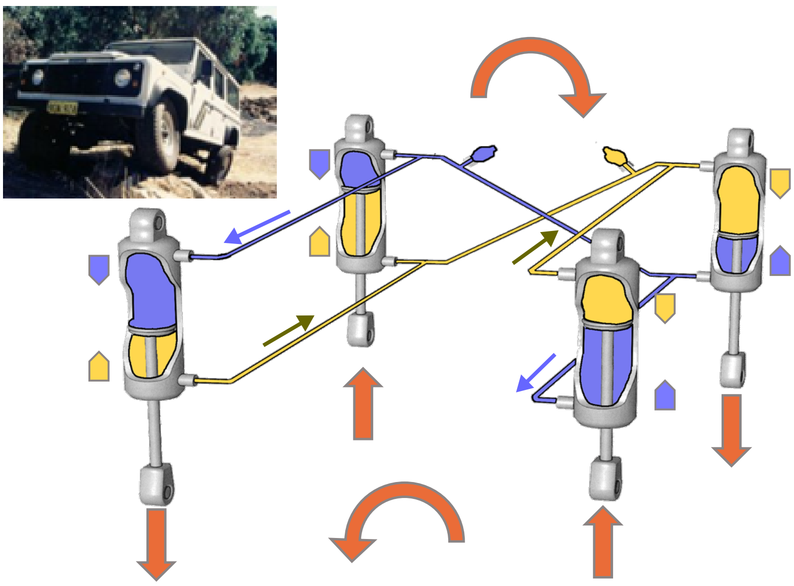

(b) Diagonal articulation.

Figure 4.28: Illustration of the *H2* system working principle.

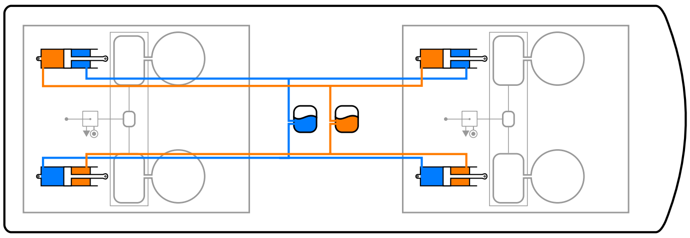

Figure 4.29: Hydro-pneumatic circuit of the *H2* system adapted to railway secondary suspension.

matic bellows. This would not be feasible in practice but facilitates the implementation since the already defined multibody input and output can be reused.

Model parameters are determined so as to obtain a stiffness equivalent to the mechanical anti-roll bar. Neglecting the oil compressibility, the quasi-static roll stiffness of the *Kinetic H2* system can be approximated by:

$$K_{roll} = \frac{8b^2 p_0 (A_{comp} + A_{reb})^2 \gamma}{V_0} \tag{4.3}$$

where: K_{roll} is the roll stiffness $[Nm]$;
b is the distance from the cylinder to the central longitudinal axis $[m]$;
p_0 is the initial pressure $[Pa]$;
A_{comp} is the compression chamber area $[m^2]$;
A_{reb} is the rebound chamber area $[m^2]$;
V_0 is the initial air volume in each accumulator $[m^3]$;
γ is the specific heat ratio.

The parameters used in the present study are listed in Table 4.6.

4.5.2 Pneumatic adaptation of the *Kinetic H2* system

Adding hydraulics could seem complex and too costly from an industrial point of view. For that reason, we propose a full pneumatic version of the *Kinetic H2* system and we will verify whether the desired properties can be achieved. The quasi-static roll stiffness can be approached by the following relation:

$$K_{roll} = \frac{8b^2 p_0 (A_{comp} + A_{reb})^2 \gamma}{V_{accu} + 2V_{comp,0} + 2V_{reb,0}} \tag{4.4}$$

Cylinder inner diameter		90 mm
Cylinder rod diameter		30 mm
Cylinder compression chamber area	A_{comp}	6.4 10^-3 m^2
Cylinder rebound chamber area	A_{reb}	5.7 10^-3 m^2
Hydraulic line diameter		12 mm
Length of hydraulic lines connected to cylinders		6 m
Length of hydraulic lines connected to accumulators		0.85 m
For the low stiffness case (four-points without valves)		
Initial pressure	p_0	10 bar
Accumulator air volume	V_0	1.7 dm^3
For the high stiffness case (four-points with valves)		
Initial pressure	p_0	20 bar
Accumulator air volume	V_0	0.85 dm^3

Table 4.6: Parameters of the adapted *Kinetic H2* system for railway secondary suspension.

with: K_{roll} the roll stiffness $[Nm]$;
b the distance from the cylinder to the central longitudinal axis $[m]$;
p_0 the initial pressure $[Pa]$;
A_{comp} the compression chamber area $[m^2]$;
A_{reb} the rebound chamber area $[m^2]$;
V_0 the volume of each accumulator $[m^3]$;
$V_{comp,0}$ the initial volume of the compression chamber $[m^3]$;
$V_{reb,0}$ the initial volume of the rebound chamber $[m^3]$;
γ the specific heat ratio.

Contrary to the hydraulic version, the stiffness is now influenced by the internal volume of the pneumatic cylinders. Furthermore, the compressibility of fluid in the pipe is not negligible and the accumulator volume V_0 have thus to include the internal volume of the pneumatic lines.

The *pneumatic H2* circuit is illustrated in Fig. 4.30. Two accumulators are used for each circuit instead of one for the hydraulic solution. A first reason is

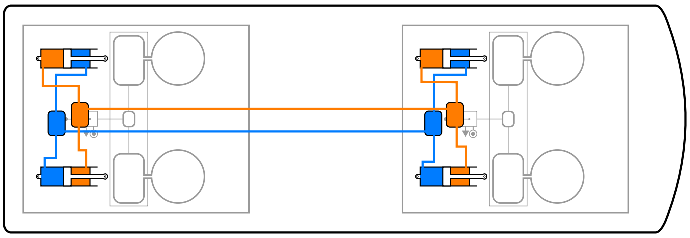

Figure 4.30: Circuit of the pneumatic version of the *Kinetic H2* system adapted to railway secondary suspension.

that the tank can be placed on the bogie without modifying the symmetry of the circuit. Moreover, it ensues a direct connection between the right and left cylinders of a same bogie. This reduces the resistance to bounce motion since the fluid must flow from right rebound chamber to left compression chamber and vice versa. In order to avoid a too large duct volume, a smaller pipe diameter can be used for the front-rear connecting pipe because the flow runs through only during twist excitations which are quite slow.

From a modelling point of view, all the components of the *pneumatic H2* circuit correspond to one case treated in Chapter 2 except the double acting cylinder. This one is treated as a "double cushion": each chamber possesses the same parameters as a bellows (see Sections 2.1 and 2.4). For cylinders, the effective area is constant and the rebound chamber volume gradient is negative.
The *pneumatic H2* circuit parameters are listed in Table 4.7. Those values were determined by first imposing that the *H2* circuit pressure is equal to the working pressure of the pneumatic bellows. The accumulator volume cannot be reduced endlessly since it must take into account the duct volume. The only solution is therefore to increase the cylinder size. The obtained diameter is quite large. However, it remains smaller than the cushion diameter.

4.5.3 Analysis of the suspension response without valve

Curve passing test. In this section the hydraulic and pneumatic versions of the *Kinetic H2* system adapted to railway vehicles are compared to the classical two-point and four-point morphologies. When levelling valves are removed, it can be observed in Fig. 4.31 that the *H2* system behaves similarly

Pneumatic line diameter		26 mm
Length of pneumatic line connected to cylinders		2 m
Length of pneumatic line connected to accumulators		10 m
Initial pressure	p_0	4 bar
For the low stiffness case (four-points without valves)		
Cylinder inner diameter		180 mm
Cylinder rod diameter		30 mm
Cylinder compression chamber area	A_{comp}	25.4 10^-3 m^2
Cylinder rebound chamber area	A_{reb}	24.7 10^-3 m^2
Cylinder compression chamber volume	$V_{comp,0}$	1.0 dm^3
Cylinder rebound chamber volume	V_{reb}	9.9 dm^3
Accumulator air volume	V_0	7 dm^3
For the high stiffness case (four-points with valves)		
Cylinder inner diameter		250 mm
Cylinder rod diameter		30 mm
Cylinder compression chamber area	A_{comp}	49.1 10^-3 m^2
Cylinder rebound chamber area	A_{reb}	48.4 10^-3 m^2
Cylinder compression chamber volume	$V_{comp,0}$	2.0 dm^3
Cylinder rebound chamber volume	V_{reb}	1.9 dm^3
Accumulator air volume	V_0	3.5 dm^3

Table 4.7: Parameters of the *pneumatic H2* circuit for railway secondary suspension.

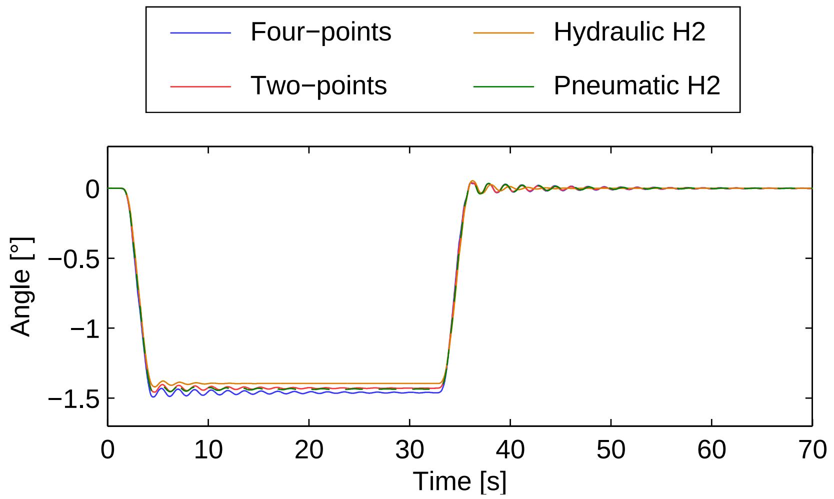

Figure 4.31: Carbody roll angle for the curve passing test.

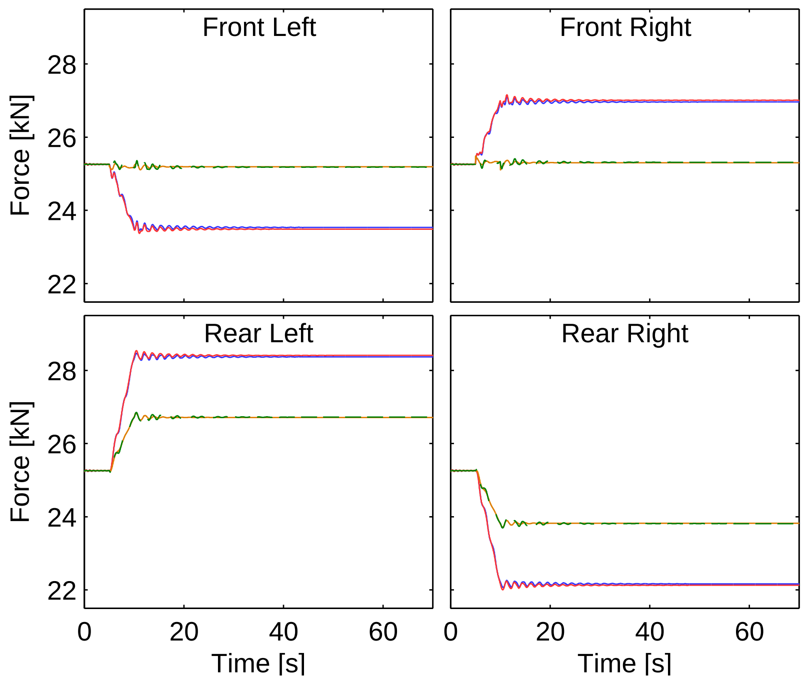

Figure 4.32: Vertical component of wheel/rail contact forces for the $\Delta Q/Q$ test.

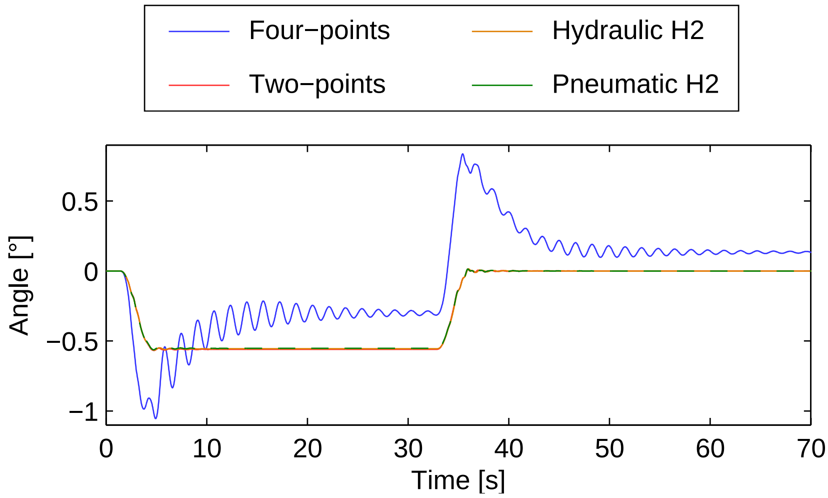

Figure 4.33: Carbody roll angle for the curve passing test.

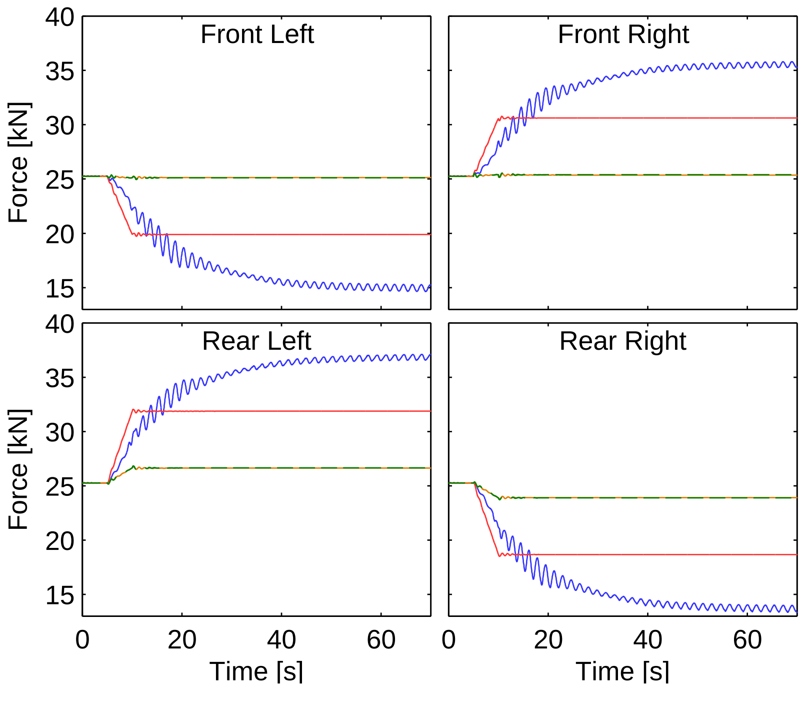

Figure 4.34: Vertical component of wheel/rail contact forces for the $\Delta Q/Q$ test.

	10 m/s	20 m/s
Four-point suspension	0.0836 m/s^2	0.1587 m/s^2
Two-point suspension	0.0831 m/s^2	0.1585 m/s^2
Hydraulic *H2*	0.1294 m/s^2	0.3135 m/s^2
Pneumatic *H2*	0.0758 m/s^2	0.1460 m/s^2

Table 4.8: Weighted RMS value of the vertical acceleration measured at the carbody centre for various suspension morphologies.

to the classical configurations. The oscillations are more rapidly damped with the *H2* configurations, especially with the hydraulic version.

$\Delta Q/Q$ test. Concerning the wheel/rail contact forces, Fig. 4.32 shows that there is no important modification of the vertical component for the first wheelset. For the rear wheelset, the wheel force fluctuations are reduced by a factor two with respect to classical topologies. The remaining variations are mainly due to the area stiffness of the bellows and compensate for the carbody roll angle due to the front wheelsets tilt.

4.5.4 Analysis of the suspension response with valves

Curve passing test. When valves are connected, the *H2* configurations react in the same way as the two-point suspension (Fig. 4.33). The levelling valve does not work since the displacement in the bogie center remain close to zero. The increased stiffness reduces the carbody roll angle accordingly.

$\Delta Q/Q$ test. During the $\Delta Q/Q$ test, the wheel load variations are the same as without valves even though the system is stiffer (Fig. 4.34). This clearly highlights the potential interest of the *H2* principle. Moreover, since the roll stiffness depends on the fluid pressure, it could be envisaged to have an adjustable stiffness depending on the passenger number. This would require a regulation system that ensures that, in the case of the pneumatic solution, the mean pressure in the *H2* circuit is, for instance, equal to the pressure in the bellows.

Comfort test. As it was explain in Section 4.5.1, in case of vertical motions, the fluid in the *H2* system must flow from the right compression chambers to the left rebound chambers and vice versa. It must therefore be checked that the *H2* does not reduce the vertical passenger comfort.
Table 4.8 presents the RMS acceleration measured for the comfort test defined in Section 4.2.4.
It appears that, as it could be expected, the four-point suspension and the two point-suspension give equivalent results. The anti-roll bar does not affect the vehicle comfort properties.
For the pneumatic *H2* system, the RMS acceleration does not increase. On the contrary, it is a bit lower. That can certainly be explained by the increased damping due to additional pneumatic circuit. Even for the 20 m/s speed, the pneumatic version would not decrease the comfort.
However, for the hydraulic *H2* configuration, the measured acceleration is larger which corresponds to a decreased comfort. This is due to the hydraulic lines that are longer since they are all connected at the carbody centre, causing a too important damping. Adopting the direct left-right connection at the bogie level as for the pneumatic version and increasing the pipe diameter could certainly improve the comfort properties of the hydraulic *H2*.

More generally, both the hydraulic and pneumatic versions of the *Kinetic H2* system could be optimized in order to improve their performances for the various tests. However, this process should be performed taking industrial constraints and criteria into account so as to guarantee the feasibility of the system. For instance, for the comfort performances, other aspects must be considered such as the potential contact with the bumpstops which must be avoided, even in some critical situations.

The analyses presented in this chapter has shown that the developed tools are suitable to address this question. The different considered tests highlight the flexibility of our approach. Further development could be investigated such as the use of strongly coupled models that would be more efficient to resort, for instance, to optimization algorithms.

Conclusion

The main objective of the present thesis was to develop pneumatic models and to couple these with multibody dynamics so as to study the behaviour of railway pneumatic suspensions.

In the first part of our work, we described the various elements composing the pneumatic circuit associated with the air springs presently used for railway secondary suspensions. Indeed, next to the pneumatic cushions which are the main suspension components, other parts are commonly used such as auxiliary tanks to adapt the suspension stiffness, connecting pipes on which restriction orifices can be added to increase the damping, levelling valves to keep a constant height between the bogie and the carbody, etc. We pointed out the number of possible circuit morphologies which mainly depend on the levelling valve configuration.
We also introduced multibody dynamics which is today a very powerful tool to deal with railway vehicles. Even though some pneumatic suspension models are available in MBS software, they are not adapted to treat the complete suspension circuit. Therefore, MBS must be coupled with more involved models, in a multidisciplinary approach. With this respect, some coupling approaches were described, among which the co-simulation technique that was used in the present work.

An important part of our work consisted in analysing existing air spring models and proposing approaches able to take a complete pneumatic circuit into account. To achieve this task, we resorted to thermodynamics that allows us to consider each suspension separately and then to connect them easily with each other. We particularly focused on the pipe models for which several techniques were investigated. The various approaches were compared and confronted to existing models for a test-case composed of a cushion connected to an auxiliary tank via a pipe. This study pointed out the effect of the pipe air mass which induces a resonance peak in the dynamic stiffness curve. If this phenomenon was already revealed by existing models in multibody codes, it must be noticed that the thermodynamical approach allows us to consider valves and circuit configurations that are more complex than the simple bellows-tank subsystem. Furthermore, only the differential pipe models can take this resonance effect into account. But when the pipe length becomes smaller, the air mass influence becomes negligible and algebraic models are suitable and even more efficient in terms of calculation speed. We also compared the incompressible flow approaches to a compressible Fanno line model. The results were confronted to a reference solution calculated in FLUENT. We observed that compressible effects limit the flow in the pipe but their impact is only visible for high frequencies. Moreover, the obtained results were in good agreement with the FLUENT solution. We then implemented a discretization method so as to take into account the influence of pressure waves in the pipe but it did not bring better results for the analysed test-case which considered short pipes only. We also analysed the heat transfer between the suspension components and the atmosphere and we showed that it can also affect the suspension response. This justified the necessity to perform experimental tests on a real air spring.

The next chapter of the thesis was therefore dedicated to the analysis of experiments that we have carried out on a metro suspension. The test bench was composed of an air spring connected to an auxiliary tank via a pipe and submitted to displacement excitations applied by an hydraulic actuator. Several pipe configurations were tested for quasi-static and dynamic actuations. A first experiment which consists in applying very slow expansions and compressions was used to estimate the parameters of the bellows model. Then, we relied on a step test to evaluate the heat transfer coefficients. The order of magnitude of obtained values is such that the suspension response is quite sensitive to the heat transfer. The last experiments also revealed that it would be interesting to test large displacement amplitudes to check the heat transfer properties of bellows and tanks. Finally, we performed a dynamic test that consisted in applying to the bellows a sinusoidal displacement excitation. Various frequencies were tested in the range $0-10\ Hz$ for most of the cases. Those final experiments were used to determine the pipe model parameters and showed a good agreement between experimental and simulation results. Furthermore, for smallest excitation amplitudes, the frequency range was extended to $0 - 20\ Hz$. In the case of the longest pipe, a second resonance was revealed and it was shown that it is captured by the discretized one-dimensional flow model only.

Finally, we took advantage of the flexibility of our approach to deal with complete and various pneumatic circuits and to study the performances of a complete metro car. A multibody model of the vehicle was built in the MBS package Simpack. The co-simulation interface provided by this software was used to couple the mechanical system to the pneumatic models implemented in Matlab/Simulink. Several tests were analysed and various pneumatic parameters were compared.
For the passenger comfort assessment, we observed that the RMS acceleration is a bit less favourable when the compressible pipe model is used instead of the incompressible model. The influence of the heat transfer was analysed via a curve passing and a loading/unloading test. We observed a great influence of this parameter on the carbody roll angle in curve. However it was shown that the levelling valve action smooths those discrepancies, but the impact of the heat flow on the air consumption calculation remains significant.
The $\Delta Q/Q$ experiment which consists in applying a twist excitation to the coach revealed an unnatural behaviour of the four-point configuration: the levelling system inflates the crushed air springs and deflates the extended ones, inducing large wheel load variations, whereas the opposite action would be preferable. We also showed that the proposed model can suitably be used to investigate the effects of suspension component failures. This can be very beneficial in the design process, especially since the standards explicitly require their analysis in the assessment process.
We then compared various suspension topologies that are commonly employed. For instance, we showed that for an equivalent roll stiffness in curve, the two-point configuration induces less wheel load variation during the $\Delta Q/Q$ test. However this system is not able to adapt the stiffness to variable payloads, contrary to the four-point configuration.
Lastly, we investigated novel configurations inspired from recent automotive advances. The most interesting is certainly the pneumatic version of the *Ki-*

netic H2 system which consists in adding four interconnected pneumatic cylinders which avoid important wheel load variations in curve for equivalent roll stiffness.

Perspectives

In the future, a lot of interesting features can be explored in the field of multiphysics modelling of railway suspension.

First of all, concerning the *pneumatic modelling*, it could for instance be checked whether the pressure waves in pipes can influence the circuit dynamics. If it is not the case for railway suspension, it could affect other kind of applications with higher dynamics such as robotics. It would then be challenging to analyse how this technique can efficiently be coupled to a MBS formulation. The influence of pneumatic lines located between valves and pneumatic chambers should also be analysed in more details.

Concerning the *coupling techniques*, we limited our work to the use of the co-simulation, which was satisfactory in our case, with some special attention to pay to the presence of hydraulic circuits. However, the pneumatic model implementation is not restricted to the co-simulation. On the contrary, it would be easy to use other methods such as a strong coupling with a set of symbolic equations for the multibody system. The efficiency in terms of simulation time and portability would certainly be strongly improved.

If we observed a good match between *experimental test* and simulation results, a larger number of suspensions should be tested. It could, for example, confirm whether the loss coefficient of each duct element can be added as it is done for incompressible steady flows. If it is the case, characterizing most commonly used elements on the basis of further tests or existing tables would allow to build an accurate suspension model without resorting to further experimental tests. The method we have proposed to determine the cushions properties should also be confronted to the techniques used by suspension manufacturers.

Lastly, we believe that the developed tool should be exploited at the first design stages in a so-called *mechatronic approach*. This would allow us for example to detect earlier problems due to a component failure or to reveal unexpected behaviour in some specific working conditions. Moreover, thanks to the thermodynamical approach, additional criteria could quantitatively be taken into account in the selection process of pneumatic components such as the compressed air consumption. Furthermore, we showed that our methods are suitable to investigate novel suspension configurations which exhibit promising properties. Such a system should certainly be investigated in more details and improved so as to satisfy practical industrial constraints. For instance, for the *Kinetic H2* system, a stiffness which can adapt to the variable payload could be implemented and the possible failure mode effects could be checked to confirm the feasibility before any part is produced. This further research should be conducted closely with the industry so as to ensure that the proposed solutions answer to real needs.

Appendix A

Hydro-MBS Modelling

This appendix is a copy of the paper entitled *Multiphysics Modeling of Multibody System: Application to Car Semi-Active Suspensions* which has been accepted for publication in the *Vehicle System Dynamics* journal. This article is

now availabe online at http://prod.informaworld.com/smpp/content db=all content=a926476010 frm=titlelink?words=docquier,fisette .

Bibliography

[1] En 14363 - railway applications - testing for the acceptance of running characteristics of railway vehicles - testing of running behaviour and stationary tests.

[2] Iso 2631 - mechanical vibration and shock – evaluation of human exposure to whole-body vibration.

[3] Iso 6358: Pneumatic fluid power – components using compressible fluids – determination of flow-rate characteristics.

[4] Uic518 - essais et homologation de véhicules ferroviaires du point de vue du comportement dynamique - sécurité - fatigue de la voie - qualité de marche.

[5] S. Alfi, S. Bruni, and L. Mazzola. Impact of suspension component modelling on the accuracy of rail vehicle dynamics simulation. In *Procedings of the 11th Mini conference on Vehicle System Dynamics, Identification and Anomalies, Budapest, Hungary*, 2008.

[6] A. Alonso, J. G. Gimenez, F. J. Nieto, and J. Vinolas. Increasing air suspension effectiveness by means of a variable area orifice. In *Procedings of the 21th IAVSD Symposium on Dynamics of Vehicles on Roads and Tracks, Stockholm, Sweden*, 2009.

[7] J. D. Anderson Jr. *Modern Compressible Flow With Historical Perspective.* McGraw-Hill, New York, 1990.

[8] M. Arnold. Numerical methods for simulation in applied dynamics. In *Simulation Techniques for Applied Dynamics*, pages 191–246. 2009.

[9] M. Arnold and A. Heckmann. From multibody dynamics to multidisciplinary applications. In *Multibody Dynamics*, pages 273–294. 2007.

[10] J. Baumgarte. Stabilization of constraints and integrals of motion. *Computer Methods in Applied Mechanics and Engineering*, 1:1–16, 1972.

[11] P. Beater. *Pneumatic Drives: System Design, Modelling and Control.* Springer, 1 edition, Mar. 2007.

[12] M. Berg. An airspring model for dynamic analysis of rail vehicles, trita-fkt report 1999:32. Technical report, Division of Railway Technology, Department of Vehicle Engineering, Royal Institute of Technology (KTH), Stockholm, 1999.

[13] M. Berg. A three-dimensional airspring model with friction and orifice damping. *Procedings of the 16th IAVSD Symposium on Dynamics of Vehicles on Roads and Tracks, Pretoria, South Africa, 1999. Journal of Vehicle System Dynamics*, 33(Supplement):528–539, 2000.

[14] P. Boon, K. Reybrouck, S. Schel, B. Vandermissen, and S. van Raemdonck. Integration of the "kinetic" anti-roll system with semi-active damping. *ATZ worldwide eMagazine*, 9:32–37, 2009.

[15] O. Brüls, A. Cardona, and M. Géradin. Modelling, simulation and control of flexible multibody systems. In *Simulation Techniques for Applied Dynamics*, volume 507, pages 21–74. Springer, 2009.

[16] S. Bruni, R. Goodall, T. X. Mei, and H. Tsunashima. Control and monitoring for railway vehicle dynamics. *Vehicle System Dynamics*, 45(7):743–779, 2007.

[17] P. Chatelle, J. Duponcheel, and J. Samin. Investigations on non-conventional railway systems through a generalized multibody approach. In *Procedings of the 8 th IAVSD-IUTAM Symposium on the Dynamics of Vehicles on Road and Tracks, Cambridge*, pages 43–57. IAVSD-IUTAM, August 1983.

[18] J.-F. Collard. *Geometrical and kinematic optimization of closed-loop multibody systems.* PhD thesis, Université catholique de Louvain, 2007.

[19] J.-F. Collard, P. Duysinx, and P. Fisette. Kinematical optimization of Closed-Loop multibody systems. In *Multibody Dynamics*, pages 159–179. 2008.

[20] K. Craig and F. Stolfi. *The mechatronics handbook*, chapter Introduction to Computers and Logic Systems. CRC Press, 2002.

[21] B. Delahaut and N. Docquier. Modélisation de véhicules ferroviares munis de suspensions pneumatiques. Master's thesis, Université catholique de Louvain, 2005.

[22] N. Docquier, A. Poncelet, M. Delannoy, and P. Fisette. Multiphysics modeling of multibody systems: Application to car semi-active suspensions. *Vehicle System Dynamics*, 2010. Accepted for publication.

[23] J. Dormand and P. Prince. A family of embedded Runge-Kutta formulae. *Journal of Computational and Applied Mathematics*, 6(1):19–26, Mar. 1980.

[24] B. M. Eickhoff, J. R. Evans, and A. J. Minnis. A review of modelling methods for railway vehicle suspension components. *Vehicle System Dynamics: International Journal of Vehicle Mechanics and Mobility*, 24(6):469–496, 1995.

[25] J. Evans and M. Berg. Challenges in simulation of rail vehicle dynamics. *Vehicle System Dynamics*, 47(8):1023–1048, 2009.

[26] A. Facchinetti, L. Mazzola, S. Alfi, and S. Bruni. Mathematical modelling of railway vehicles with secondary airspring suspension: safety and ride comfort. In *Procedings of the 21th IAVSD Symposium on Dynamics of Vehicles on Roads and Tracks, Stockholm, Sweden*, 2009.

[27] P. Fisette. *Génération symbolique des équations du mouvement de systèmes multicorps et application dans le domaine ferroviaire*. PhD thesis, Université catholique de Louvain, 1994.

[28] P. Fisette, K. Lipinski, and J. Samin. Dynamic behaviour comparison between bogies : Rigid or articulated frame, wheelset or independent wheels. *Vehicle System Dynamics: International Journal of Vehicle Mechanics and Mobility*, 25(1 supp 1):152, 1996.

[29] P. Fisette and J.-C. Samin. A new wheel/rail contact model for independent wheels. *Archive of Applied Mechanics*, 64(3):180–191, Mar. 1994.

[30] C. Fuhrer and B. Leimkuhler. A new class of generalized inverses for the solution of discretized euler-lagrange equations. In *NATO Advanced Research Workshop on Real-Time Integration Methods for Mechanical System Simulation, Snowbird, Utah*, 1989.

[31] L. Ganovski. *Modeling, simulation and control of redundantly actuated parallel manipulators*. PhD thesis, Université catholique de Louvain, 2007.

[32] J. García de Jalón. Twenty-five years of natural coordinates. *Multibody System Dynamics*, 18(1):15–33, 2007.

[33] J. García de Jalón and E. Bayo. *Kinematic and Dynamic Simulation of Multibody Systems: The Real-Time Challenge*. Springer-Verlag, 1 edition, Dec. 1994.

[34] M. Géradin and A. Cardona. *Flexible Multibody Dynamics: A Finite Element Approach*. John Wiley & Sons, 2001.

[35] R. Goodall. Active railway suspensions: Implementation status and technological trends. *Vehicle System Dynamics: International Journal of Vehicle Mechanics and Mobility*, 28(2):87, 1997.

[36] M. Gretzschel and O. Vaculín. Simulation of an integrated mechatronic train. *Vehicle System Dynamics*, 37:137, June 2002.

[37] W. Hooker and G. Margulies. The dynamical attitude equations for an n-body satellite. *Journal of Astronautical Sciences*, 12:123–128, 1965.

[38] I.E.Idel'cik. *Mémento des pertes de charge-Coefficients de pertes de charge singulières et de pertes de charge par frottement*. Editions Eyrolles, Paris, 13 edition, 1986.

[39] S. Iwnicki. *Handbook of Railway Vehicle Dynamics*. CRC Taylor & Francis, 1 edition, May 2006.

[40] J. J. Kalker. *Three-Dimensional Elastic Bodies in Rolling Contact*. Dordrecht/Boston/London: Kluwer Academic Publishers, 1990.

[41] D. Karnopp and R. C. R. Donald L. Margolis. *System Dynamics: Modeling and Simulation of Mechatronic Systems (Third Edition)*. John Wiley & Sons Inc, 2000.

[42] W. Kortüm and O. Vaculín. Is multibody simulation software suitable for mechatronic systems? *Vehicle System Dynamics*, pages 1–15, Dec. 2004.

[43] C. B. Laney. *Computational Gasdynamics*. Cambridge University Press, June 1998.

[44] J. D. Mattingly. *Elements of Gas Turbine Propulsion*. McGraw-Hill, New York, 1996.

[45] L. Mazzola. *Possibilities and challenges for the virtual homologation of the railway rolling stock*. PhD thesis, Politecnico di Milano, 2009.

[46] M. O. A. E. Menceur, P. Pudlo, P. Gorce, and F.-X. Lepoutre. An automatic procedure for identifying alternative automobile ingress movements in young and elderly populations with or without prostheses. *International Journal of Industrial Ergonomics*, 39(6):966–980, Nov. 2009.

[47] G. Misonne. Etude et analyse des modes de défaillance des suspensions secondaires pneumatiques sur les véhicules ferroviaires. Master's thesis, Université catholique de Louvain, 2010.

[48] A. Nieto, A. Morales, A. Gonzélez, J. Chicharro, and P. Pintado. An analytical model of pneumatic suspensions based on an experimental characterization. *Journal of Sound and Vibration*, 313(1-2):290–307, 2008.

[49] P. E. Nikravesh and H. A. Affifi. Construction of the equations of motion for multibody dynamics using point and joint coordinates. In *Computer-aided analysis of rigid and flexible mechanical systems*, volume Series E: Applied Sciences268, pages 31–60. Kluwer Academic Publications, NATO ASI, 1994.

[50] H. Paynter. *Analysis and Design of Engineering Systems*. MIT Press, Cambridge, 1961.

[51] A. Poncelet, J.-F. Collard, and P. Fisette. Parameter sensitivity analysis: Symbolic computation for large multibody systems. In *Proceedings of*

the First Joint International Conference on Multibody System Dynamics, Lappeenranta, Finland, 2010.

[52] T. Postiau, L. Sass, P. Fisette, and J.-C. Samin. High-performance multibody models of road vehicles: Fully symbolic implementation and parallel computation. *Vehicle System Dynamics*, 35:57–83, Jan. 2001.

[53] M. Presthus. Derivation of air spring model parameters for train simulation. Master's thesis, Lulea University of Technology, 2002.

[54] O. QING and S. YIN. THE NON-LINEAR MECHANICAL PROPERTIES OF AN AIRSPRING. *Mechanical Systems and Signal Processing*, 17(3):705–711, May 2003.

[55] G. Quaglia and M. Sorli. Air suspension dimensionless analysis and design procedure. *Vehicle System Dynamics*, 35(6):443, 2001.

[56] M. Raison. *On the quantification of joint and muscle efforts in the human body during motion*. PhD thesis, Université catholique de Louvain, 2009.

[57] M. Raison, C. Aubin, C. Detrembleur, P. Fisette, P. Mahaudens, and J. Samin. Quantification of global intervertebral torques during gait: comparison between two subjects with different scoliosis severities. *Studies in Health Technology and Informatics*, 158:107–111, 2010. PMID: 20543409.

[58] B. Raucent. *Identification des paramÃ¨tres dynamiques des robots manipulateurs*. PhD thesis, Université catholique de Louvain, 1990.

[59] R. E. Roberson and J. Wittenburg. A dynamical formalism for an arbitrary number of interconnected rigid bodies with reference to the problem of satellite attitude control. In *Procedingd of the 3rd International Congress of Automatic Control, London*, 1967.

[60] J. Samin and P. Fisette. *Symbolic modeling of multibody systems*. Springer, 2003.

[61] J.-C. Samin, O. Brüls, J.-F. Collard, L. Sass, and P. Fisette. Multiphysics modeling and optimization of mechatronic multibody systems. *Multibody System Dynamics*, 18(3):345–373, Oct. 2007.

[62] L. Sass. *Symbolic Modeling of Electromechanical Multibody Systems*. PhD thesis, Université catholique de Louvain, 2004.

[63] L. Sass, J. McPhee, C. Schmitke, P. Fisette, and D. Grenier. A comparison of different methods for modelling electromechanical multibody systems. *Multibody System Dynamics*, 12(3):209–250, Oct. 2004.

[64] J.-M. Seynhaeve, G. D. Pelsemaeker, and L. Bolle. Logiciel de calcul d'écoulements transitoires consécutifs à la rupture d'une canalisation. methodes et modeles utilises. Technical report, Université catholique de Louvain, 1992.

[65] SIMPACK. *SIMPACK Reference Manual, Release 8.9. Simpack AG, Gilching, Germany 2009*. Simpack Gmbh, 2010.

[66] Y. Sugahara, A. Kazato, R. Koganei, M. Sampei, and S. Nakaura. Suppression of vertical bending and rigid-body-mode vibration in railway vehicle car body by primary and secondary suspension control: results of simulations and running tests using shinkansen vehicle. *Proceedings of the Institution of Mechanical Engineers, Part F: Journal of Rail and Rapid Transit*, 223(6):517–531, 2009.

[67] P. Sundvall. Comparisons between predicted and measured ride comfort in trains-a case study on modelling. Master's thesis, TRITA-FKT Report 2001:19, Div. of Railway Technology, Dep. of Vehicle Engineering, Royal Institute Of Technology, Stockholm, 2001.

[68] K. Toyofuku, C. Yamada, T. Kagawa, and T. Fujita. Study on dynamic characteristic analysis of air spring with auxiliary chamber. *JSAE Rev (Soc Automot Eng Jpn)*, 20(3):349–355, 1999.

[69] R. A. Wehage and E. J. Haug. Generalized coordinate partitioning for dimension reduction in analysis of constrained dynamic systems. *Journal of Mechanical Design*, 104(1):247–255, Jan. 1982.

[70] C. Weidemann. Air-springs in simpack. *Simpack News*, December:10–11, 2003.

[71] C. Weidemann, L. Mauer, and M. Arnold. Result accuracy and calculation speed in time domain simulation of railway vehicles. In *Proceedings of Multibody Dynamics 2007 conference, Milano, Italy*, 2007.

[72] D. E. Winterbone and R. J. Pearson. *Theory of Engine Manifold Design: Wave Action Methods for IC Engines.* WileyBlackwell, illustrated edition edition, Sept. 2000.